Finite-Strain analysis in Orthogneiss of the Gran Paradiso massif, Western Alps, Italy

Dissertation
zur Erlangung des Grades
„Doktor der Naturwissenschaften“
am Fachbereich für Geowissenschaften
der Johannes Gutenberg-Universität in Mainz

Osama Mohamed Kaoud Kassem
geboren in Souhag in Ägypten

Mainz 2005

Tag der mündlichen Prüfung: 29. 04. 2005

All views and results presented in this thesis are those of the author, unless stated otherwise.

Ich versichere, dass ich die vorliegende Arbeit selbständig und nur unter Verwendung der angegebenen Quellen und Hilfsmittel verfasst habe.

Mainz, den 10. Januar 2005

The Pyramids of Giza, Egypt.

The pyramids of Menkaure's three queens in front of the pyramids of Menkaure, Khafre and Khufu. Pyramids of Giza are the only one of the Seven Wonders of the Ancient World to survive. This is why it has been said: everything fears time, but time fears the Pyramids.

Table of contents

Figure caption:

Fig.1.1: a) Tectonic sketch map of the western and central Alps. b) The location and accessibility of Gran Paradiso massif.

Fig.2.1: Plate-tectonic evolution of the Alpine region from Permian to Tertiary. Africa/Europe relative plate motions are from Dewey et al., (1989), based on analysis of Atlantic magnetic anomalies and transform faults. (a) Pre-Triassic configuration: Africa, Europe, Iberia, and Adria all form parts of pangaea, surrounding a gulf of the Thethys ocean. (b) Late Jurassic: opening of the southern and central Atlantic is transferred eastwards to open up the Neothys Basin between Africa and Europe. Adria remains attached to Africa. (c) Mid-Cretaceous: Adria starts to rift away from Africa, and convergence begins on its northern margin. This causes high-P/low-T metamorphism of crustal rocks, now found in the internal zones of the Alps. (d) Late Cretaceous: Adria moves northwards away from Africa and towards Eruope, forming an accretionary wedge on its northern margin. (e) Oligocene: Collision starts between Adria and Europe, to form the present collisional chain of the Alps (after Platt, 1997).

Fig.2.2: Main tectonic and Palaeographic units of the Alps.

Fig.2.3: Simplified geological map of western Alps. Cross-section SE-NW indicating of the geophysical-geological transect of the western Alps in Fig.2.4 from Schmid and Kissling (2000).

Fig.2.4: The schematic geophysical-geological sections through the western Alps. (ECORS-CROP) After Schmid and Kissling (2000).

Fig.2.5: Tectonic map of the Gran Paradiso massif.

Fig.3.1: Graphical representation of strain ellipsoids: the Flinn diagram. A) Different ellipsoids are described using the value K = (a-1) / (b-1). B) If the volume is not constant,

the line a = b (1+ Δ) divides the field of flattening strain. After Flinn 1962, and Ramsay, 1967.

Fig.3.2: (a, b and c) Maps showing localities of finite-strain samples.

Fig.3.3: (a) XZ section of moderately deformed augengneiss SSE of Pont; note that feldspar porphyroclasts with axial ratios of up to ~4 are not parallel to main-phase foliation. (b) Quartzite conglomerate from base of Zermatt-Sass zone E of Lillaz; most clasts are parallel to foliation. (c) Mylonitic deformation of augengneiss leading to platy gneiss; sample GP02-106. (d) Weakly deformed metagranite E of Ceresole; large feldspar clasts are at high angle to foliation. (e) Dynamically recrystallized feldspar porphyroclasts indicating top-W shear sense; both microphotographs are from sample GP02-80A. (f). Recrystallized feldspar porphyroclasts and mica fish indicating top-W shear sense; sample GP02-102.

Fig.3.4: (a) Lineation map for Gran Paradiso massif and contact between Gran Paradiso massif and Zermatt-Saas zone near Lillaz (b); arrow heads indicate plunging direction.

Fig.3.5: Modified AKF diagram showing fundamental phase relations in the system K2O-MgO-Al2O3-SiO2-H2O relevant to Phengite solid solubility. Abbreviations: Ea eastonite, Ms Muscovite (after Massonne and Schreyer 1987).

Fig.3.6: Phengite chemistry: a) compositional variation of Si and Al. b) Relationship between Mg and Si contents. c) Relationship between Mg/Mg+Fe and Si contents. d) Histogram of white mica analyses showing uni-modal distribution of Si contents.

Fig.3.7: Lower-hemisphere equal-area projections for maximum extension direction (X): a) conglomerate samples (contours start at 5% and increment every 5%), b) augengneiss samples (contours start at 1% and increment every 1%), c) Erfaulet samples (contours start at 5% and increment every 5%), and d) all samples (contours start at 1% and increment every 1%). Red squares in the stereographic projections represent mean values of tensor averages.

Fig.3.8: Lower-hemisphere equal-area projections for intermediate direction (Y): a) conglomerate samples (contours start at 5% and increment every 5%), b) augengneiss samples (contours start at 1% and increment every 1%), c) Erfaulet samples (contours start at 5% and increment every 5%), and d) all samples (contours start at 1% and increment every 1%). Red squares in the stereographic projections represent mean values of tensor averages.

Fig.3.9: Lower-hemisphere equal-area projections for maximum shortening direction (Z): a) conglomerate samples (contours start at 5% and increment every 5%), b) augengneiss samples (contours start at 1% and increment every 1%), c) Erfaulet samples (contours start at 5% and increment every 5%), and d) all samples (contours start at 1% and increment every 1%). Red squares in the stereographic projections represent mean values of tensor averages.

Fig. 3.10: (a) Flinn diagram (Flinn 1962) showing relative strain or strain symmetry as obtained by R_f/ϕ (black squares) and Fry (open dots) analysis. (b) R_f/ϕ and Fry data from same samples connected by tie lines; grey sample points indicate data from metasediments. (c) S_X vs K showing positive correlation. (d) S_Y vs K showing pronounced negative correlation. (e) S_Z vs K depicting no obvious correlation.

Fig.3.11: (a) Maps showing Nadai strain magnitude (E_t) for each sample and contours of E_t for Gran Paradiso massif (a), contact of latter with Zermatt-Sass zone (b) and contact with the western part for Gran Paradiso (c). Assuming constant volume deformation Nadai strain magnitude represents square of deviatoric strain ($E_t = E_d^2$). Cross section B-B' in Fig. 12 is indicated.

Fig.3.12: Cross section B-B´ showing contoured Nadai strain magnitude and its relation to nappe contact within Gran Paradiso massif and between latter and Zermatt-Saas zone; highest Nadai strains occur within Gran Paradiso unit.

Fig.3.13: (a) Maps showing K value for each sample and contours of K value for Gran Paradiso massif (a) and contact of latter with Zermatt-Sass zone (b), and contact with the western part for Gran Paradiso (c). Cross section C-C' in Fig. 14 is indicated.

Fig.3.14: Cross section C-C′ showing contoured K value and its relation to nappe contact within Gran Paradiso massif and between latter and Zermatt-Saas zone; K values >1 are in general restricted to Erfaulet unit.

Fig.3.15: Isocon diagrams after Grant (1986) comparing trace element and major oxide concentrations of deformed samples to that of least deformed sample (GP01-23A) (R_{XZ} ratios of samples are shown); element concentration is scaled to 0-100 wt% or parts per million. Solid line represents 1:1 correspondence between concentrations of deformed and almost undeformed samples; dashed line represents averaged estimate of volume loss based on enrichment of Zr (open circles), Al_2O_3 (open triangles) and TiO_2 (open squares).

Fig.4.1: Schematic nappe sequence in northern part of Western Alps and maximum PT conditions for Gran Paradiso and Erfaulet units; emplacement of higher pressure Gran Paradiso unit onto Erfaulet unit demands that 4-11 km of vertical section was removed during nappe emplacement.

Fig.4.2: Schematic illustration of the three exhumation processes: normal faulting, ductile flow and erosion (After Ring et al. 1999).

Fig.4.3: Plots of model results for tensor average strains, illustrating the exhumation and strain history for proportional strain rates, respectively; depth of initial accretion is 46 km; residence time within a steady-state wedge is 6myr.

Fig. 5.1: Cross section E-W showing broad domal structural; Erfaulet unit forms base of exposed section and crops out in major valleys.

Fig. 5.2: Schematic structural model for occurrence of slightly constrictional strain in Erfaulet unit. Early S1 foliation parallel to tectonic contact between Gran Paradiso unit and Erfaulet unit is folded and forms gneiss-cored fold nappe of Vissers & Compagnoni (1984); S2 foliation is generally subparallel to S1, which explains flattening strain, but in hinge zones of F2 folds S2 is at high angle to S1 leading to local constrictional strain.

Acknowledgments

I wish to express my cordial thanks and deep gratitude to all of those individuals who provided their kind help to me during the various stages of this work. From the Institute of Geosciences, University of Mainz, Germany, my thankfulness is due to the following pre-eminent persons; all have contributed to the success of this doctoral thesis in one way or another. My supervisor deserves my special thanks for his knowledgeable supervision and academic guidance as well as for his constant support and encouragement to advance my research work though the good and difficult times. He initiated fruitful discussions and made suggestions all of which have improved the text. In addition, he has enlightened me through courses pertinent to the geology of the Alps. I have benefited considerably from this scientific approach; in particular during my field work to which has contributed and within the framework of three excursions.

From the Institute of Geosciences, University of Mainz, I'm equally grateful to all of my colleagues who have provided their help and support during the initial phases and/or furtherance of this doctoral thesis.

At the same time, and from my home land (Egypt), I would like to thank the Head of the Department of Geosciences in the National Research Centre (NRC) for his support and approval of a scholarship that enabled me to purse my doctoral studies abroad. Staff members of the Egyptian Embassy, Berlin, are thanked for their understanding and assistance in procedures concerning the scholarship. More over, the Head of Geophysical Group (NRC) has provided, kindly, her helpful and has shown keen interest in following up the progress of my research studies in Germany. In addition to the former, I would not forget to extend my thanks to all of my colleagues at the NRC; my sincere thanks to them and many others at home are implicit.

Last, but not least, I'm most grateful to my own family members (my parents, brothers and sisters as well as my wife, Hoda, and our children Riham, Mohamed and Rawan). I'm indebted to all of them, beyond words, for their unparalleled patience, continuous solidarity and moral support as well as for their encouragement and understanding. My wife and children, in particular, are thanked for their forbearance, tolerance, sacrifice and solidarity during my intermittent absence, whether in the field (Italy)

and/or at the Institute (Mainz). The least to be done, in this case, is that I am dedicating this doctoral thesis to them with my deep and everlasting appreciation along the road of life.

Abstract:

A finite-strain study in the Gran Paradiso massif of the Italian Western Alps has been carried out to elucidate whether ductile strain shows a relationship to nappe contacts and to shed light on the nature of the subhorizontal foliation typical of the gneiss nappes in the Alps. The R_f/ϕ and Fry methods used on feldspar porphyroclasts from 143 augengneiss and 11 conglomerate samples of the Gran Paradiso unit (upper tectonic unit of the Gran Paradiso massif), as well as, 9 augengneiss (Erfaulet granite) and 3 quartzite conglomerate samples from the underlying Erfaulet unit (lower unit of the Gran Paradiso massif), and 1 sample from mica schist. Microstructures and thermobarometric data show that feldspar ductility at temperatures >~450°C occurred only during high-pressure metamorphism, when the rocks were underplated beneath the overriding Adriatic plate. Therefore, the finite-strain data can be related to high-pressure metamorphism in the Alpine subduction zone. The augen gneiss was heterogeneously deformed and axial ratios of the strain ellipse in XZ sections range from 2.1 to 69.8. The long axes of the finite-strain ellipsoids trend W/WNW and the short axes are subvertical associated with a subhorizontal foliation. The strain magnitudes do not increase towards the nappe contacts. Geochemical work shows that the accumulation of finite strain was not associated with any significant volume strain. Hence, the data indicate flattening strain type in the Gran Paradiso unit and constrictional strain type in the Erfaulet unit and prove deviations from simple shear.

In addition, electron microprobe work was undertaken to determine if the analysed fabrics formed during high-P metamorphism. The chemistry of phengites in the studied samples suggests that deformation and final structural juxtaposition of the Gran Paradiso unit against the Erfaulet took place during high-pressure metamorphism.

On the other hand, nappe stacking occurred early during subduction probably by brittle imbrication and that ductile strain was superimposed on and modified the nappe structure during high-pressure underplating in the Alpine subduction zone. The accumulation of ductile strain during underplating was not by simple shear and involved a component of vertical shortening, which caused the subhorizontal foliation in the Gran Paradiso massif. It is concluded that this foliation formed during thrusting of the nappes onto each other suggesting that nappe stacking was associated with vertical shortening. The primary evidence for this interpretation is an attenuated metamorphic section with high-pressure metamorphic rocks of the Gran Paradiso unit juxtaposed against the Erfaulet unit.

Therefore, the exhumation during high-pressure metamorphism in the Alpine subduction zone involved a component of vertical shortening, which is responsible for the subhorizontal foliation within the nappes.

Zusammenfassung

Eine Verformungsstudie im Gran Paradiso Massif der italienischen westlichen Alpen ist durchgeführt worden, um aufzuklären, ob duktile Verformung ein Verhältnis zu den Deckenkontakten hat und Rückschlüsse auf die Natur der subhorizontal Schieferung, die für die Gneisdecken in den Alpen typisch ist, erlaubt. Die Rf/ϕ und die Fry Methoden wurden auf 143 Augengneis-, 11 Konglomerat- und 1 Glimmerschiefer-Probe der Gran Paradiso Einheit (obere tektonische Einheit des Gran Paradiso Massif), sowie 9 Augengneis (Erfaulet Granit) und 3 Konglomerat-Proben der darunter liegenden Erfaulet Einheit (unterere Einheit des Gran Paradiso Massif) angewendet. Mikrostrukturen und thermobarometrische Daten zeigen, dass Feldspatduktilität bei Temperaturen von ~450°C nur während der Hochdruckmetamorphose auftrat. Folglich können die Verformungsdaten auf die tektonischen Prozesse während der Hochdruckmetamorphose in der alpinen Subduktionzone bezogen werden. Der Augengneis wurde heterogen verformt und axiale Verhältnisse de Verformungsellipse in XZ-Schnitten reichen von 2.1 bis 69.8. Die langen Achsen der Verformungsellipsoide sind W/WNW orientiert und die kurzen Achsen sind subvertikal. Die Verformungsbeträge erhöhen sich nicht in Richtung zu den Deckenkontakten. Geochemische Daten zeigen, dass die Verformungs-akkumulation nicht mit bedeutenden Volumensverschiebungen verbunden war. Folglich zeigen die Daten an, dass die Verformungsgeometrie oblat in der Gran Paradiso Einheit und prolat in der Erfaulet Einheit war und somit von einfachen Scherung abwich.

Zusätzlich wurde Elektronmikrosondearbeien durchgeführt, um festzustellen, ob sich die analysierten Strukturen während der Hochdruckmetamorphose bildeten. Die Chemie von Phengiten lässt vermuten, dass Deformation und abschließende strukturelle Nebeneinander-stellung der Gran Paradiso Einheit gegen die Erfaulet Einheit während der Hochdruck-metamorphose stattfandt.

Da die Verformungsdaten keinerlei Beziehung zu den Deckenkontakten zeigen, wird angenommen, dass sich die Deckenkontakte früh während der Subduktion vermutlich durch spröde Imbrikierung bildeten. Diese Deckenkontakte wurden dann durch duktile Deformation während des Hochdruckmetamorphose durch Unterplattung in der alpinen Subduktionzone heterogen überprägt. Die Akkumulation der duktilen Verformung während der Unterplattung kann nicht mit einfacher Schereund beschrieben werden und beinhaltete

eine Komponente vertikaler Verkürzung, die die subhorizontale Schieferung im Gran Paradiso Massif verursachte. Es wird gefolgert, dass sich diese Schieferung während der Decken-überschiebungen bildete.

1. Introduction

1.1 General considerations:

This study is a contribution to the understanding of the structure and kinematic evolution of the Gran Paradiso massif within the Western Alps of Italy. It has been achieved through field work and subsequent investigations with emphasis on acquisition and interpretation of finite strain and exhumation data. Corroborative microprobe analytical studies were also carried out. These were performed on phengite micas from widespread augen gneisses that form an integral part of the Gran Paradiso massif.

Though the Gran Paradiso and adjacent areas were subjected to wide ranging geological investigations e.g. (Compagnoni et al. 1974; Compagnoni & Prato 1969; Vearncombe 1983,1985; Benciolini et al., 1984; Dal piaz and Lombardo, 1986; Goffé and Chopin, 1986; Pognante et al., 1987; Ballévre, 1988; Biino and Pognante, 1989; Borghi et al., 1992; Compagnoni et al. 1994), they, still, represent key regions wherein much can be learned with reference to the geotectonic evolution of the Alpine Orogen in general and that of the Western Alps in particular. A number of finite-strain studies from natural shear zones show oblate geometries (Coward 1976; Choukrone & Gapais 1983, O'Hara 1990, Bailey et al. 1994, Ring 1999). These oblate fabrics may result from volume loss in simple shear zones or from true flattening with or without volume loss (Ramsay & Wood 1973; Simpson & DePaor 1993). A quantification of finite strain, the degree of non-coaxiality and volume strain is needed to evaluate the significance of such oblate strain geometries and how they may related to the flat-lying foliation characteristic for the nappes in the internides of the Alps.

Other major problems include the stage of orogeny at which nappes form and what the relationship is between finite strain and nappe contacts. Common wisdom is that the bases of nappes are high-strain zones and that therefore the accumulation of large finite strains and nappe emplacement is intimately related. In the Alps, nappe contacts are, at least in part, major lithologic boundaries and the occurrence of Permo-Mesozoic sediments between gneiss units is often used to map nappe boundaries. The contact between the oceanic Zermatt-Saas zone and the continental Gran Paradiso massif is also a major lithologic boundary.

Feehan & Brandon (1999) have pointed out that the orientations of finite strains have a strong influence on the relation between ductile thinning of the overburden and exhumation. The exhumation of deeply subducted crustal material, especially during plate convergence, is one of the key geodynamic problems of mountain belt geology (Platt 1993). The key geodynamic problem for exhumation is thus that HP rocks need to move rapidly upwards within a zone of continuing convergence (subduction regime). Exhumation occurs through three processes: erosion, normal faulting, and ductile thinning. The processes are, also, of significance with respect to the formation of orogenic topography in addition to their contribution to synorogenic sedimentation (Ring et al. 1999). Ring et al. (2001b) showed that nappe emplacement will, in general, result in higher PT conditions in rocks of the lower plate, an inference which is in contrast to the commonly applied 'rules' of thrust faulting; in the latter case rocks with higher metamorphic grade should be tectonically above lower grade ones. In the author's opinion, however, is that the occurrence of high-grade on low-grade rocks requires that crustal shortening and nappe stacking is associated with reduction of the overburden (exhumation) of the overriding nappe.

In a detailed furtherance, however, the current work focuses on the timing of the nappe stacking in the Gran Paradiso massif as well as the relationship between the nappe contacts therewithin. It enables an assertive opinion that nappe stacking during high-pressure metamorphism in the Alpine subduction regime(s) was not triggered through simple shear. It has, rather, involved a component of vertical shortening, which is responsible for the development of subhorizontal foliation within the nappes.

In broad terms, the current documentation encompasses 6 consecutive chapters. Each of these concerns itself with a particular theme and all are corroborative to each other. Chapter 1 includes: location and accessibility of the area under consideration, objectives and aims of the study, and an outline pertaining to the finite strain and exhumation of the Gran Paradiso massif. Chapter 2 focuses on the geological background of the European Alps. Emphasis, however, has been placed on the Western Alps in general and the Gran Paradiso massif in particular. In addition, the history of deformation and metamorphism of the Gran Paradiso has been introduced. Within the scope of Chapter 3, methods of the finite strain analysis and results are presented. Chapter 4 deals with the implication of the finite strain data with respect to the exhumation of the Gran Paradiso massif and adjacent rock units. Whereas Chapter 5 highlights a discussion and summary, Chapter 6 is a conclusion for this dissertation.

1.2 Location and Accessibility:

The Gran Paradiso is a subcircular massif in the western Alps of northern Italy. It stretches for some 40 kilometres in diameter, and is bounded by latitudes 45°24′ and 45°48′N and longitudes 6°57′ and 7°33′E (Fig. 1.1). The massif is of mainly difficult access. It is reachable through railway net systems, highways and a wide range of motorable country tracts that criss-cross the western Alps of Italy and adjacent areas at large. In the field, however, rough topography is not uncommon. This may hamper accessibility; in particular rugged glaciated peaks that may reach about 4000 metres above the sea level.

In order to achieve the objectives of the current work (outlined earlier), the Gran Paradiso massif was subjected to a number of field excursions. These were undertaken between 2001 and 2003 in the following sequence:

- The first trip was from 24/8/2001 to 1/9/2001.
- The second trip was from 14/6/2002 to 10/7/2002.
- The third trip was form 21/7/2003 to 28/7/2003.

During the specified period of time some 167 samples were collected from the Gran Paradiso massif and environs. The purpose of the sampling was to perform petrographic, geochemical and strain analyses.

1.3 Scope of present work: aims and objectives:

Though the geology, structural framework, geochemistry and geochronology of the Gran Paradiso massif was reported upon by many authors, there still remain some uncertainties concerning the significance of pertinent, complex structural features. In essence, a common feature of the interiors of the Pennine gneiss nappes in the Western Alps, and also of the interiors of many other orogens, is that they have a penetrative subhorizontal foliation subparallel to the tectonic contacts with the under- and overlying nappes. In most cases, this foliation formed during thrusting of the nappes onto each other suggesting that nappe stacking was associated with vertical shortening. This observation contrasts with the widely held opinion that nappe formation in orogens is by simple-shear deformation.

In this dissertation the structure of the Gran Paradiso massif that consists of two subunits (Gran Paradiso and Erfaulet) and of the adjoining unit (Zermatt Saas zone), is discussed in detail. A conspectus of the objectives and aims of the study includes the following aspects:

(1) To study finite-strain in the Gran Paradiso massif and adjacent areas within the realm of the Italian Western Alps. (2) To elucidate whether ductile strain thereabout shows a relationship to nappe contacts. It is also aimed at shedding some light on the nature of the subhorizontal foliation typical for the Pennine gneiss nappes. (3) To investigate the relationship between thrusting and exhumation processes with reference to two structurally juxtaposed subunits (Gran Paradiso and Erfaulet). P-T data show that there is a crustal section of about ~11 km which is missing between the Gran Paradiso and Erfaulet subunits. Furthermore, to estimate the role of vertical ductile shortening and contributed to exhumation during nappe stacking. (4) To assess the difference in results of strain type between the Gran Paradiso and Erfault units.

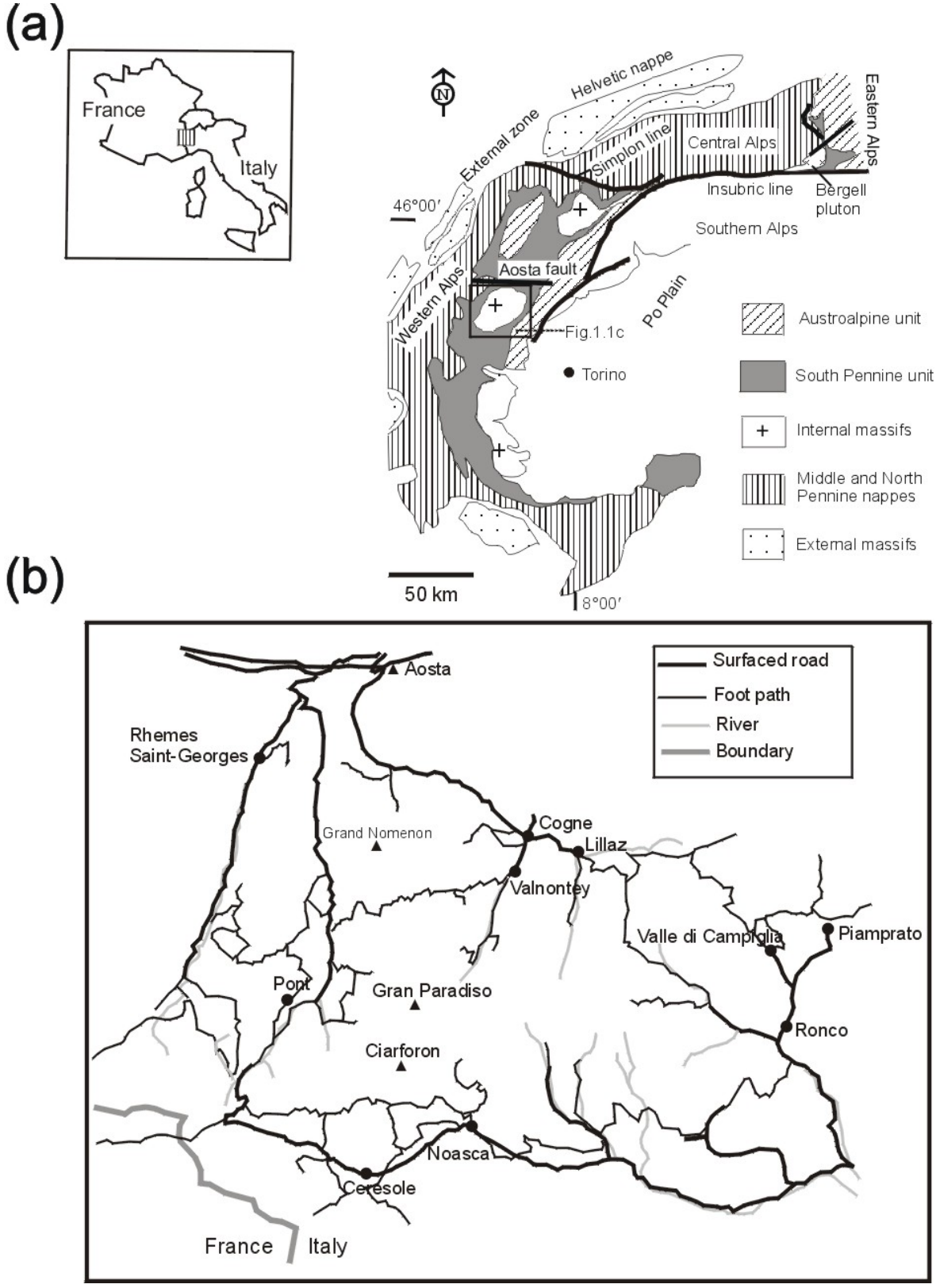

Fig.1.1: a) Tectonic sketch map of the western and central Alps. b) The location and accessibility of Gran Paradiso massif.

2. Geological Overview

2.1. The History of the European Alps

The European Alps have been studied for at least 150 years, longer than any other orogen in the world. It forms part of extensive arcuate mountain chain and young extensional basins created in the Mediterranean region during convergence between the African and European plates. Available data about the tectonic evolution of this orogen (e.g. Trümpy, 1980; Coward and Dietrich, 1989; Pfiffner, 1992; Platt, 1997) reveal that the history of the Alps began early in Mesozoic time, when most of the continental masses of the world were joined together in the supercontinent Pangea. During the Triassic, much of the Western Europe lay in the continental interior and experienced desert conditions. The associated deposition of continental clastics and evaporates was to play an important role in later Alpine tectonism. Farther south, in the shallow seas bordering the great oceanic gulf known as Tethys **(Fig.2.1a)**. As a result of the break up of the Pangea and the separation of Laurasia and Gondwana the central Atlantic began to open in the early Jurassic. Associated strike-slip between the Iberia and Africa/Adriatic plates gave rise to the South Pennine (Piemont or Ligurian) ocean**,** which formed the westernmost part of Tethys **(Fig.2.1b)**. The Alpine orogeny is a result of the closure of this ocean.

The northern margin of the South Pennine Ocean was a classic passive continental margin that extended from southeastern France through Switzerland to Austria. The southern margin of the South Pennine Ocean in the region of the Alps was the rifted border of a continental block known as Adria. Adria is the continental crust that underlies the present shallow Adriatic Sea and adjacent areas, including northern Italy.

During the Mesozoic, Africa (including Adria) moved southeast and then east relative to Europe, rotating slowly counterclockwise **(Fig.2.1c)**. About the middle of the Cretaceous, Africa started to move northeast relative to Europe, and subduction of the Neotethys began at the northern margin of Adria **(Fig.2.1d)**. From this time on the Alps began to evolve by the progressive subduction and accretion of sediment and crustal slices from the floor of the Neotethys. By early Tertiary time, the Neotethys had closed, and the

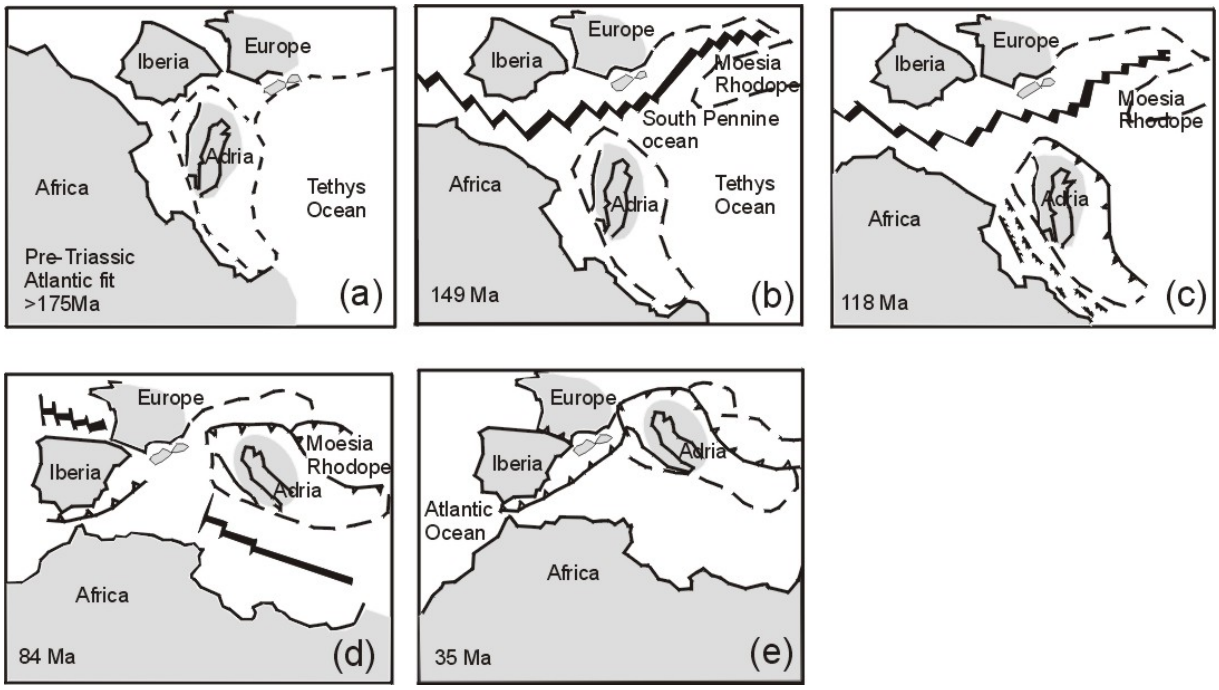

Fig.2.1: Plate-tectonic evolution of the Alpine region from Permian to Tertiary. Africa/Europe relative plate motions are from Dewey et al., (1989), based on analysis of Atlantic magnetic anomalies and transform faults. (a) Pre-Triassic configuration: Africa, Europe, Iberia, and Adria all form parts of pangaea, surrounding a gulf of the Thethys ocean. (b) Late Jurassic: opening of the southern and central Atlantic is transferred eastwards to open up the Neothys Basin between Africa and Europe. Adria remains attached to Africa. (c) Mid-Cretaceous: Adria starts to rift away from Africa, and convergence begins on its northern margin. This causes high-P/low-T metamorphism of crustal rocks, now found in the internal zones of the Alps. (d) Late Cretaceous: Adria moves northwards away from Africa and towards Eruope, forming an accretionary wedge on its northern margin. (e) Oligocene: Collision starts between Adria and Europe, to form the present collisional chain of the Alps (after Platt, 1997).

European continental margin entered the subduction zone **(Fig.2.1e).** This marks the start of continental collision, and shortening and deformation of both margins and of the oceanic domains between them continued until the Pliocene to the recent (Platt, 1997).

From the structural point of view, the Alps can be divided into several regions with different structural styles and histories of deformation. These differences reflect differences in stratigraphy, tectonic setting, and the physical conditions and duration of deformation. The main tectonic and palaeogeographic domains of the Alps, from bottom to top, are the Helvetic unit, the Penninic unit, and the Austroalpine / South Alpine units **(Fig.2.2)**. The Insubric line marks the boundary between the Southern Alps and the Austroalpine (+Pennine) domain. In the western and central Alps, the Penninic domain is extensively exposed, while in Eastern Alps this domain is hidden beneath the Austroalpine and reappears only in the two windows the Engadine and Tauern windows. The Helvetic and Penninic units represent the shelf, slope and adjacent ribbon continents related to the European continental margin and the oceanic domains, whereas the Austroalpine nappes and South Alpine units are related to the overriding African plate (e.g. Hsü, 1989). The Helvetic domain is subdivided in a series of nappes. It consists of a Variscan crystalline basement and a post-Variscan, mainly Mesozoic sedimentary cover. The crystalline basement, which consists of Variscan (or older) is exposed in the so-called External Crystalline Massifs. The Penninic domain is a composite realm, which includes both continent and ocean-derived units. The continental units are the external Briançonnais Zone or Grand Saint Bernard composite nappe, and the Internal Crystalline Massifs Monte Rosa, Gran Paradiso and Dora Maira. The Internal Crystalline Massifs are overlain by the oceanic derived units of the Piemonte Zone (Castelli and Compagnoni, 1994) **(Fig.2.2)**.

Remnants of the South Pennine are represented by ophiolitic rocks occurring in different structural units of the Alpine nappe pile, e.g. the Zermatt-Saas and Antrona ophiolites (Bearth, 1953, 1962, 1967, 1973; Gosso et al., 1979; Milnes et al., 1981; Beccaluva et al., 1984; Platt 1986; Pfeiffer et al., 1989; Polino et al., 1990). The restoration of the paleogeography of the Alpine units is a longstanding problem due to polyphase deformation and metamorphism during the complex Alpine history. Most authors agree that two partly oceanic basins existed in the Penninic zone in Jurassic to Cretaceous time, the north Penninic or Valaisan basin and the South Penninic. The basins were separated by the Briançonnais continental fragment (Platt, 1986; Froitzheim et al., 1996; Froitzheim, 2001). The Valaisan basin consisted of thinned continental and possibly oceanic crust (Trümpy,

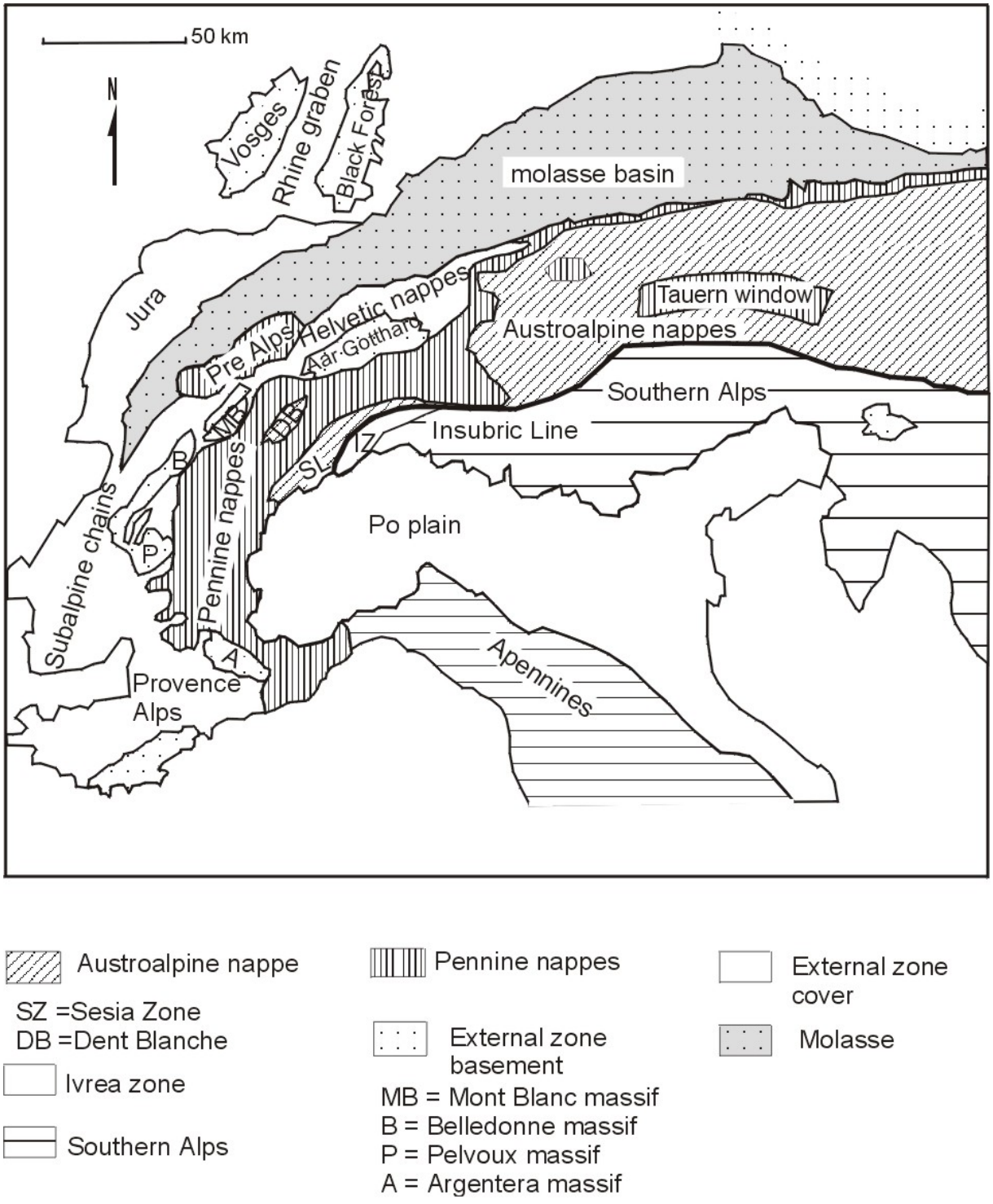

Fig.2.2: Main tectonic and Palaeographic units of the Alps.

1980; Polino et al., 1990; Stampfli, 1993; Stampfli and Marchant 1997). On the other hand, the Ligurian basin separated the Briançonnais and the African continent to the south (Bearth, 1967, 1973; Dal Piaz, 1974; Platt 1986; Polino et al., 1990).

2.2. Structure of the western Alps:

In the previous discussion, it has been explained that the closure of Neotheys by SE-directed subduction, the accretion of crustal fragments during this convergence and complex interleaving of different tectonostratigraphic units by regional overthrusting and extension have resulted in the formation of the Alpine Orogen (Platt, 1986; Coward and Dietrich, 1989; Schmid et al., 1996; Pfiffner et al., 1997; Schmid and Kissling, 2000; Stampfli, 2000). In the metamorphic areas of the western Alps, components of the European (Briançonnais) microcontinent (Penninic Domain), the Adriatic microcontinent (Austroalpine Domain) and the interjacent oceanic plate (south Penninic) are exposed **(Fig.2.3)**. Penninic and Austroalpine basement rocks contain evidence of pre-Alpine metamorphism. However, all three major units have locally developed eclogite-facies rocks of the Alpine age that developed during subduction (Ernst and Dal Piaz, 1978).

The Western Alps are separated from the Central Alps by the Simplon line (Bearth 1956), which is a moderately southwest-dipping, ductile shear zone that has been active between 18 and 12 Ma (Mancktelow 1990). Further southwest, the Austroalpine and upper Pennine nappes of the Dent Blanche/Monte Rosa region were displaced across the extensional Aosta fault towards the northeast, relative to the upper Penninic units of the Gran Paradiso area in the footwall of the fault **(Fig.2.3)**. Like the Simplon fault, the Aosta fault cuts structures, which are due to Cretaceous and Paleogene deformation. Therefore, the Aosta fault is also of late Alpine age and probably formed during the same extensional event as the Simplon fault (Ring 1994; Bistacchi et al. 2001).

In the following, a brief description of each major tectonic unit of the western Alps from bottom to top is given, based mainly on Escher and Beaumont (1997).

European margin: The External massifs and their cover (extending northward underneath the Molasse basin) and the Helvetic cover nappes, whose crystalline substratum has to be looked for within the deepest part of the Lepontine dome (lowest Penninic nappes). The External massifs are updomed basement nappes (i.e Mont Blanc massif,

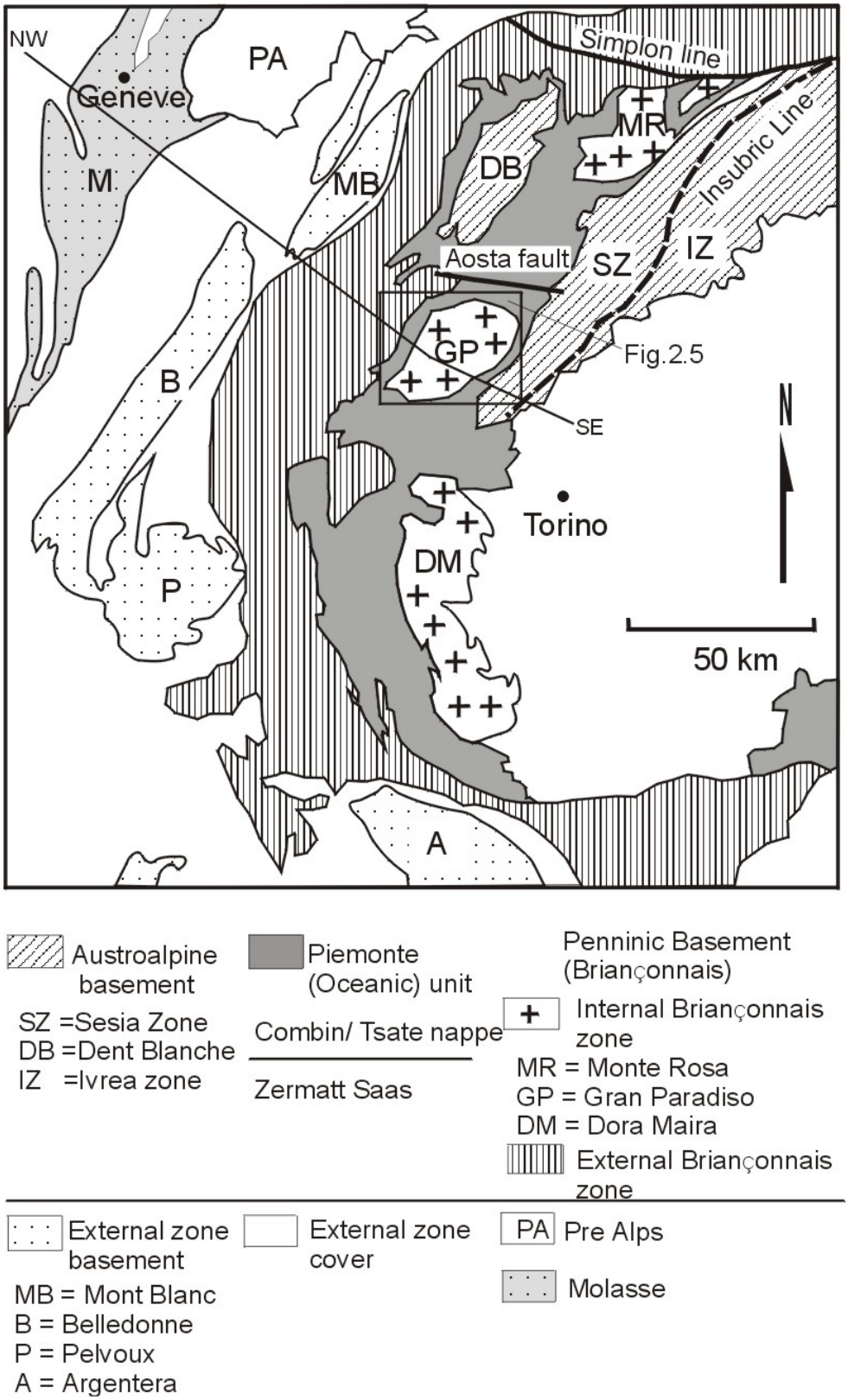

Fig.2.3: Simplified geological map of western Alps. Cross-section SE-NW indicating of the geophysical-geological transect of the western Alps in Fig.2.4 from Schmid and Kissling (2000).

Aiguilles Rouges massif, Belledonne massif, Pelvoux and Argentera massifs) consisting of a polymetamorphic basement intruded by Variscan granitoids **(Figs.2.3, 2.4)**. Most Alpine structures show an initial N- to W- vergence, whereas later backfolding (S-vergence) is only observed southeast of the Aiguilles Rouges massif. The Alpine deformation took place under greenschist facies conditions in the external parts, whereas in the more internal parts amphibolite facies is recorded. The later backfolding was characterized by retrograde greenschist facies metamorphism (Escher and Beaumont, 1997; Pawlig, 2001). During formation of the basement nappes, the cover was detached, displaced towards the northwest and is now forming the Helvetic cover nappes. Triassic evaporites served as detachment horizons.

Valais Ocean: Remnants of the Valais oceanic lithosphere and associated sediments, i.e. the Sion-Courmayeur zone, are found in a discontinuous zone at the boundary between nappes derived from the European crust and those of the Briançonnais microcontinent **(Fig.2.4)**. The ductile oceanic sediments of the Valais accretionary prism must have formed a weak structural link between the European and Briançonnais nappe piles (Trümpy, 1980; Platt, 1986; Polino et al., 1990; Escher and Beaumont, 1997; Pawlig, 2001). The Valais Ocean opened near the Jurassic-Cretaceous boundary and the remnants of this ocean presently define a northern Alpine suture zone, which closed during the Late Eocene. Those remnants are mainly made up by calcschists, schists, limestones, quartzites and conglomerates with locally occurring mafic to ultramafic rocks.

Briançonnais microcontinent: The basement nappes derived from the Briançonnais upper continental crust form a central zone between the Valais and the Piemont ophiolitic nappes (Platt, 1986; Froitzheim et al., 1996; Froitzheim, 2001) **(Figs. 2.3 and 2.4)**. The Briançonnais microcontinent basement is preserved in the form of the Tambo-Suretta, Maggia and the Grand St. Bernard nappe in the eastern, central and western Penninic realm respectively. The Grand St. Bernard nappe is separated into several independent nappes, the Zone houillère, the Pontis and the Siviez Mischabel nappes, and the Mont Fort nappe (Ballèvre and Merle 1993).

The more internal part of the Briançonnais nappe pile observed in the Western Alps is characterized by three large basement nappes, the Dora Maira massif, the Gran Paradiso

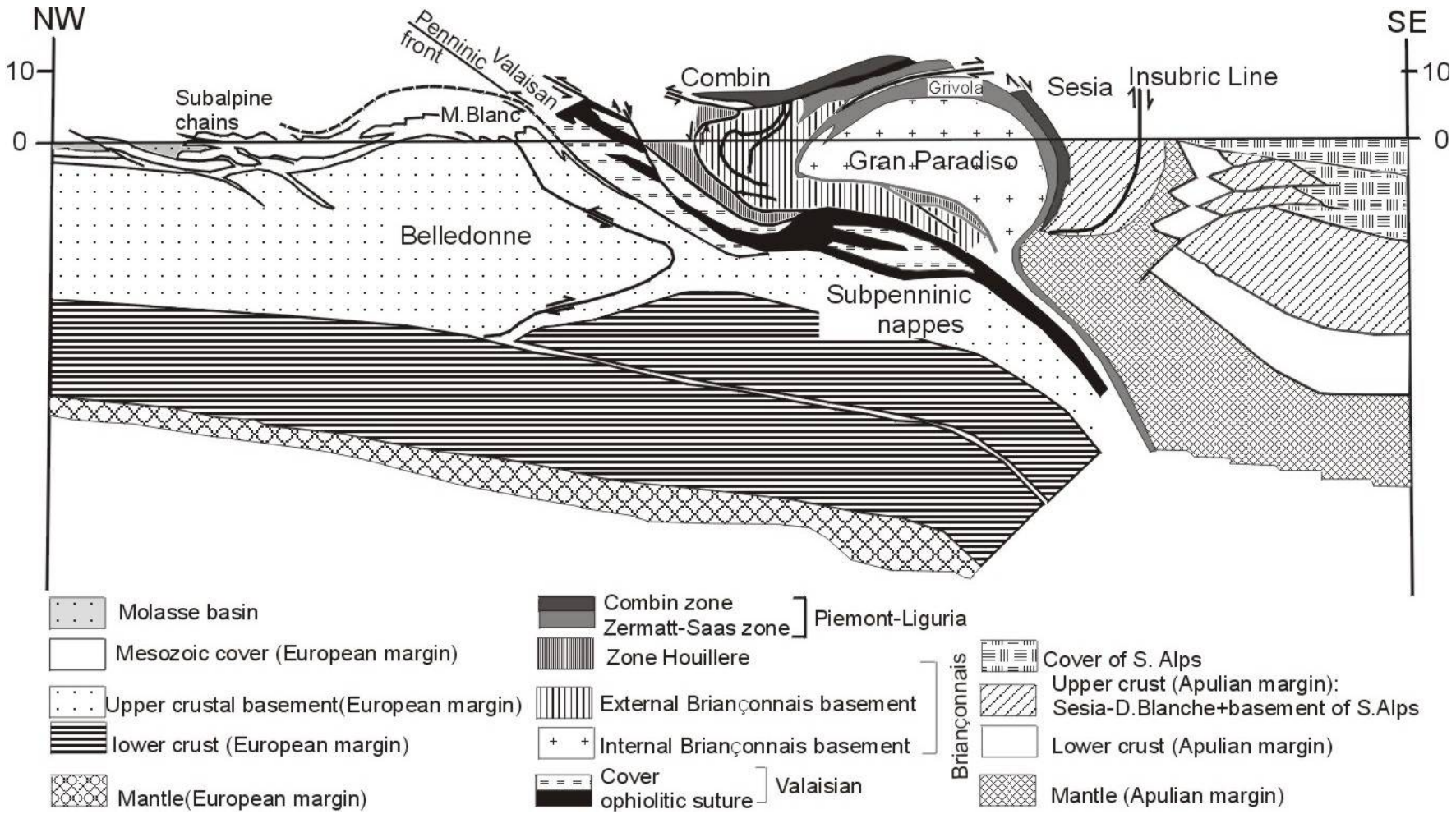

Fig.2.4: The schematic geophysical-geological sections through the western Alps. (ECORS-CROP) After Schmid and Kissling (2000).

massif and Monte Rosa nappe. The massifs form windows within the South Pennine oceanic units (Piemont Zone); therefore, they are regarded as internal massifs. They commonly consist of voluminous, Carboniferous and Permian granites intruded into mica schists (Bearth, 1952; Compagnoni et al., 1974; Dal Piaz and Lombardo, 1986; Chopin et al., 1991; Paquette et al., 1999; Brouwer, 2000; Bertrand et al., 2000). Partially, remnants of a post Variscan cover are still attached to the basement rocks of all three massifs (Bearth, 1952; Vialon, 1966; Compagnoni et al., 1974; Bearth and Schwander, 1981; Dal Piaz and Lombardo, 1986; Borghi et al., 1996; Froitzheim, 2001). All three continental basement units were deformed and metamorphosed under high to partly ultrahigh pressure metamorphic conditions during the Alpine orogeny implied by occurrences of eclogites and partially coesite relics (Dal Piaz, 1966; Wetzel, 1972; Klein, 1978; Chopin, 1984; Dal Piaz and Lombardo, 1986; Massonne and Chopin, 1989; Chopin, et al., 1991; Schert et al., 1991; Henry et al., 1993; Gebauer et al., 1997; Brouwer, 2000; Pawlig, 2001).

Piemont-Liguria (South Penninic) Ocean: Remains of the Piemont oceanic domain form an important and continuous zone separating the Briançonnais units from the Austroalpine unit **(Figs. 2.3 and 2.4)**.The Piemont unit comprises rocks of ophiolitic affinity that can be subdivided into two main lithotectonic units; the structurally lower Zermatt-Saas Zone, metamorphosed at eclogite facies conditions, and overlying blueschist facies Combin Zone. The Combin zone is separated from the underlying Zermatt-Saas zone by the Combin fault (Ballèvre and Merle 1993; Ring 1995).

The Zermatt-Saas zone is made up of serpentinite, metagabbro, metabasalt, metachert, conglomerate and Bündnerschiefer (e.g. Bearth 1976). PT conditions in the Zermatt-Saas zone have been estimated at 550-600°C and 18-20 kbar (Reddy et al. 1999); rare lenses of ultrahigh-pressure rocks yielded 590-630°C and 26-28 kbar (Reinecke 1991). The oceanic Antrona zone contains ophiolitic rocks similar to those of the Zermatt-Saas zone and is hence correlated to that zone (e.g. Pfeiffer et al. 1989).

The heterogeneous Combin zone marks the boundary between the Austroalpine units and the underlying Pennine nappes, the Zermatt-Saas Zone, (e.g. Bearth 1976; Marthaler & Stampfli 1989). It contains continent-derived Permo-Triassic to Liassic metasediments overlain by calcschist (Bündnerschiefer) and metavolcanics with interbedded manganiferous metachert, which collectively indicate a deep oceanic setting (Dal Piaz & Ernst 1978). Two main units characterize the Combin Zone. The first one is made up by marly metasediments,

mainly calcschists, which were derived from basaltic volcanics and gabbros as well as some serpentinites and Mn-quartzites indicating the origin from an oceanic unit. According to Sartori (1990), this unit is referred to as the Tsatè nappe and is probably the remnant of an accretionary prism that was formed during the subduction and closure of the oceanic domain. The other one is a sedimentary sequence ranging from Permian siliceous conglomerates to Triassic quartzites and dolomitic marbles deposited on top of a continental crust. Also some calcareous sequences of presumed Jurassic age are present (Ballèvre and Merle, 1993).

Austroalpine and south Alpine nappes: The continental Austroalpine units can be separated into the Dent Blanche nappe and the tectonically underlying Sesia zone (Ballèvre et al. 1986) **(Fig. 2.3)**. The base of the Sesia zone represents part of the pre-Alpine Austroalpine basement thrust westwards over the Penninic basement and Piemonte oceanic material (Compagnoni, 1977). Three main lithotectonic units have been recognised in the Sesia Zone (Compagnoni et al., 1977).

The Eclogite Micaschist Complex is a several kilometre thick unit comprising pre-Alpine high-grade paragneiss with marbles, amphibolites and granulites intruded by Variscan gabbros and granites and metamorphosed at eclogite facies (Vuichard and Ballevre, 1988; Pognante, 1989). The eclogite facies assemblages (T~ 500-600°C, P>13 kbar) are locally overprinted by a later, greenschist facies metamorphism (Compagnoni et al., 1977).

The Gneiss Minuti Complex contains fine-grained quartz-feldspar schists, with augen orthogneiss, micaschists and metagabbros. These represent pre-Alpine lithologies overprinted by Alpine greenschist facies metamorphism and deformation. The contact of the Gneiss Minuti Complex and underlying Piemonte oceanic unit is a high-strain zone accommodating top-to–SE extension after earlier thrusting (Wheeler and Butler, 1993; Reddy et al., 1999b).

The Seconda Zone Diorito Kinzigitica (IIDK) forms the structurally highest unit in the Sesia Zone and comprises pre-Alpine amphibolite facies rocks similar to those found in the Ivrea Zone (Compagnoni et al., 1977). This pre-Alpine metamorphism is also overprinted by a localised low-greenschist facies metamorphism, evident within shear zones close to its margins (Lardeaux et al., 1982; Ridley, 1989), which is of Alpine age (Reddy et al., 1996; Pickles et al., 1997).

Further west, the Austroalpine basement forms the Dent Blanche nappe (Fig.2.3). The Dent Blanche nappe is subdivided into the high strain Arolla schist, which preserves Alpine greenschist facies metamorphism and is thought to correlate with the Gneiss Minuti Complex (Ballèvre et al. 1986).

The Southern Alps are separated from the other Alpine complexes described above by a major tectonic feature, the Insubric Line, which is replaced eastward by the Giudicaria Line and Alpine Dinaric line (Frey, et al., 1974). The south Alpine continental lithosphere of the Western Alps is mainly represented by the Ivrea and Strona-Ceneri Zones, which are separated from the Sesia Zone to the north by the Canavese Line. The Ivrea zone is a subvertical cross-section from the Moho to the continental crust (Mehnert, 1975; Henk et al., 1997). Gneisses that contain partially mafic and ultramafic rocks displaying granulite facies metamorphism can be found (Zingg et al., 1990). The mid-crustal upper part, the Strona-Ceneri Zone, is formed by a monotonous series of paragneisses, schists and minor amphibolites. An early, eclogite-facies metamorphism took place before the Ordovician and was followed by two medium-grade metamorphic overprints in early Ordovician and in Variscan time. Near the contact to the Ivrea Zone, the Strona-Ceneri Zone also experienced an early Permian heating event, which is represented by several granite intrusions (Pawlig, 2001).

2.3. Gran Paradiso massif:

Petrological work in the Gran Paradiso massif in western Alps was pioneered by many authors (Compagnoni et al. 1974; Compagnoni & Prato 1969; Vearncombe 1983, 1985; Benciolini et al., 1984; Dal Piaz and Lombardo, 1986; Goffé and Chopin, 1986; Pognante et al., 1987; Ballévre, 1988; Biino and Pognante, 1989; Borghi et al., 1992; Compagnoni et al. 1994). The Gran Paradiso massif consists of two subunits **(Fig.2.5)**. (1) The upper Gran Paradiso unit (also known as polymetamorphic complex) is made up of metasediments (Gneiss Minuti) into which the granitic precursor of widespread augengneiss is intruded during the Permian (Bernard 2000). (2) The tectonically underlying Erfaulet unit (monometamorphic complex) comprises metaconglomerate, metapelite and metagranite/augengneiss. Compagnoni et al. (1974) assigned a Late Carboniferous and/or Permian age to the conglomerate. In the southwestern part of the Gran Paradiso massif, the Bonneval gneiss crops out below the Gran Paradiso unit. It is a commonly mylonitic,

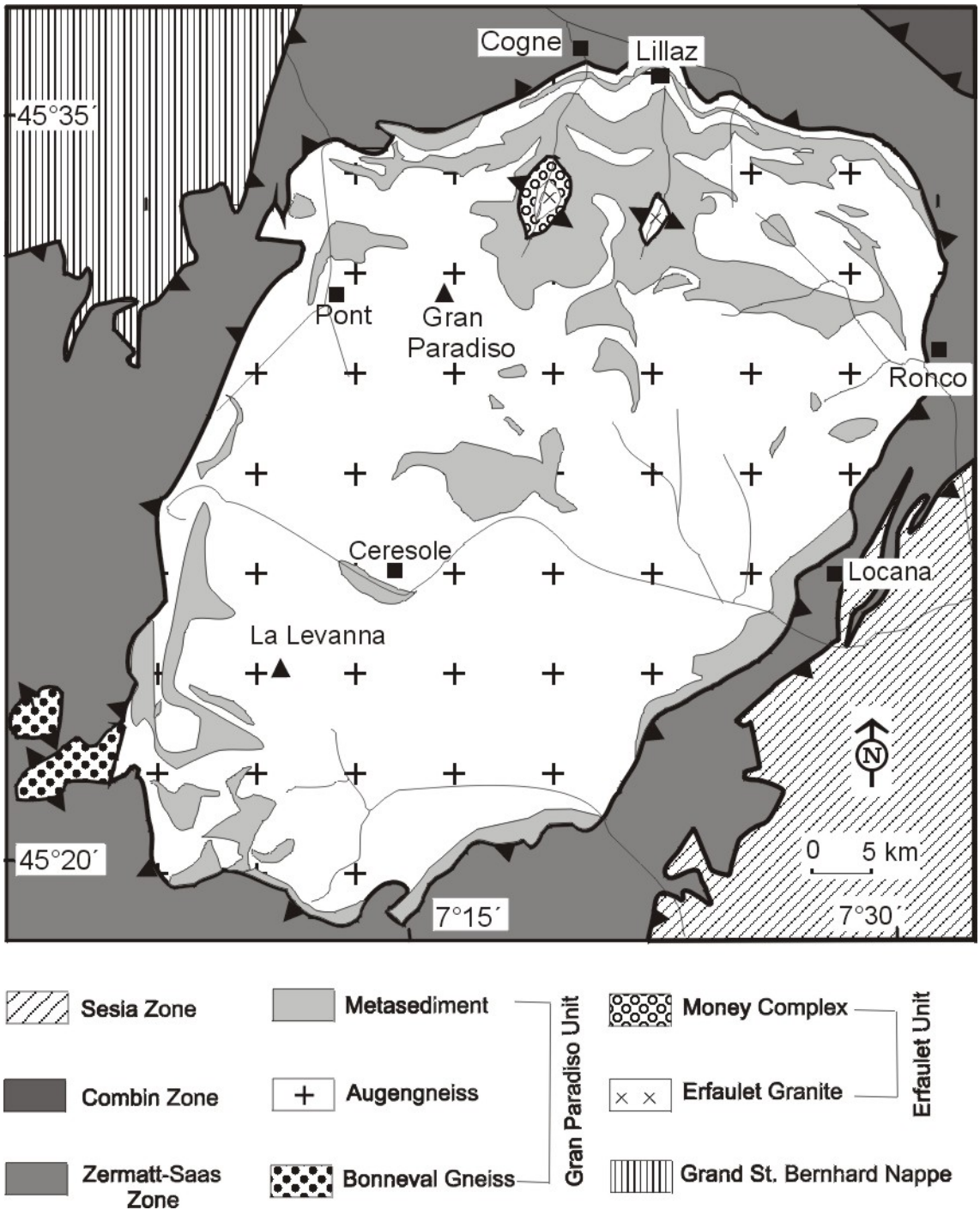

Fig.2.5: Tectonic map of the Gran Paradiso massif.

banded gneiss derived from Permian volcanics and sediments (Bertrand 1968). The Bonneval gneiss is separated from the augengneiss by a fault zone in which dolomite, cargneule, anhydrite and Bündnerschiefer occur (Bois & Fabre 1956). The structural studies suggest that The Bonneval gneiss was part of the Gran Paradiso nappe during Alpine orogenesis (Vearncombe 1985).

The monometamorphic complex (the lower Erfaulet unit) separated from the polymetamorphic complex (the upper Gran Paradiso unit) by a subhorizontal overthrust contact (Compagnoni et al. 1974). This contact cuts the Erfaulet unit and Gran Paradiso unit at a very low angle (Vissers, and Compagnoni, 1984). Compagnoni et al. 1974 suggested that the complicated geometry of the porphyritic metagranites (augengneisses) and associated polymetamorphic metasediments resulted from the deformation related to overthrusting.

Borghi et al. (1996) reported a summary on the reconstruction and interpretation of the P-T history of the eclogitic Penninic units of the western Alps using geothermobarometers to determine peak metamorphic conditions. In the Gran Paradiso massif, pressure is in the range 8 to 15 kbar and temperatures are between 400 and 550°C (Vearncombe 1983; Benciolini et al., 1984; Dal piaz and Lombardo, 1986; Goffé and Chopin, 1986; Pognante et al., 1987; Ballévre, 1988; Biino and Pognante, 1989; Borghi et al., 1992; Compagnoni et al. 1994). Biino and Pognante (1989) suggested for the eclogite facies metamorphic peak P between 12 and 20 kbar and T around 500°C, which are higher than those proposed by most of previous authors (Benciolini et al., 1984; Dal piaz and Lombardo, 1986; Pognante et al., 1987; Ballévre, 1988). However, these physical parameters are in good agreement with the estimates of Goffé and Chopin (1986), and with the estimates of 500±50°C and 10-16 kbar of Le Goff and Ballévre (1990) based on geothermobarometry of albite-garnet orthogneiss modelled in the KCFASH system (Compagnoni et al. 1994).

On the ground of different lines of petrological and textural evidence, Le Goff and Ballévre (1990) conclude that the Gran Paradiso Massif was submitted to lower pressures than the Sesia Zone. By using the maximum celadonite content (Si=3.6 at pfu) of potassium white micas in the phengite-quartz-K-feldspar-biotite assemblage (Massonne and Schreyer, 1987) and taking a peak metamorphic temperature of 500±50°C from the chloritoid-bearing schists (Chopin, 1981), Massonne and Chopin (1989) estimate two groups of pressures of

11.6±1 and 14.4±1 kbar, Erfaulet and Gran Paradiso units respectively. This was suggested as evidence of at least two major nappe units in the Gran Paradiso massif (Compagnoni et al. 1994). In addition, Borghi et al. (1992, 1994) showed that during the Alpine orogeny, maximum metamorphic conditions of both units were different: peak PT conditions of the Gran Paradiso unit were 12-14 kbar and 500-550°C, whereas high-pressure metamorphism of the Erfaulet unit occurred at 11-13 kbar and 450-500°C.

The cumulative evidence summarized above indicates that the Gran Paradiso unit was subjected to eclogite metamorphism of T= 500°C and P= 12-14 kbar, i.e. P-T conditions very close to the low-albite breakdown reaction to produce jadeite + quartz. Therefore, the rare occurrence of jadeite in the Gran Paradiso may be explained either with a slightly higher or lower temperature in different parts of the massif, or with the lack of jadeite because of reaction kinetic factors (Le Goff and Ballévre, 1990).

The metamorphic evolution after the high-pressure overprint was similar in both units (Gran Paradiso and Erfaulet units) indicating that they were juxtaposed during and/or soon after the peak of high-pressure metamorphism. There are no age data, which constrain high-pressure metamorphism or associated deformation in the Gran Paradiso massif. Available Sm/Nd data for pyrope and the U/Pb ages for zircon from the correlative Dora Maira massif have been interpreted to date the high-pressure event at 38-40 Ma (Tilton et al. 1991). Zircon and apatite fission-track ages of ~30 Ma and 24-19 Ma, respectively (Hurford and Hunziker,1989) indicate cooling after the greenschist-facies overprint in the Gran Paradiso massif.

2.4. Review of deformation history of the Gran Paradiso massif and adjacent areas:

In the Gran Paradiso massif, some authors show that the Gneiss Minuti was intruded by porphyritic granite during late Variscan times. Total Pb zircon dates range between 301 and 350 Ma, and reflect crystallization of the granite (Pangaud et al. 1957; Buchs et al. 1962*;* Chessex et al. 1964). These dates are likely affected by inherited zircons. Recently, a 269±6 Ma SHRIMP U-Pb crystallization age of zircons from augengneisses in the south-western part of Gran Paradiso was published (Bertrand et al. 2000). This intrusion age of the Gran Paradiso granites coincides nicely with the magmatic age of similar granites in the

Dora Maira massif, commonly considered structurally and palaeogeographically equivalent to the Gran Paradiso massif, which has recently been determined at 275 Ma by SHRIMP (Gebauer et al. 1997). During Alpine times, the granitic rocks were transformed into augengneisses. Callegari et al.1969; Compagnoni and Prato 1969, reported intrusive contacts between the augengneisses and the Gneiss Minuti as well as Compagnoni et al 1974 show this contact between the augengneisses and metabasites, which confines the age of the metabasites to the upper Carboniferous or lower Permian, and demonstrates that the high-pressure assemblages found in the metabasic rocks must be related to Alpine metamorphism.

During this metamorphic evolution the rocks involved were intensely deformed, leading to the development of various generations of deformational structures. These were investigated by many authors (e.g. Milnes, 1978; Platt and Lister, 1978; Milnes et al., 1981; Vissers & Compagnoni, 1984; Vearncombe, 1985; Massonne and Chopin, 1989; Borghi et al. 1994). In particular, Vissers & Compagnoni (1984) advocate successive and/or overprinting structures that range from D_1 to D_5. Two of these (D_1-D_2) predate the main phase; D_3 comprises the main-phase structures, whereas D_4 and D_5 are superimposed on the main-phase foliation.

In accord with the work of Vissers & Compagnoni (1984), it may be summarized that D_1 structures include few tight cm-scale folds of a compositional layering refolded by D_2 folds. They occur in the polymetamorphic metasediments of the Gran Paradiso unit, which indicates that the polymetamorphic metasediments were deformed before they were intruded by multiple generations of porphyritic granites. Moreover, Vearncombe (1985) reported that within metagabbro and metalavas in the Zermatt-Saas Zone, a series of less deformed pods unaffected by the extensive D2 deformation are recognised. Within these pods, rare eclogites, omphacite-bearing rocks as well as glaucophane eclogite are preserved. The glaucophane needles within the pods are usually aligned and constitute a foliation (D_1) that predates the nappe pile.

Tight to isoclinal D_2 folds refolded by D_3 folds occur at various localities in the basement, the Combin zone, and the Zermatt-Saas Zone with its contained ophiolites. The D_2 folds display a shallow W-ward plunging axis. A penetrative foliation is subparallel to the axial planes of these folds. The Zermatt-Saas Zone often posses an LS fabric with the elongation lineation running approximately E-W. Despite difficulties in deducing the age of particular fabrics in the Zermatt-Saas Zone, it is suggested that much of this fabric is D_2 in

origin (Vearncombe, 1985). The Combin zone also possesses a prominent LS fabric, which parallels that in the basement and Zermatt-Saas Zone. The Sesia zone, especially that region adjacent to the Zermatt-Saas Zone, has a weak, usually planar fabric. In the augengneisses, local relics of a pre-mainphase gneissic layering presumably represent D_2 structures.

The third Alpine deformation is a major phase of folding. The D_2 fabric is folded, D_2 folds are locally refolded and a new axial planar D_3 fabric developed. Greenschist facies minerals usually define this fabric. In the metasedimentary rocks, the morphology of the foliation varies from a differentiated layering, with relics of crenulations in quartz rich microlithons, to a pervasive schistosity. In many localities, the gneissic layering in the augengneiss can be shown to be continuous with the D_3 axial-plane foliation in the metasediments. Locally, WNW-trending extension lineations developed in the plane of the main-phase foliation. D_3 fold axes commonly are subparallel to these lineations, which possibly indicate a reorientation of the fold axes towards the D_3 finite extension direction. Quartz mylonites occur in layers subparallel to the main phase foliation. The mylonite zones could reflect the effects of ongoing D_3 deformation localized in quartzite layers or, alternatively, be referred to a younger deformation episode, which predates D_5 described below. The main-phase (D_3) foliation is commonly defined by oriented blue-green amphibole, epidote and chlorite, indicating greenschist-facies conditions during the development of the D_3 structures and suggesting a pre-D_3 age of the Eoalpine relics, which are mostly observed as inclusions in garnet porphyroblasts. Greenschist metamorphism in the Gran Paradiso massif is characterized by the widespread blastessis of albite and chlorite, and concomitant replacement of the Eoalpine mineral assemblages.

Two generation of structures (D_4 and D_5) are superimposed on the main-phase foliation. The D_4 generation of structures comprises centimetre to millimetre scale ductile shear zones, which deform the main-phase foliation either in single or in conjugate sets, the latter in a symmetric arrangement with respect to this foliation (Vissers & Compagnoni, 1984). They indicate deformation with a component of finite extension subhorizontal to the main-phase foliation (Platt & Vissers, 1980) and represent the effect of high-strain D_3 deformation.

The D_5 generation of deformational structures includes a moderately south-dipping crenulation cleavage parallel to the axial planes of minor folds, which affect the main-phase foliation and the quartz mylonites (Vissers & Compagnoni, 1984). These structures are rare and mainly occur in a domain underneath the augengneisses of the major fold structure.

They might correspond to the doming of the main-phase foliation. Extensional shear bands in Zermatt-Saas Zone of the type described by Platt and Vissers (1980) are grouped in this event (Vearncombe, 1985). The D_4 and D_5 generations of deformational structures apparently postdate major albite growth, suggesting, that these structures developed in the waning stages of the Alpine metamorphic evolution.

Vissers & Compagnoni (1984) suggest that structural analysis indicates that the geometry of the rocks of the Gran Paradiso unit primarily results from large-scale folding and concomitant development of the axial-plane (main-phase) foliation. The large-scale folding is related to individualisation of the Gran Paradiso unit, that is to say that the Gran Paradiso unit is a gneiss-cored fold nappe. Furthermore, the main-phase structures postdate the Eoalpine HP assemblages and predate widespread porphyroblastesis of albite. The data suggest individualisation of the Gran Paradiso unit between the Eoalpine HP metamorphism and greenschist facies overprint. This result correlates well with the timing of nappe development in the Zermatt-Saas Fee area (Dal Piaz et al., 1972).

3. Strain and Structural analysis

3.1 Definition and strain parameter:

Strain is the geometrical expression of the amount of deformation caused by the action of a system of stresses on a body. In other words, strain can be defined as the change in size and shape of a body resulting from the action of an applied stress field. The strain is *homogeneous* if the changes in size and shape are proportionately identical for each small part of the body and for the body as a whole. Also, the strain is *inhomogeneous* if the changes in size and shape of small parts of the body are proportionately different form place-to-place and different from that of the body as a whole. Strain is expressed as dilation (volume change) or distortion (shape change), or as a combination of these processes.

Many authors presented the parameters of strain and show the quantity of the deformation. Also, they determined the symmetry of strain (oblate vs prolate) and the type of strain (constrictional vs flattening). Strain may be measured in two ways:

(1) *Linear strain*: The change in absolute length is an inadequate measure of the deformational state of a line segment, because for a given change in length, the intensity of the change is much greater for a short line segment than for a long one (Park, 1983). Two measures in common use are the stretch (S) and the extension (e).

$$S = l_f / l_i$$

where l_f is the ratio of the deformed length and l_i the undeformed length.

$$e = (l_f - l_i) / l_i$$

where l_i is the original length and l_f the new length of a line. Note that a positive value of e is an elongation whereas a negative value of e is a shortening.

(2) *Shear strain*: A body can also change shape without changing volume. Changes in shape are described by changes in the angle between pairs of lines that are initially perpendicular.

$$\gamma = \tan\Psi$$

where Ψ is the deflection of an originally right angle.

Principal strain axes consist of three mutually perpendicular axes X, Y and Z, which are parallel respectively to the directions of greatest, intermediate, and least elongation of the strain parallelepiped. In addition, *the strain ellipsoid* are maximum, intermediate and minimum axes X = 1 + e_x, Y = 1 + e_y and Z = 1 + e_z respectively, which is the shape taken up by a deformed infinitesimal sphere of unit radius.

If the orientations of the principle strain axes X, Y and Z have not changed during the deformation, the strain may be described as irrotational and the process is generally known as *pure shear*. Where a change in orientation has occurred, the strain is described as rotational and the process is known as *simple shear*.

Volumetric strain: Changes in volume commonly shape changes during deformation, and if these are not recognized they can cause misleading estimates of the principal strain ratios. The volume change (ΔV) is given by:

$$\Delta V = (V_f / V_i) / V_i$$

where V_f and V_i are the volumes in the deformed and undeformed states respectively.

Since the volume of the strain ellipsoid is 4/3л (X * Y * Z) derived from a unit sphere of volume 4/3 л.

$$Sv = V_f / V_i = Sx * Sy * Sz$$

Three special cases of homogeneous strain can be distinguished by particular ratio of the principal strains X, Y, and Z (Park, 1983). In the general case, the three axes are unequal and X > Y > Z. The special cases are:

(a) X > Y = Z prolate strain ellipsoid

This type of strain involves uniform extension in the X direction and equal shortening in all directions at right angles to it.

(b) X = Y > Z oblate strain ellipsoid

This type of strain involves uniform shortening in the Z direction and equal extension in all directions at right angles to it.

(c) X > Y = 1 > Z plane strain

This type of strain is distinguished by the intermediate principal strain axes remaining unchanged (i.e. Y has unit length). X is extended and Z is shortened.

A convenient way of representing the various strain states is to use the Flinn diagram (Flinn, 1962). In this diagram **(Fig. 3.1a)**, the ratios of the principal strains are taken, such that

$$a = X/Y = (1+ e_x) / (1+ e_y) \text{ or } a = Sx / Sy$$

and

$$b = Y/Z = (1+ e_y)\ (1+ e_z) \quad \text{or} \quad b = Sy / Sz$$

and a is plotted against b (Park, 1983).

The different shapes of ellipsoids are distinguished using the value *K*, such that

$$K = (a - 1) / (b - 1).$$

Fig.3.1a is constructed assuming a constant volume since the line $K = 1$ will only pass through the origin when the volume change $\Delta = 0$. When $\Delta \neq 0$

$$1+ \Delta = (1+ e_x)\ (1+ e_z)$$

(since $(1+ e_y) = 1$ for $K = 1$ ellipsoids)

$$= a / b$$

$$\therefore a = b\ (1+ \Delta)$$

Thus for a volume change of Δ, the line $a = b\ (1+ \Delta)$ represents plane strain and divides the constrictional from the flattening fields **(Fig.3.1b)**.

The various strain states can be described as follows:

a) $K = \infty$ Axially symmetric extension

b) $1 < K < \infty$ Constrictional strain

c) $K = 1$ Plane strain

d) $0 < K < 1$ Flattening strain

e) $K = 0$ Axially symmetric flattening

In this way the shape of an ellipsoid can be described using only the value of parameter *K*, and constrictional and flattening strains can immediately be distinguished by whether *K* is greater than or less than 1.

The Nadai strain magnitude is defined by an orthogonal coordinate system using the natural principal strains E_X, E_Y and E_Z. The distance from the origin provides an invariant measure of the total strain magnitude (E_t), which can be decomposed into two orthogonal components: volume (E_v) and deviatoric (E_d) strain. E_v and E_d are independent of the rotational component of deformation.

$$E_t = (E_d^2 + E_v^2)^{1/2}$$

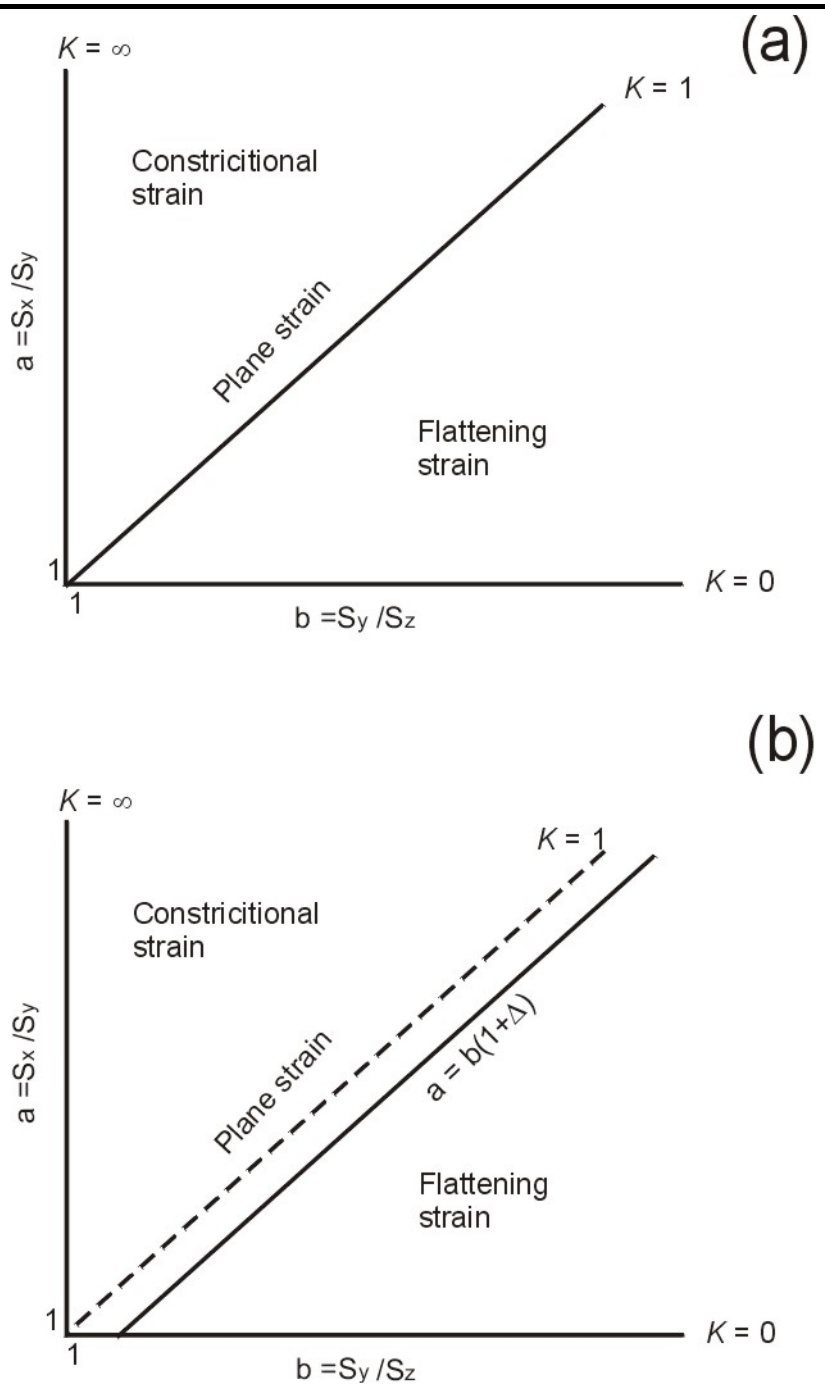

Fig.3.1 : Graphical representation of strain ellipsoids: the Flinn diagram. A) Different ellipsoids are described using the value K = (a-1) / (b-1). B) If the volume is not constant, the line a = b (1+Δ) divides the field of flattening strain. After Flinn 1962, and Ramsay, 1967.

3.2 Field investigations and sampling:

It has been introduced earlier that in total about forty-five days between 2001 to 2003 were spent in the field. Emphasis was given to collection of deformed rock samples, which were designated for strain analysis studies to be carried out subsequently in the laboratory.

167 samples were collected from the Gran Paradiso Massif (for sample localities refer to Fig. 3.2). The R_f/ϕ and Fry methods used on feldspar porphyroclasts from 143 augengneiss and 11 conglomerate samples of the Gran Paradiso unit (upper tectonic unit of the Gran Paradiso massif), as well as, 9 augengneiss (Erfaulet granite) and 3 quartzite conglomerate samples from the underlying Erfaulet unit (lower unit of the Gran Paradiso massif), and 1 sample from mica schist. The Fry method was applied to eight samples (one mica schist sample, four conglomerates and three augengneiss samples) for comparing the results with those obtained by the R_f/ϕ method. The feldspar grains from one mica schist sample have been analysed by the Fry method to see whether the strain recorded in the metasediments is of the same magnitude as those in the augengneiss and conglomerate.

Sample preparation for the R_f/ϕ and Fry analyses involved cutting large (20-30 cm) hand samples along three mutually perpendicular faces subparallel to the XY, YZ and XZ principal planes, mark feldspar grains an polished cuts and making scanned images from them. The tracings were then digitised. A least squares best-fit ellipse was calculated for each marker outline as well as its relative position and orientation.

A suite of 10 whole rock samples was crushed to obtain powders for undertaking chemical analysis. The powder material was used to prepare glass fusion discs as well as pressed powder pellets as would be described in detail later. The selection of the rock samples was based, essentially, on their varying degrees of deformation. Major- and trace element analyses were performed by using the standard XRF (X-ray fluorescence spectroscopy technique).

3.3 Techniques used in strain analysis:

To quantify the finite strain in the Gran Paradiso massif, feldspar grains and conglomerate closes have been analysed by the R_f/ϕ and Fry techniques (Fry 1979; Ramsay

1967; Ramsay & Huber 1983). Two-dimensional strain measurements were made on XY, XZ and YZ sections (X ≥Y≥ Z, finite strain axes) in order to estimate the three dimensional strain geometry. Finite strains determined with the normalized Fry technique were primarily used to check the R_f/ϕ estimates. The Fry strains are thought to represent the matrix strain, whereas the R_f/ϕ strains describe the fabric ellipsoid or clast strain (Ramsay & Huber 1983; Ring 1998). For R_f/ϕ analysis on feldspar, the long and short axes of up to 40 grains per section were measured and mean aspect ratios for each section were calculated. Tectonic strains were determined from the chi-squared minima of the R_f/ϕ analyses (Peach & Lisle 1979). For Fry analysis, the central points of more than 100 feldspar grains per section were used to calculate strain. The strain estimates were used to calculate the finite-strain ellipsoid according to the modified least-square technique of Owens (1984).

In order to calculate deformation-related volume change, major and trace element concentrations (in wt. % and ppm respectively) of both deformed and undeformed Gran Paradiso rock samples were measured employing the XRF technique. These have to be recognized otherwise misleading estimates of the principal stretches would be incurred.

Electron microprobe work was then undertaken to determine the analysed fabrics formed during high-P metamorphism. The association of high-Si phengite with the K-feldspar, phlogopite and quartz represents one of those recently recognized mineral assemblages that characterise high pressure, low temperature metamorphism in subduction zones (Massonne & Schreyer 1987).

3.3.1 Rf/ϕ Method:

In order that the strain analysis through the R_f/ϕ method would have meaningful results, it is imperative to demonstrate that the measured objects deformed homogeneously with their matrix. The R_f/ϕ technique is, in fact, based on calculating the theoretical distribution of final ellipticities and orientations that result from imposing different strains on objects that have a known initial ellipticity and orientation. The finial ellipticity R_f and the orientation ϕ of a deformed object depend on the initial ellipticity R_i, on the initial orientation θ of the undeformed object, and on the ellipticity R_s of the imposed strain ellipse. In order to evaluate the initial feldspar fabric, the strained distributions of the feldspar grains were undeformed using the procedure (program THETA) described by Peach and Lisle (1979). The method superimposes a coaxial strain having its long axis at right angles to the

preferred orientation on the R_f/ϕ distribution. The magnitude of this superimposed strain is incremented and after each step the randomness of the resultant undeformed orientation of the markers is calculated. If no initial fabric is present, the reciprocal finite strain value can be determined from the strain necessary to bring about the most uniform particle distribution.

At first the three principal strain directions X, Y, and Z have to be determined ($X \geq Y \geq Z$; principal stain axes). For this purpose, the rock sample is cut parallel to the foliation, which represents the plane of flattening (XY) and oriented perpendicular to Z. The next axes are the maximum extension direction X, which are normal to the foliation and parallel to lineation (XZ). The intermediate strain direction, Y, is defined by its orthogonality with X and Z, which are normal to foliation and lineation (YZ).

After having cut the samples in the Rxz and Ryz directions, Rxy direction has been calculated in accord with the following equation:

$$R_{xy} = R_{xz} / R_{yz}$$

In addition, the stretches Sx, Sy and Sz, which are parallel to the principle axes X, Y and Z respectively, enable the following calculation(s).

$$Sy = \sqrt[3]{\frac{R_{xz}}{R^2_{xy}}}$$

$$Sx = R_{xy} \times Sy$$

$$Sz = \frac{1}{Sx \times Sy}$$

3.3.2 Fry method:

The Fry method is useful for determining the strain ellipse from a large number of points. In essence, it involves plotting the length and orientation of a large number of center-to-center lines relative to a single reference point. Fry (1979) proposed the all object-object separations method, where the relative positions of adjacent grains are directly plotted by sequentially putting the origin of an overlay on each centre and recording the position of adjacent centres as points. In many aggregates, these points define an elliptical void and parallel ring of high point-density around the origin of the overlay. These ellipses will equal the finite-strain ellipse for homogeneously deformed populations of originally statistically uniform centres. The advantage of the Fry method is that it provides a graphical solution to

the centre-to-centre method, which is both rapid and accurate, and that one sees from the developing graph when enough data have been plotted to provide an answer of sufficient accuracy for the investigation in hand. This technique provides an excellent practical method for finding the best-fit solution to the strain ellipse.

3.3.3 X-ray fluorescence spectroscopy (XRF):

To investigate the possibility of deformation-related volume change, major oxide and trace element concentration were plotted on isocon diagrams (Grant 1986). These diagrams compare element concentrations in the altered rock (mylonite) to concentrations in the original rock (protolith). The basic argument is that some components are likely to have been immobile in the alteration process and, for example, should be relatively enriched in mylonite that underwent volume loss (O'Hara & Blackburn 1989). If these elements can be identified, volume change can be calculated assuming that the volume change is a factor common to the behaviour of all components. Al_2O_3 (Hem 1978), TiO_2 and Zr (Correns 1978) are usually immobile during regional deformation. The experimental results of Ayers and Watson (1991, 1993) indicate that rutile and zircon solubilities and solubility gradients in high-grade PT fields will be extremely low for typical water-rich fluid compositions. If significant mobility of Ti and Zr took place during metamorphism, then it is likely that rutile and zircon would have grown in veins, which has never been observed in and next to the sample localities. However, rutile commonly occurs in quartz veins in high-pressure settings suggesting that Ti might be a mobile phase during high-pressure metamorphism.

Major- and trace element analyses were performed by standard X-ray fluorescence spectroscopy (XRF), using glass fusion disks and pressed powder pellets. All analyses were made with a sequential Philips PW 1404 wavelength-depressive fluorescence spectroscopy with excitation by an Rh X-ray tube following a method described by Stern (1972). Operating conditions were between 40 and 80 kV and 30 to 60 mA, depending on which element was analysed.

3.3.4 Microprobe analysis:

Microprobe techniques differ from most other techniques used to analyse geological materials in that they involve the excitation and chemical analysis of selected areas as small as a few microns in diameter on the surface of samples. Specimens must therefore be

prepared as polished geological thin sections mounted on a glass slide backing, or alternative as samples polished in a resin block. Microprobe techniques have the ability to determine the composition of individual minerals in thin section or even concentration variations within a single grain.

The most widely used of these techniques is electron probe microanalysis. An electron beam, accelerated to a selected voltage, normally in the range 15 to 30 kV, is focused on the surface of a sample. Interactions between this primary electron beam and the sample cause a number of phenomena, including the generation of x-rays characteristic of the atoms of the excited sample. The intensity of these x-rays is measured using wavelength dispersive or energy dispersive spectrometers. After correction for matrix effects, count data are compared with data from minerals of standard composition in order to quantify the analysis. Due to the unavoidably higher intensity of the continuum formed by electron excitation, detection limits are of the order of 50 to 100 times poorer than those expected for bulk analysis by x-ray fluorescence.

Quantitive mineral analyses, backscatter electron images and X-ray element maps were performed on a JEOL JXA 8900 RL superprobe at the Institute for Geosciences at the University of Mainz. Natural and synthetic phases were used calibration. Additionally a CL and F content in mica were measured using the GlimUMainz procedure with 15 kV acceleration voltages, 12 nA beam current an beam diameter of 2μm. Obtained data were corrected for absorption, atomic number, fluorescence and background using the Phi-Rho-Z method.

3. 4 Results of finite-strain analysis:

The sample localities for finite strain analysis are shown in **Fig.3.2**, the strain data are summarized in **Tables 3.1 and 3.2** (see appendix).

3.4.1 Deformation structures:

Meso- and microstructural investigations were made on polished slabs and thin section cut parallel to the foliation (XY), normal to the foliation and parallel to the lineation (XZ) and normal to the foliation and lineation (YZ).

The augengneiss of the Gran Paradiso unit is very heterogeneously deformed in the field **(Fig. 3.3)**. Localities where feldspar grains in platy augengneiss are extremely smeared

out with aspect ratios in the XZ section exceeding 25 grade laterally and vertically into moderately deformed augengneiss with XZ aspect rations of 3-4 over short distances of ~100 metres **(Fig.3.3a)**. The development of an augengneiss fabric appears to be controlled by moderate deformation of a formerly porphyritic granite, whereas intense deformation destroyed any former porphyritic or augen fabric **(Fig.3.3b and c)**. However, the platy augengneiss does not characterize the nappe contact of the Gran Paradiso unit with the overlying Zermatt-Saas zone. This nappe contact is studied in detail near Cogne and Lillaz **(Fig. 2.5)**. Augengneiss there typically has feldspar porphyroclasts with aspect ratios of 2-6 in XZ sections. Close to the contact of the Gran Paradiso unit with the Zermatt-Saas zone in the northeast near Ronco nicely preserved intrusive relationships of the granite precursor of the augengneiss into metapelite are abundant (see also Callegari et al. 1969). In the structurally lower parts of the augengneiss unit east of Ceresole in the central massif, the rocks appear almost undeformed in the field **(Fig. 3.3d)**. At the contact of the augengneiss unit with conglomerate of the Money complex south of Cogne and the Erfaulet granite south of Lillaz, the augengneiss also does not appear strongly deformed in the field.

In the augengneiss, the main-phase foliation is a gneissic layering defined by elongated, dynamically recrystallized feldspar porphyroclasts, myrmekite growth and alignment of mica and quartz **(Fig.3.3e and f)**. In the metasedimentary rocks of the Gran Paradiso unit, the morphology of the foliation varies from a differentiated layering, with relics of crenulations in quartz-rich microlithons, to a pervasive schistosity. Vissers & Compagnoni (1984), Vearncombe (1985) and Borghi et al. (1994) showed that the main-phase foliation is superimposed on an earlier Alpine foliation.

On the main-phase foliation, a west- to WNW-trending stretching lineation is developed **(Fig.3.4)**. In augengneiss, this stretching lineation is well expressed by the alignment of recrystallized tails around feldspar porphyroclasts and preferred orientation of quartz and mica aggregates. In metasedimentary rocks, strain shadows around garnet and quartz–mica alignment define the stretching lineation. Asymmetric strain shadows around garnet and shear bands indicate top-to-the-west or –WNW shear **(Fig. 3f)**. Strain shadows around feldspar porphyroclasts contain recrystallized potassium feldspar, plagioclase and quartz. Assumed temperatures for the onset of ductility of potassium feldspar are usually of the order of .450–500 8C (Voll 1980; Pryer 1993).

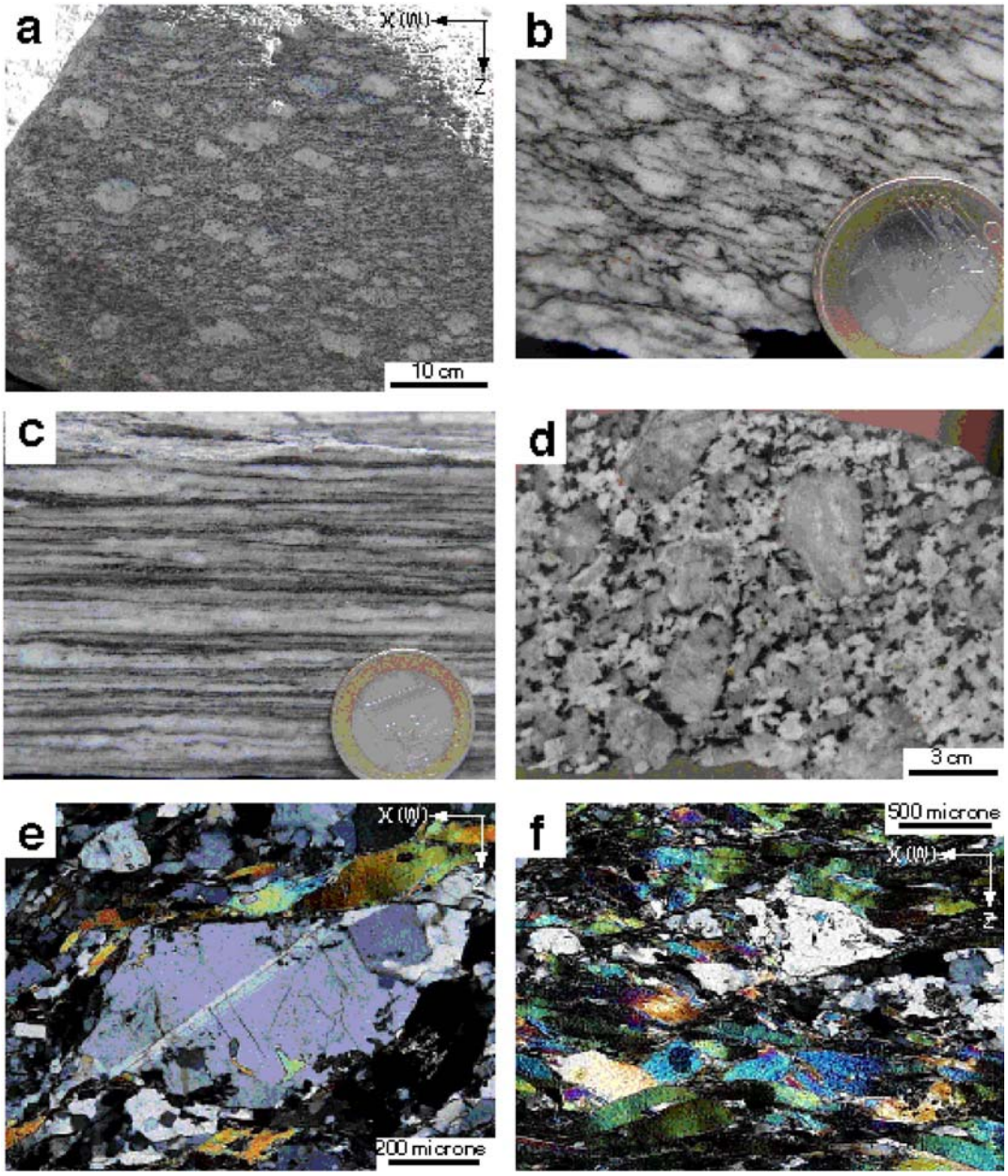

Fig.3.3: (a) XZ section of moderately deformed augengneiss SSE of Pont; note that feldspar porphyroclasts with axial ratios of up to ~4 are not parallel to main-phase foliation. (b) Quartzite conglomerate from base of Zermatt-Sass zone E of Lillaz; most clasts are parallel to foliation. (c) Mylonitic deformation of augengneiss leading to platy gneiss; sample GP02-106. (d) Weakly deformed metagranite E of Ceresole; large feldspar clasts are at high angle to foliation. (e) Dynamically recrystallized feldspar porphyroclasts indicating top-W shear sense; both microphotographs are from sample GP02-80A. (f). Recrystallized feldspar porphyroclasts and mica fish indicating top-W shear sense; sample GP02-102.

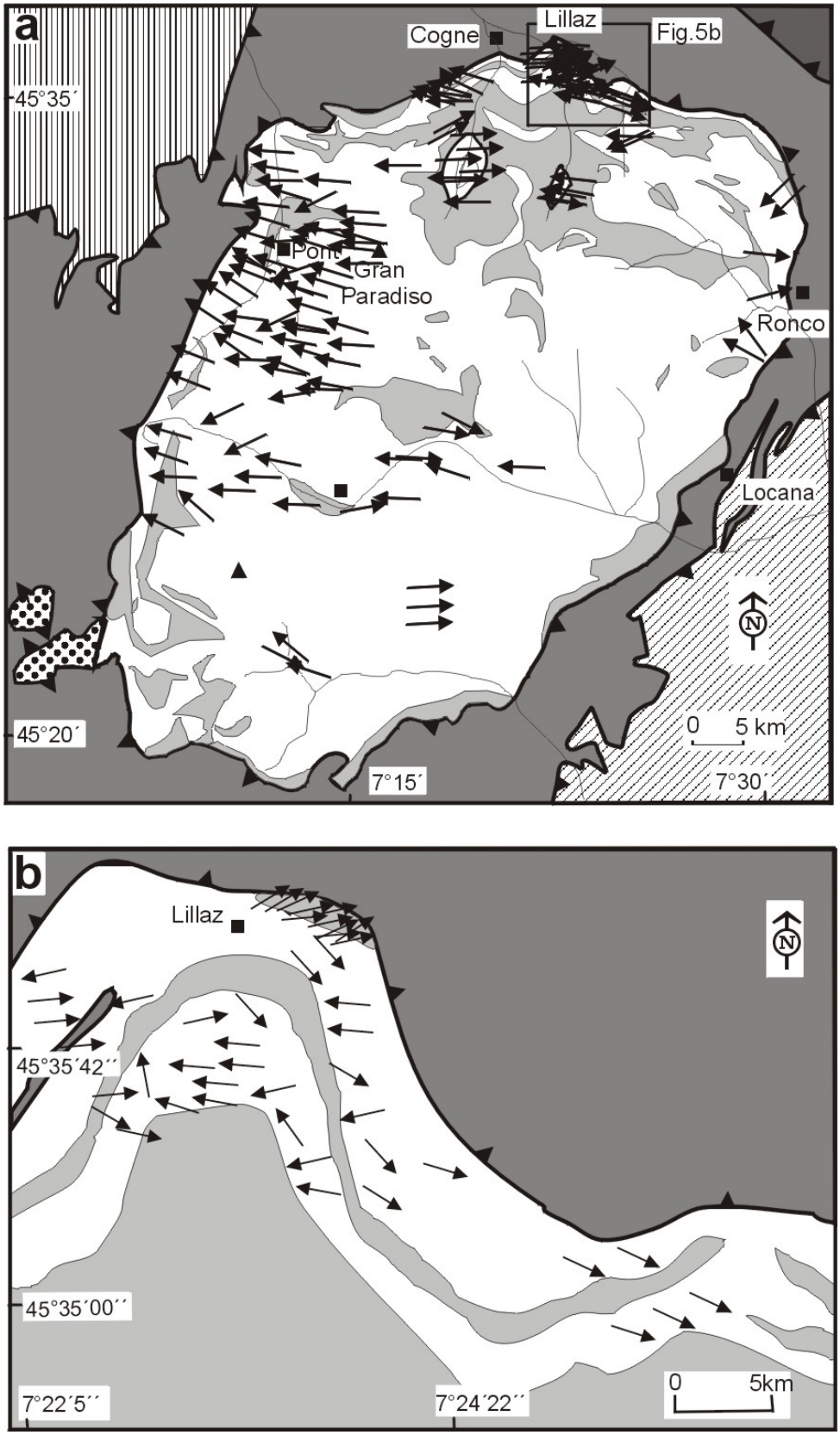

Fig.3.4: (a) Lineation map for Gran Paradiso massif and contact between Gran Paradiso massif and Zermatt-Saas zone near Lillaz (b); arrow heads indicate plunging direction.

The main-phase foliation and stretching lineation is deformed by two subsequent deformation events, which proceeded during greenschist- to sub-greenschist-facies metamorphism (Vissers & Compagnoni 1984; Vearncombe 1985; Sandrone et al. 1993). The latest of these deformation events is associated with localized top-E/ESE shearing. It is important to note that potassium feldspar did not deform ductilely during these two post-peak-metamorphism deformation events.

3.4.2 Results of Microprobe analysis:

As discussed previously, phengite chemistry has been investigated in detail in order to determine the analysed fabrics formed during high-P metamorphism, metamorphic pressure conditions on the basis of an experimentally developed phengites geobarometer, check differences between samples and delineation of zonation within grains. It is to be noted that the analysed samples are dispersed within the phengite field with a clear tendency to merge with that of muscovite (see triangular diagram – **Fig. 3.5**).

Within the framework of the current investigation, microprobe analytical data of phengite micas are presented in **Table 3.3** (see appendix) and plotted in **Fig. 3.6**. The phengitic micas from augengneiss samples Gp01.65B, Gp02-80A and Gp02-102 have mean average Si contents of ~ 3.5 p.f.u. These values are strikingly high and the phenomenon may be interpreted as an indication of high-pressure conditions.

As can be seen in Figure 3.6a the aluminium content of the phengites consistently increases with the decrease of Si content (i.e. they display a negative correlation trend). In contradiction, the composition of the individual populations in the samples analysed (i.e. of iron, magnesium and sodium contents) show comparable distribution patterns. The magnesium content is, more or less, constant with the silica variation **(Fig.3.6b&c)**. Furthermore, the histogram of white mica analysis shows a strongly unimodal distribution with the peak about 3.5 Si p.f.u. **(Fig.3.6d)**.

Detailed microprobe analytical studies indicate homogeneity and that Si values are constant across individual phengites grains (i.e. no chemical zonation). These features are equally decipherable through microscopic investigations. It is inferred that the phengites micas concerned belong to one generation.

The analytical work and corroborative microscopic investigations that were carried out by the author (**Table 3.4 see appendix**) have revealed that plagioclase has an albitic

composition. In addition, no zonation has been detected in the analysed feldspars. Lack of oligoclase rims in the plagioclase component of the rocks studied suggests that the fabrics are inferred to have formed at high-pressure conditions.

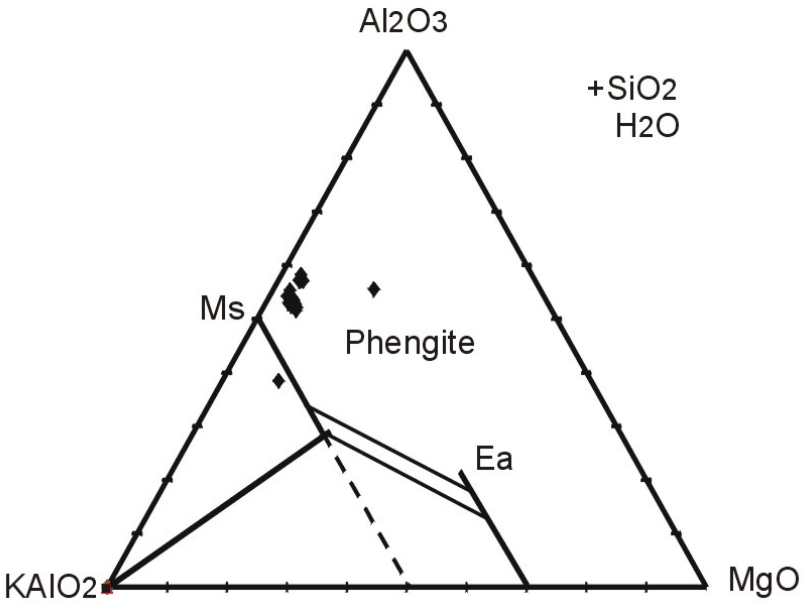

Fig.3.5: Modified AKF diagram showing fundamental phase relations in the system K2O-MgO-Al2O3-SiO2-H2O relevant to Phengite solid solubility. Abbreviations: Ea eastonite, Ms Muscovite, (after Massonne and Schreyer 1987).

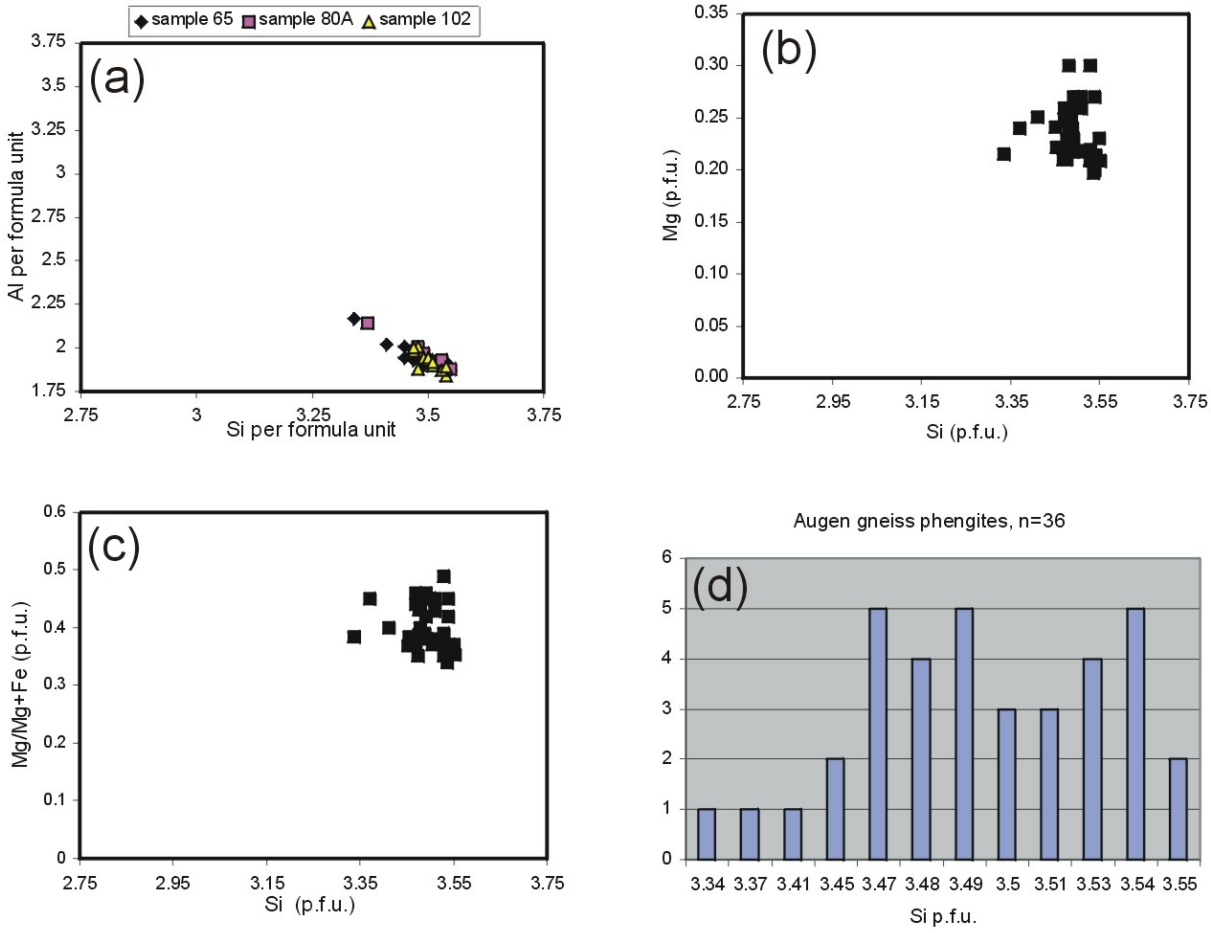

Fig.3.6: Phengite chemistry: a) compositional variation of Si and Al. b) Relationship between Mg and Si contents. c) Relationship between Mg/Mg+Fe and Si contents. d) Histogram of white mica analyses showing uni-modal distribution of Si contents.

3.4.3 Direction of Finite Strain:

The field orientations of strain for Gran Paradiso unit (augengneiss, conglomerate) and Erfaulet unit (conglomerate, Erfaulet granite) are shown in **Figs. 3.7 to 3.9.**

3.4.3.1 Maximum Extension Direction (X)

The trends of the long axes of the finite strain ellipsoid (X) in conglomerate and augengneiss are along E/ENE and W/WNW directions and are of shallow plunges **(Fig.3.7a and Fig.3.7b)**. In addition, the trend of the Erfaulet unit is, predominantly, along a W/WNW direction (similar to augengneiss direction) and its plunge is a shallow as well (**Fig.3.7c)**. In particular, the mean value for the long axes for all units shows clustering along a W/WNW trend and a plunge of about 8° (see **Fig.3.7d** and Table1).

3.4.3.2 Intermediate Direction (Y)

The samples in conglomerate and augengneiss in the intermediate direction (Y) have an overall maxima fanning around the N direction and a shallow plunge in the main part **(Fig.3.8a and Fig. 3.8b)**. On the other hand, the Erfaulet unit displays a W/WSW direction and a shallow angle of plunge **(Fig.3.8c)**. The mean for all units has a N/ENE trend, a dipping plunge about 3°, in addition to a subvertical attitude with respect to the X direction **(Fig.3.8d)**.

3.4.3.3 Maximum Shortening Direction (Z)

In **Fig.3.9a**, conglomerate has a W/WSW trend and the augengneiss is of a southeasterly trending maximum shortening direction **(Fig.3.9b).** These rocks have a steeply plunging angle. Furthermore, the trend of the Erfaulet unit is at an E/ENE direction and a high angle as well **(Fig.3.9c)**. Contouring of all data for the shortening directions (Z axes) reveals a preferred orientation of about 118° (ca. SE) and a steep angle in the range of 82° **(Fig.3.9d)**. Thus, shortening axes are subvertical and are associated with a subhorizontal foliation.

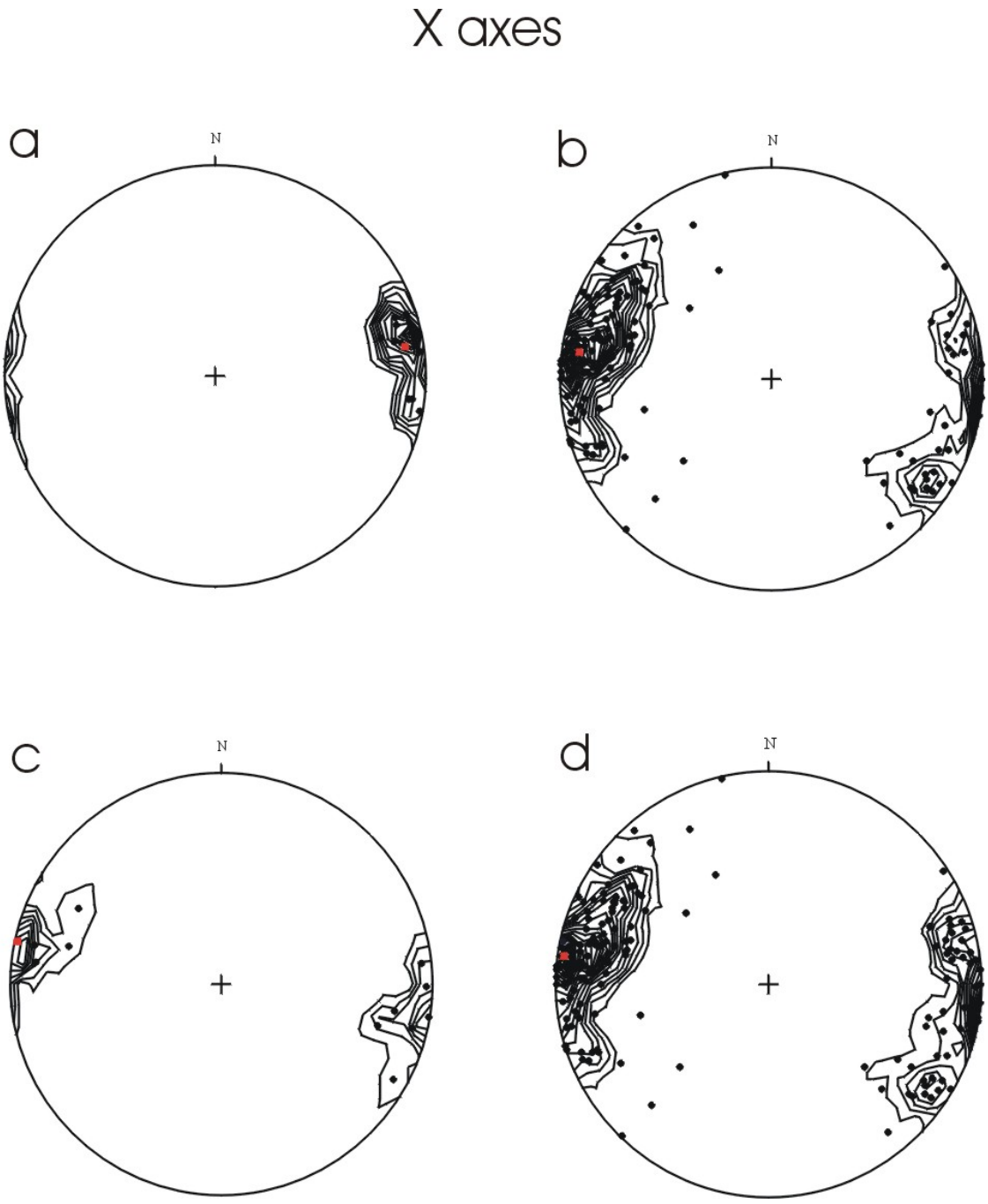

Fig.3.7: Lower-hemisphere equal-area projections for maximum extension direction (X): a) conglomerate samples (contours start at 5% and increment every 5%), b) augengneiss samples (contours start at 1% and increment every 1%), c) Erfaulet samples (contours start at 5% and increment every 5%), and d) all samples (contours start at 1% and increment every 1%). Red squares in the stereographic projections represent mean values of tensor averages.

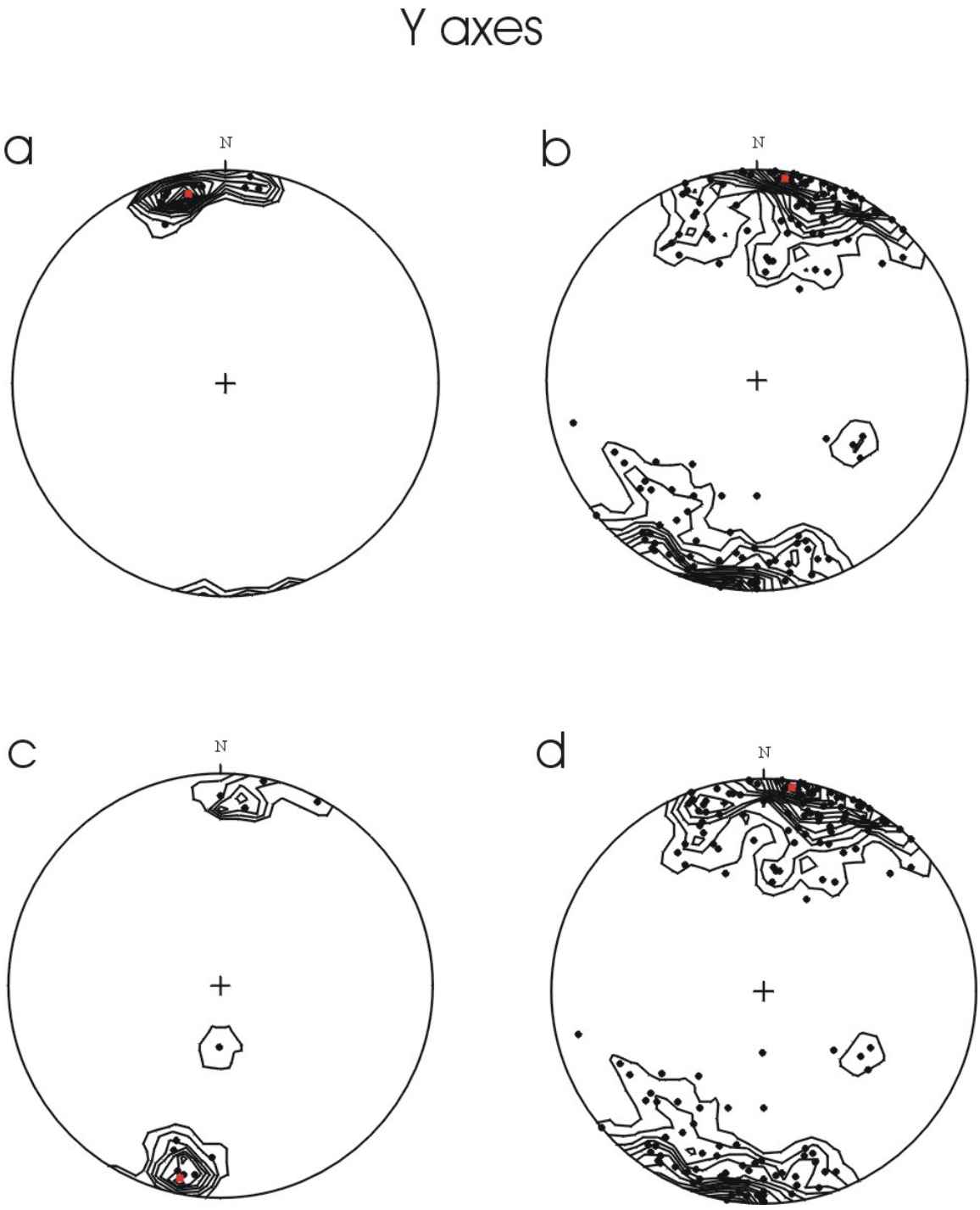

Fig.3.8: Lower-hemisphere equal-area projections for intermediate direction (Y): a) conglomerate samples (contours start at 5% and increment every 5%), b) augengneiss samples (contours start at 1% and increment every 1%), c) Erfaulet samples (contours start at 5% and increment every 5%), and d) all samples (contours start at 1% and increment every 1%). Red squares in the stereographic projections represent mean values of tensor averages.

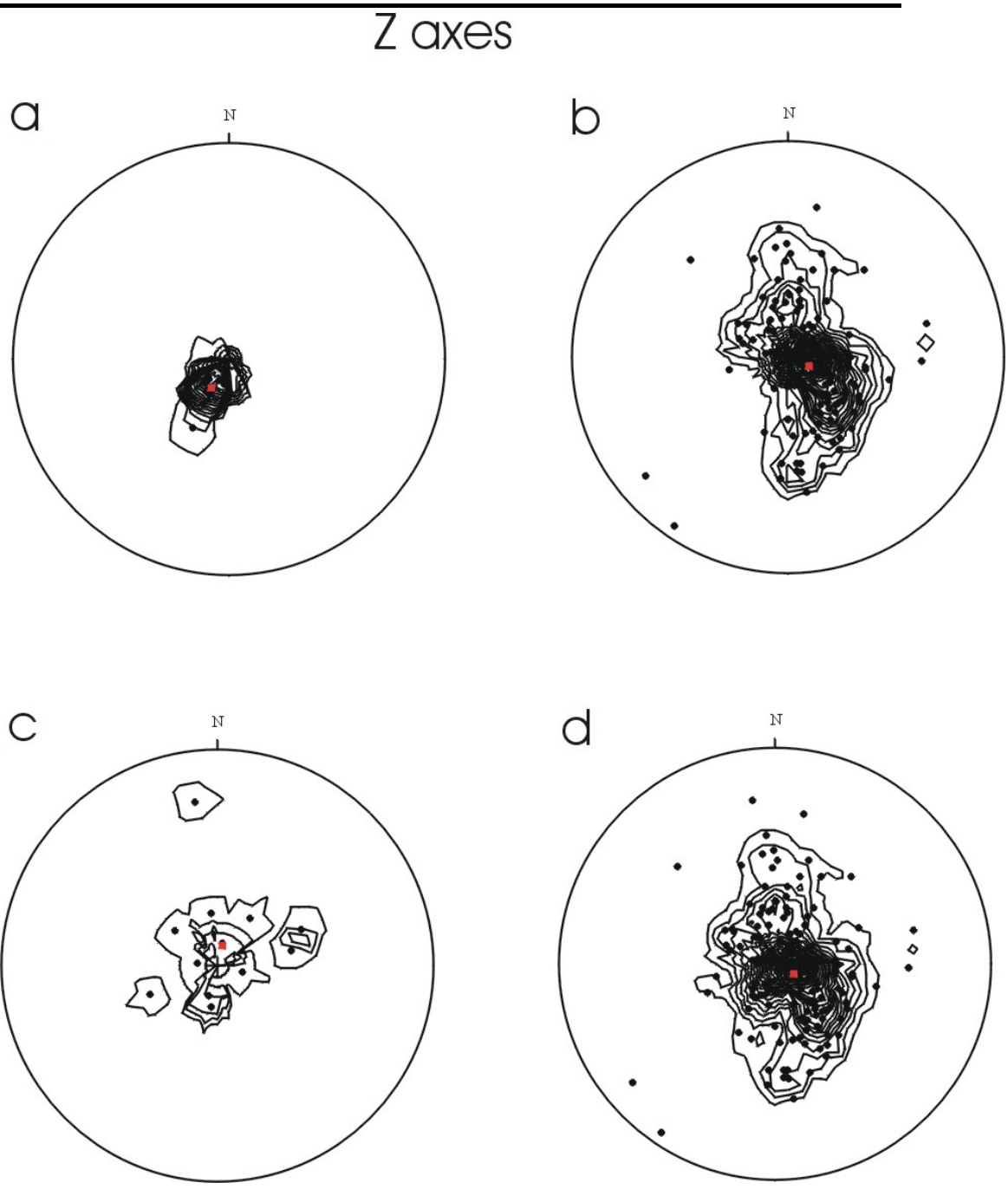

Fig.3.9: Lower-hemisphere equal-area projections for maximum shortening direction (Z): a) conglomerate samples (contours start at 5% and increment every 5%), b) augengneiss samples (contours start at 1% and increment every 1%), c) Erfaulet samples (contours start at 5% and increment every 5%), and d) all samples (contours start at 1% and increment every 1%). Red squares in the stereographic projections represent mean values of tensor averages.

3.4.4 Magnitudes of Finite Stretches:

The sample localities for finite strain analysis are shown in **Fig. 3.2** (see appendix), the strain data are summarized in **Tables 3.1 & 3.2** and shown in a Flinn diagram in **Fig. 3.10a**. The Flinn diagram shows the relative shapes of the strain ellipsoids, i.e. prolate vs oblate. According to Hossack (1968), this classification is called strain symmetry. To infer strain type, i.e. constrictional vs flattening, information on volume strain is needed.

As shown in **Figure 3.10b**, Fry strains are not fundamentally different from R_f/ϕ strains; in some cases, the R_f/ϕ strains are slightly greater than the Fry strains, whereas in other cases the opposite is the case. Therefore, our studied samples show that there was no significant difference in deformation behaviour between the quartz-mica matrix and the feldspar porphyroclasts during the accumulation of finite strain at peak metamorphic conditions. Furthermore, finite strain in the augengneiss is of the same order of magnitude as those from the conglomerate and metasediments samples. The main-phase foliation is not refracted between augengneiss and metasediments, which also suggests similar deformation behaviour in both lithologies. Hence, R_f/ϕ strains derived from analysing feldspar porphyroclasts and quartzite pebbles represent regional strain.

In general, the strain ellipsoids have oblate strain symmetry with some data points in the prolate field **(Fig. 3.10a**). The axial ratios in XZ sections range from 2.10 to 69.81 **(Table 3.2)** with S_X ranging from 1.34 to 9.62 **(Table 3.1)**. The stretches in the Z direction, S_Z, range from 0.12 to 0.64, indicating vertical shortening of 36% to 88%. S_Y ranges from 0.57 to 1.65, showing both contraction and extension in this direction. The strain data verify pronounced heterogeneous deformation of the augengneiss as apparent in the field.

The amount of strain as defined by the Nadai strain magnitude **(Table 3.2)** has been plotted for all samples on three maps **(Fig. 3.11)** and the strain magnitudes of the samples from the northwestern massif have been projected into a cross section **(Fig. 3.12)**. The map pattern is somewhat erratic and does not show any obvious relationships between the strain magnitude and tectonic contacts in the Gran Paradiso massif. The highest strain magnitudes of about ~3 occur in a small area to the southwest of Gran Paradiso summit south of Pont in the middle part of the Gran Paradiso unit **(Fig. 3.11c)**. Towards the contact with the Zermatt-Saas zone in the western and northern Gran Paradiso massif the values decrease to ~1.5. Our detailed study in the Lillaz area of the northern Gran Paradiso massif also does not show any

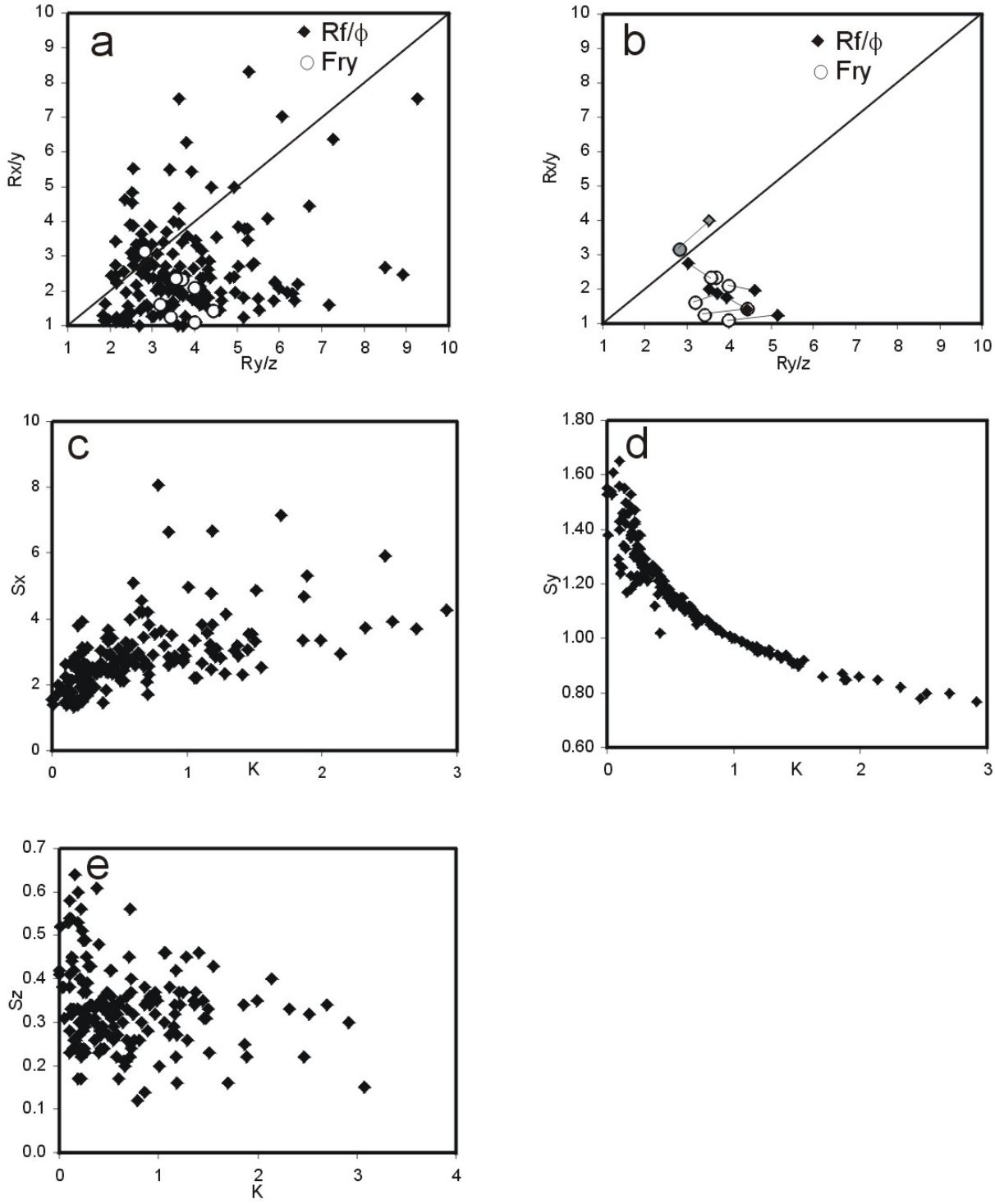

Fig. 3.10: (a) Flinn diagram (Flinn 1962) showing relative strain or strain symmetry as obtained by R_f/ϕ (black squares) and Fry (open dots) analysis. (b) R_f/ϕ and Fry data from same samples connected by tie lines; grey sample points indicate data from metasediments. (c) S_X vs K showing positive correlation. (d) S_Y vs K showing pronounced negative correlation. (e) S_Z vs K depicting no obvious correlation.

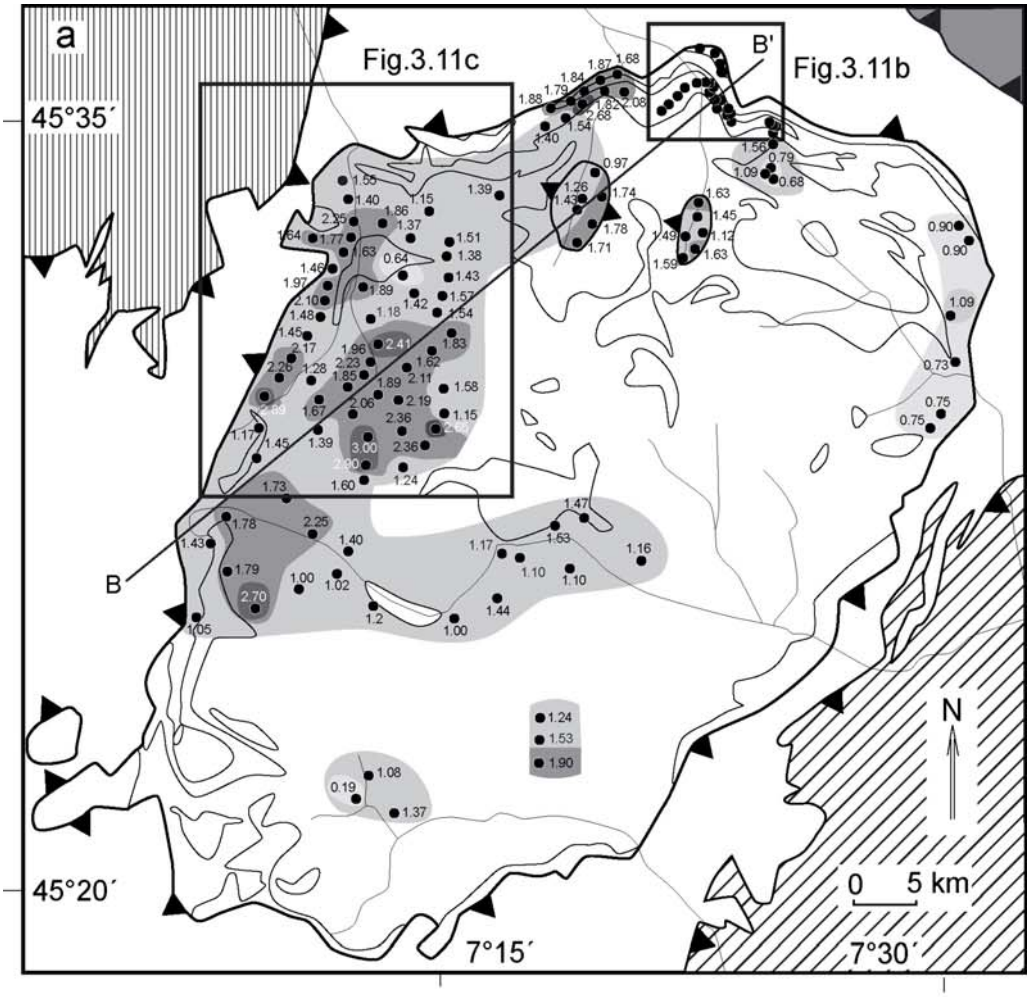
a
Fig.3.11c
Fig.3.11b
B
B'
45°35´
45°20´
7°15´
7°30´
N
0 5 km

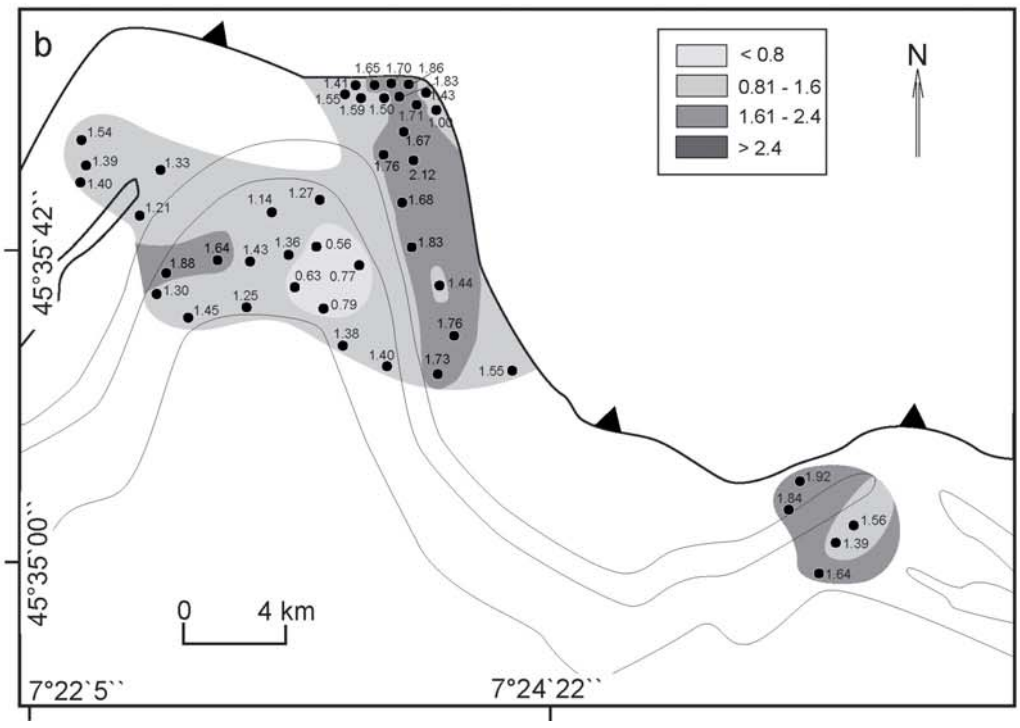
b
< 0.8
0.81 - 1.6
1.61 - 2.4
> 2.4
N
45°35`42``
45°35`00``
7°22`5``
7°24`22``
0 4 km

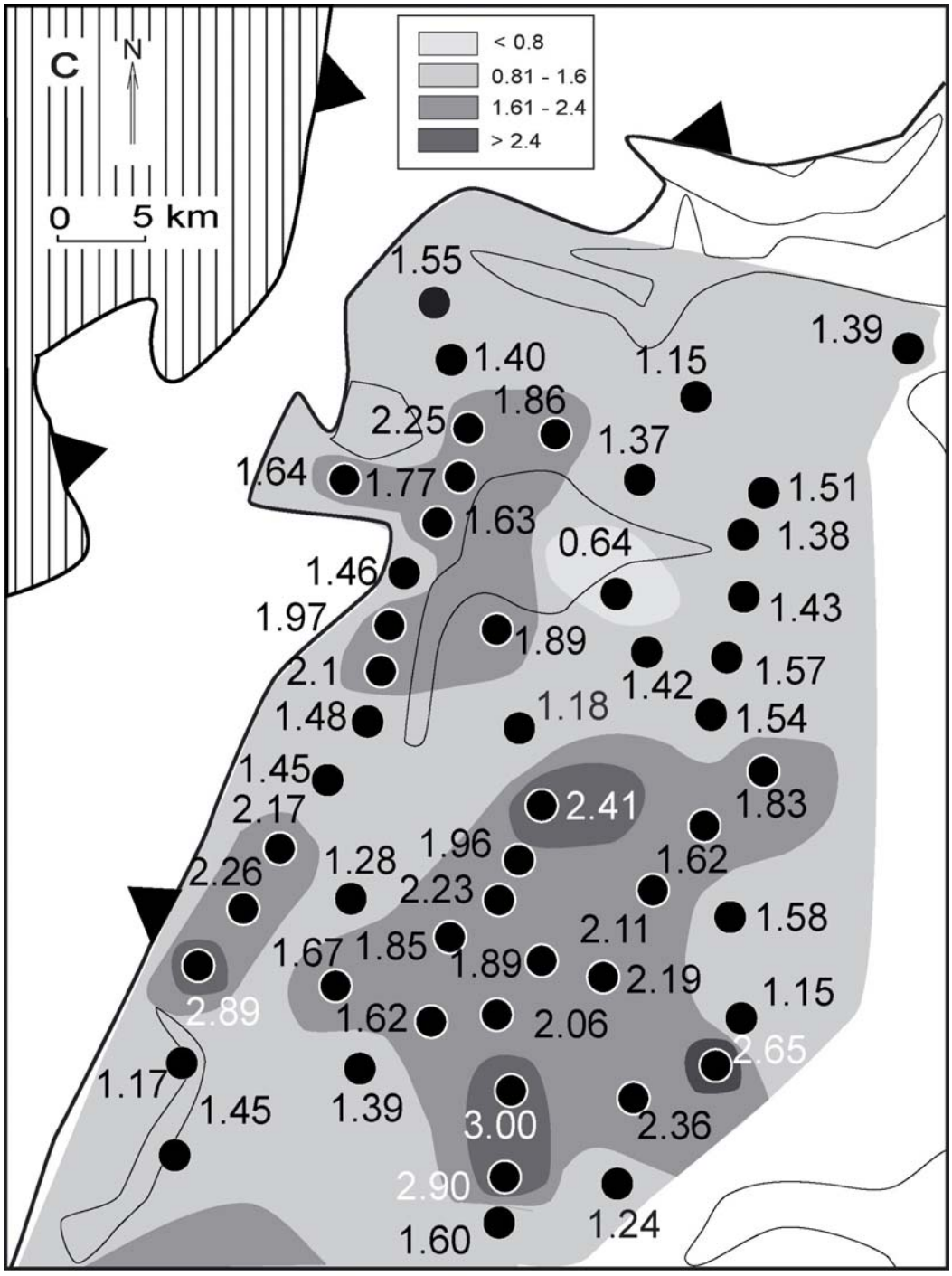

Fig.3.11: (a) Maps showing Nadai strain magnitude (E_t) for each sample and contours of E_t for Gran Paradiso massif (a), contact of latter with Zermatt-Sass zone (b) and contact with the western part for Gran Paradiso (c). Assuming constant volume deformation Nadai strain magnitude represents square of deviatoric strain ($E_t = E_d^2$). Cross section B-B' in Fig. 12 is indicated.

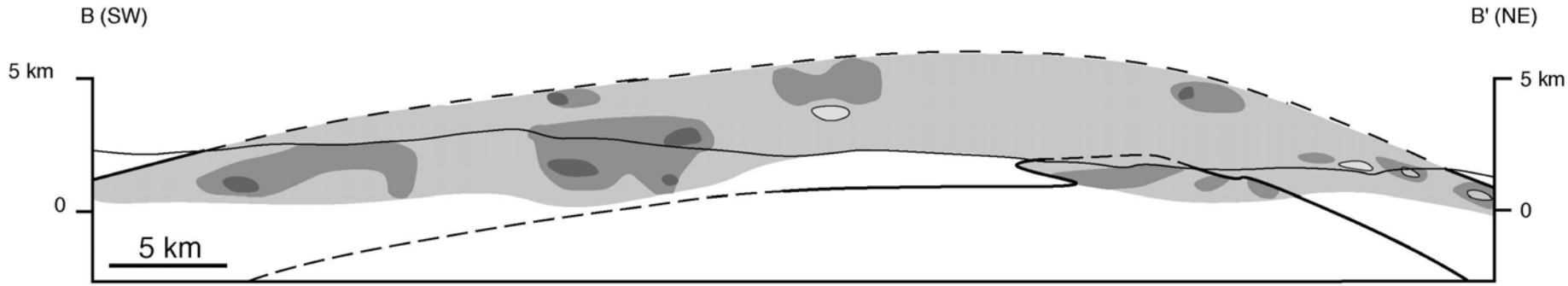

Fig.3.12: Cross section B-B´ showing contoured Nadai strain magnitude and its relation to nappe contact within Gran Paradiso massif and between latter and Zermatt-Saas zone; highest Nadai strains occur within Gran Paradiso unit.

obvious strain increase towards the contact of the Gran Paradiso unit with the Zermatt-Saas zone **(Fig. 3.11b)**. The contact of the Gran Paradiso unit with the Zermatt-Saas zone in the northeast near Ronco is even characterized by strain magnitudes >1. The nicely preserved intrusive relationships in this area (see above) corroborate low strain intensities. The tectonic contact between the Gran Paradiso and Erfault units is also not characterized by increased strain magnitudes **(Fig. 3.11a)**; values of 1-1.5 are typical for the Erfault unit **(Table 3.2)**.

In contrast to the strain magnitude, the strain symmetry as expressed by the K value (Flinn 1962; Ramsay & Huber 1983) does show a relationship to nappe contacts in the Gran Paradiso massif **(Figs. 3.13 & 14).** With a few exceptions, K values in the Gran Paradiso unit are low and indicate oblate strain. Near Lillaz, the contact between the Gran Paradiso unit and the Zermatt-Saas zone is characterized by strong oblate strain symmetries **(Fig. 3.13b)**. However, in the Erfaulet unit, the K values are, in general, greater than 1 and suggest slightly prolate strain symmetry at the contact between the Gran Paradiso and Erfaulet units **(Fig. 3.13a)**.

Figure 3.10c and 3.10d show that with increasing stretch in the X direction and decreasing S_Y the strain symmetry becomes more prolate. S_Z shows no obvious correlation between vertical shortening and K **(Fig. 3.10e)**. Because deviatoric strain depends on all three principal stretches, the positive and negative correlation of S_X and S_Y with the K value does not result in a correlation of E_t and K on the maps.

3.4.5 Volume Change (Volume deformation):

In the isocon diagrams in **Figure 3.15** the chemical compositions **(Table 3.5 see appendix)** of variously deformed samples have been plotted against the concentration of the least-deformed sample (GP01-23A). It is notes that sample GP01-23A does not represent a protolith of the deformed samples because it is deformed and metamorphosed. However, we intent to investigate in a semi-quantitative fashion whether pronounced deformation in the more highly deformed samples was accompanied by significant volume change. We argue that the isocon diagrams in **Figure 3.15** illustrate the depletion or augmentation of the analysed elements during progressive deformation.

It is evident that no single isocon can be fitted to the data points in most diagrams, which suggests differential element behaviour. Nonetheless, Al_2O_3, Zr and also Ti plot on

reasonably defined isocons in most diagrams. In some diagrams, Al_2O_3 and Zr (and Ti) show slight enrichment, whereas in others it does not. There is no systematic increase in the amount of volume loss or gain with increasing deformation intensity. Overall, the data suggest constant-volume or isochoric deformation.

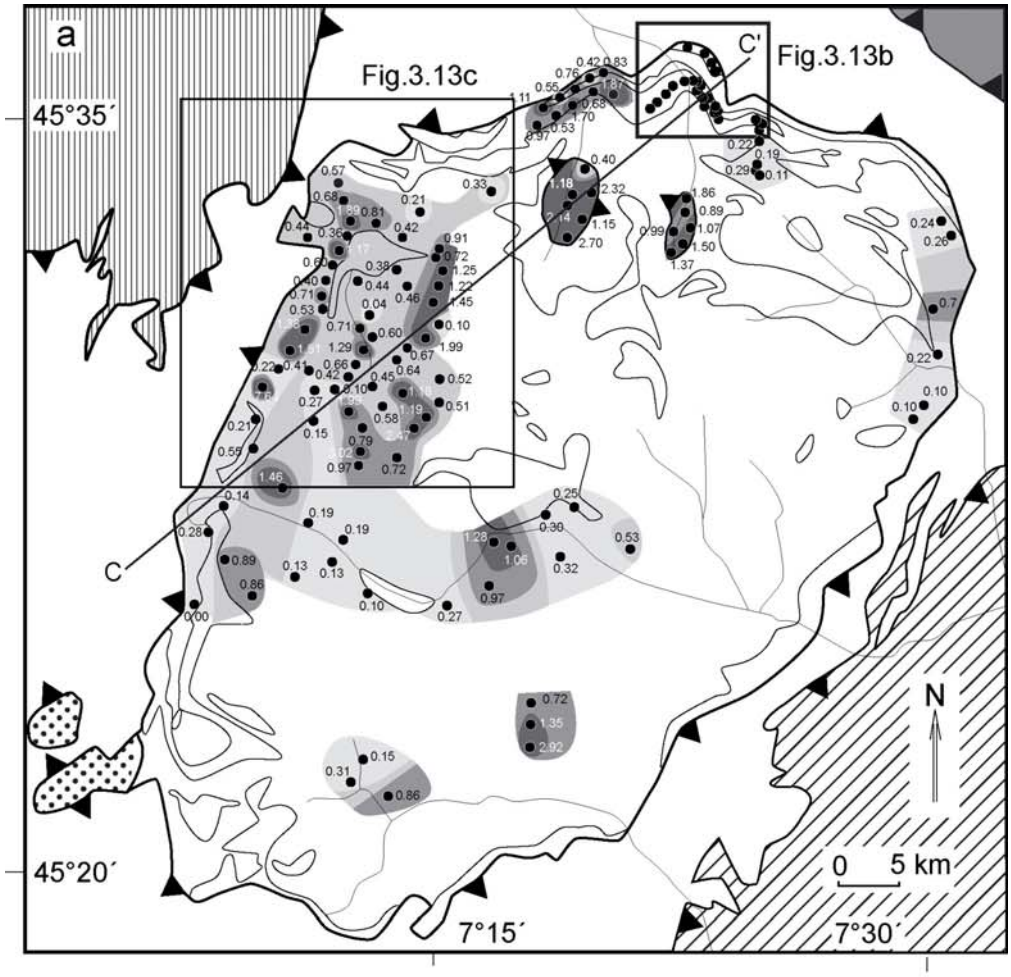
a
Fig.3.13c
Fig.3.13b
C
C'
45°35´
45°20´
7°15´
7°30´
N
0 5 km

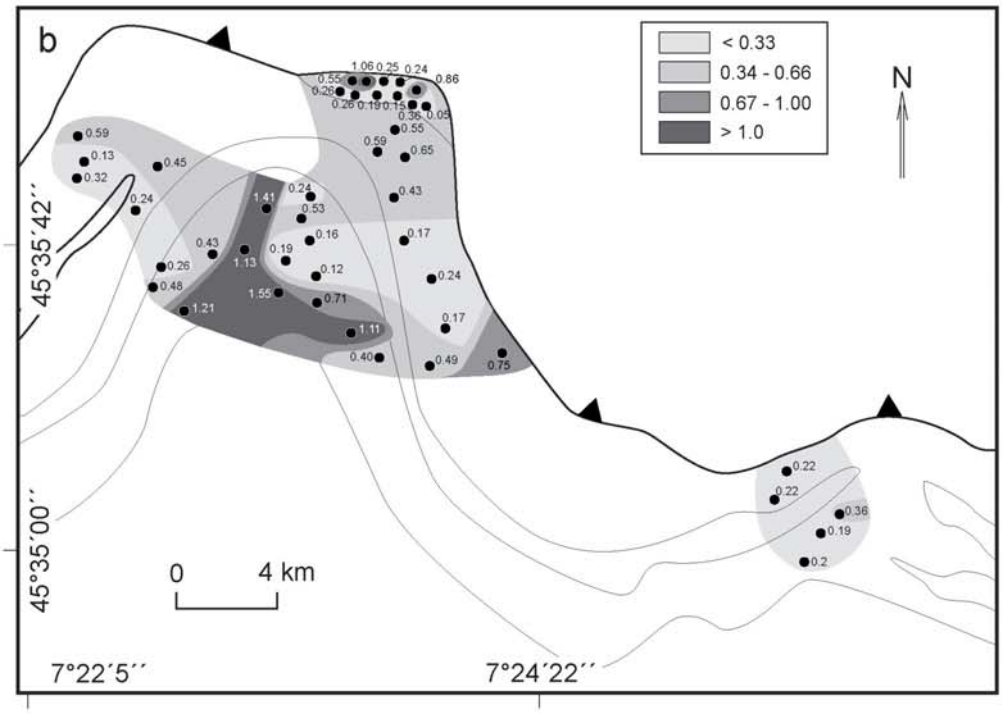
b
< 0.33
0.34 - 0.66
0.67 - 1.00
> 1.0
N
45°35´42´´
45°35´00´´
7°22´5´´
7°24´22´´
0 4 km

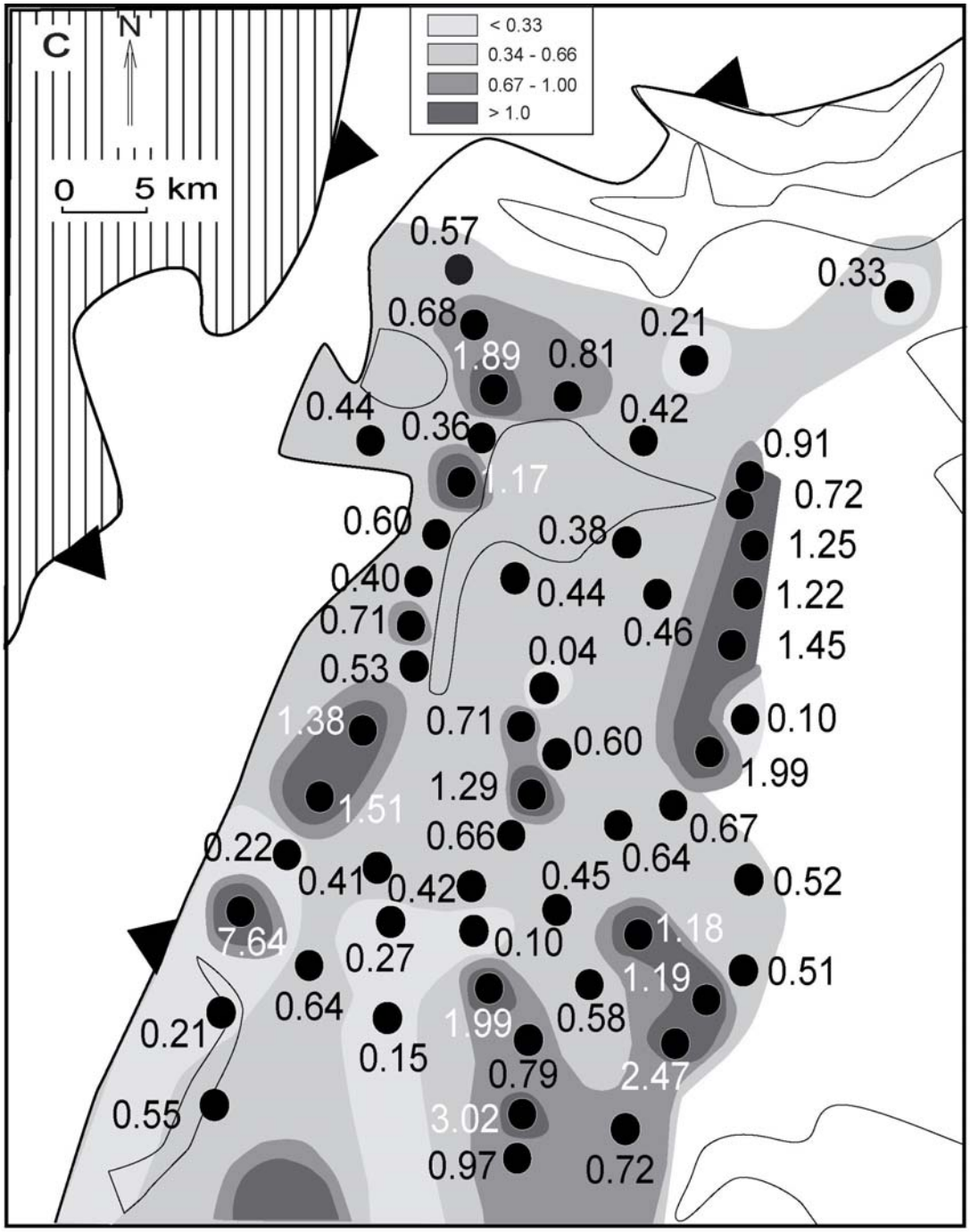

Fig.3.13: (a) Maps showing K value for each sample and contours of K value for Gran Paradiso massif (a) and contact of latter with Zermatt-Sass zone (b), and contact with the western part for Gran Paradiso (c). Cross section C-C' in Fig. 14 is indicated.

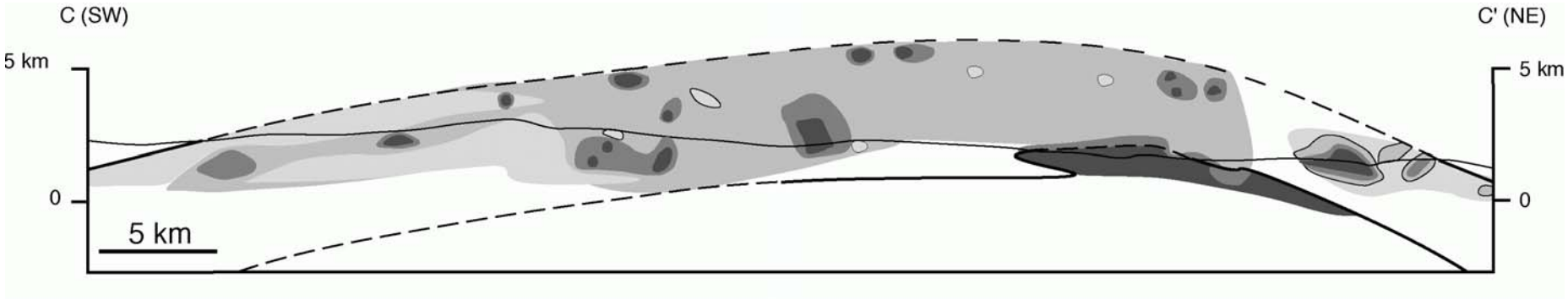

Fig.3.14: Cross section C-C´ showing contoured K value and its relation to nappe contact within Gran Paradiso massif and between latter and Zermatt-Saas zone; K values >1 are in general restricted to Erfaulet unit.

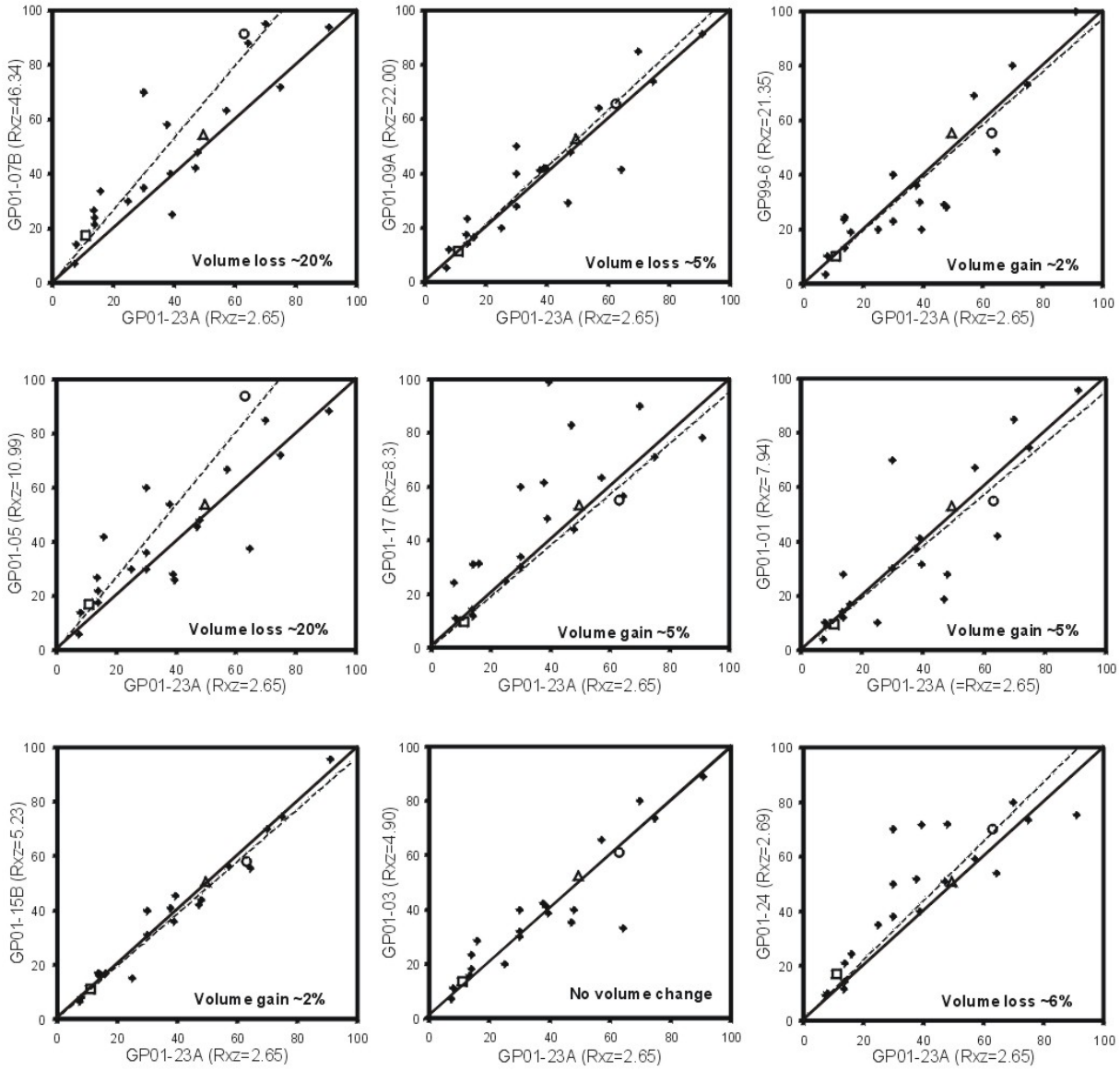

Fig.3.15: Isocon diagrams after Grant (1986) comparing trace element and major oxide concentrations of deformed samples to that of least deformed sample (GP01-23A) (R_{XZ} ratios of samples are shown); element concentration is scaled to 0-100 wt% or parts per million. Solid line represents 1:1 correspondence between concentrations of deformed and almost undeformed samples; dashed line represents averaged estimate of volume loss based on enrichment of Zr (open circles), Al_2O_3 (open triangles) and TiO_2 (open squares).

4. Ductile Strain and Exhumation history for the Metamorphic Rocks of the Gran Paradiso Massif

4.1 Introduction:

The current chapter is an attempt to explain how the missing ca. 3.5-10.5 km thick crustal section between the Erfaulet and Gran Paradiso units has been removed. This demands exhumation of the overriding Gran Paradiso unit during high-pressure metamorphism. One possibility to explain this paradox is the vertical shortening of 36-88%, which accompanied the accumulation of finite strain. Ring et al. (2001b) showed that nappe emplacement will, in general, result in higher PT conditions in rocks of the lower plate, which is in contrast to the commonly applied 'rules' of thrust faulting according to which rocks with higher metamorphic grade should be tectonically above lower grade rocks. Nevertheless, as argued by Ring et al. (2001b), the occurrence of high-grade on low-grade rocks requires that crustal shortening and nappe stacking is associated with a reduction of the overburden (exhumation) of the overriding nappe **(Fig. 4.1)**.

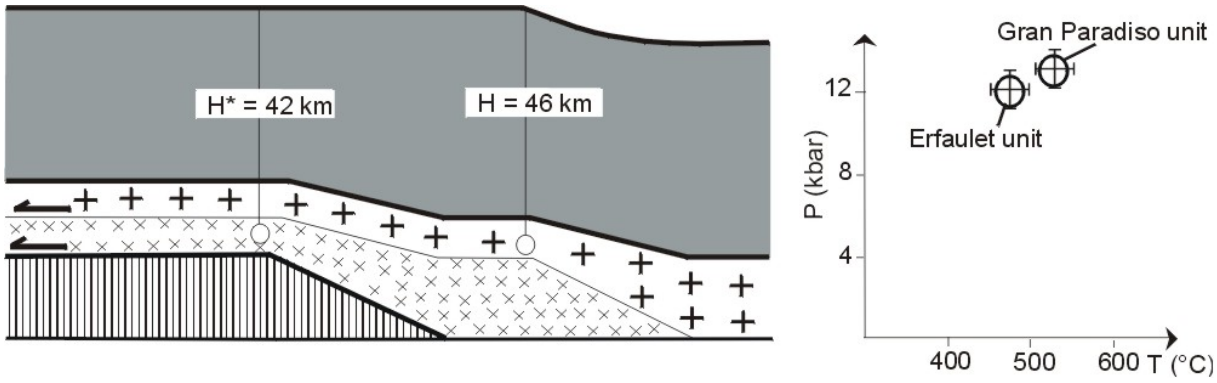

Fig.4.1: Schematic nappe sequence in northern part of Western Alps and maximum PT conditions for Gran Paradiso and Erfaulet units; emplacement of higher pressure Gran Paradiso unit onto Erfaulet unit demands that 4-11 km of vertical section was removed during nappe emplacement.

Exhumation is a generic term describing the return of once deep-seated metamorphic rocks to the Earth's surface. Exhumation of high-P rocks has been discussed in recent studies within the context of the orogenic-wedge dynamics (e.g. Platt, 1986, 1987, 1993; Brandon, 1990, 1995; Ring & Brandon, 1994, 1999; Ring et al., 1999). The initial process of deep structural burial is ascribed to subduction of the slab beneath the overriding thrust wedge, followed by lithospheric underplating at the base and high pressure metamorphic overprinting. The contractional deformation itself, however, does not explain how high-P rocks were brought back to the surface, since adding material at the bottom just increases the thickness of the wedge and does not cause the overburden to be removed (Platt, 1986). Exhumation occurs by three processes: erosion, normal faulting, and ductile thinning. The processes are important, not only for the exhumation that they cause, but also for their influence on the formation of orogenic topography and the contribution to production of synorogenic sediments (Ring et al. 1999). In the following part, a brief description of these processes is given **(Fig.4.2)**.

Ductile Thinning: Ductile thinning is defined as the change in thickness of the overburden above a material point because of ductile deformation within the overburden. Feehan & Brandon (1999) introduced a one- dimensional steady-state model to estimate the contribution of ductile deformation to exhumation of a generic accretionary wedge. Ductile thinning processes can either aid or hinder exhumation, depending upon whether ductile flow causes vertical thinning as associated with the formation of subhorizontal foliation, or vertical thickening as associated with the formation of a subvertical foliation. The presence of a subhorizontal foliation is generally diagnostic of ductile thinning **(see Fig.4.2)**. The general observation of subhorizontal foliations in the internal zones of many orogens shows that ductile thinning commonly aids exhumation (Selverstone 1985; Wallis 1992, 1995; Wallis et al. 1993; Platt 1993; Mortimer 1993; Ring 1995; Krabbendam & Dewey 1998; Ring et al. 1999). Ductile thinning by itself cannot fully exhume rocks and an additional exhumation process is required to bring rocks back to the earth's surface (Platt et al. 1998; Feehan & Brandon 1999). In the simplest case, where exhumation is entirely controlled by ductile thinning, exhumation by ductile thinning is given by the average stretch in the vertical because this tells how much the vertical has changed in thickness. However, if the exhumation occurs by additional processes as well, it is more difficult to quantify the contribution of ductile thinning to exhumation. In this case, the vertical rate at which a rock

moved through its overburden and the rate of thinning of the remaining overburden at each step along the exhumation path have to be considered (Feehan & Brandon 1999). The general conclusion is that the contribution of ductile thinning to exhumation will always be less than that estimated from the vertical stretch only.

Normal Faulting: The most commonly cited evidence for normal faulting is the presence of younger over older or low-grade on high-grade tectonic contacts, where large faults, with low to moderate dips, have placed younger above older rocks or low-grade rocks on high grade rocks, and in the process have cut out a significant thickness of stratigraphic or metamorphic section. High P/T rocks may be exhumed in the footwalls of faults that have a large-magnitude component of normal displacement **(Fig.4.2)**. A widely perceived driving force for such normal faulting is underplating of the forearc, possibly by a subducted bathymetric high, which leads to overthickening, gravitational collapse, and extension of a tapered accretionary prism (Lister et al. 1984; Platt 1986). Normal faulting may also be driven by oblique convergence (Avé Lallemant & Guth 1990). In addition, the exhumation rate during the normal faulting is a function of both slip rate and fault dip (Ring et al., 1999). Many studies of active convergent margins have documented underplating (e.g. Westbrook & Smith 1993; Clowes et al. 1987; Fuis & Plafker 1991) and normal faulting (e.g. Crespi et al. 1996; McNeill et al. 1997). Normal faulting has been suggests as the exhumation mechanism of high P/T rocks from the modern and ancient convergent margins around the world, including the Franciscan complex of California (Jayko et al. 1987; Harms et al. 1992), the Dora Maria ultra-high pressure metamorphic rocks of the western Alps during the later stage of the exhumation (Avigad 1992; Michard et al. 1993) and the Tauern Window of the eastern Alps (Selverstone 1988).

Erosion: Erosion is one of the important processes to exhume high P/T (metamorphic) rocks of the overburden as the deeper-level rocks rise through the crust. Surface uplift and erosion rate may be controlled by orogen-thickening mechanisms such as underplating, thrusting, and contractional pure shear (Platt 1993; Thompson et al. 1997). Early geologists observed that mountainous regions eroded faster than adjacent lowlands, and that ancient mountain belts were commonly flanked by thick synorogenic deposits that could be traced by provenance to erosional sources within the orogen. The large volumes of detrital deposits found adjacent to almost all convergent continental orogens provides ample evidence that erosion is a significant exhumation process.

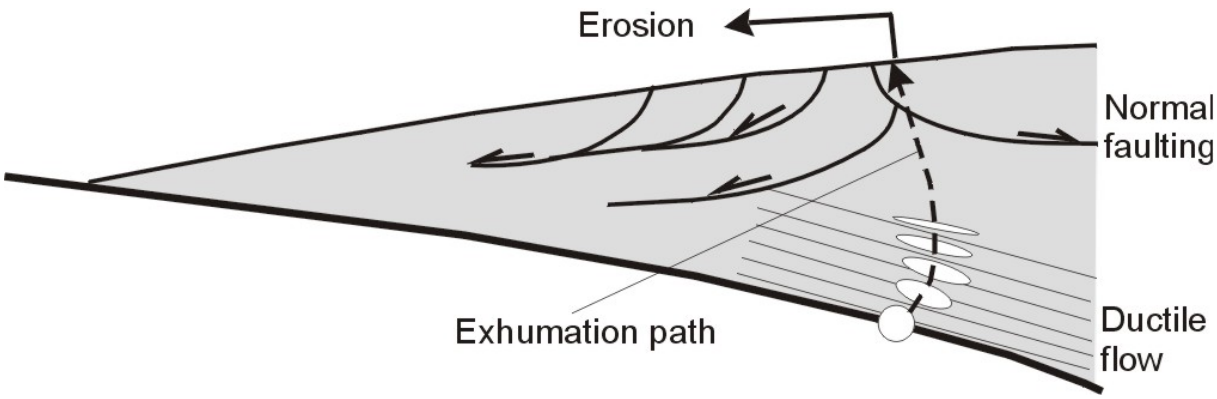

Fig.4.2: Schematic illustration of the three exhumation processes: normal faulting, ductile flow and erosion (After Ring et al. 1999).

Finite strain measurements were already presented in chapter 3. In conjunction with the microprobe data, they record the amount of ductile strain experienced by rocks during deformation under high-pressure conditions within the orogen. Finite strains indicate the average of shortening is about 58% in the vertical direction associated with horizontal extension during high-pressure nappe stacking. Thus, one would expect that ductile thinning has played a significant role in the exhumation of rocks from the Gran Paradiso unit **(Fig.4.1)**. Feehan & Brandon (1999) have pointed out that the orientations of finite strains have a strong influence on the relation between ductile thinning of the overburden and exhumation. Wedge models (e.g. Willet et al. 1993) suggest that directions and magnitudes of principal strains do not remain constant, but vary during deformation. Therefore, strain measurements and exhumation modelling can be only used to quantify the end-product, which possibly arose from a complex interdependence of the thickening and thinning processes.

Kassem & Ring (2004) suggest that the vertical shortening, which accompanied the accumulation of finite strain during high-pressure metamorphism, has led to the thinning of the overriding nappe package and, consequently, the final overburden above the Erfaulet unit was reduced. The interpretation of the final movement of the Gran Paradiso unit onto the Erfaulet unit shall be elaborated upon within this chapter. In order to properly estimate the contribution that vertical ductile shortening exerted upon total exhumation of the overriding nappe package, it is needed to consider both the vertical rate at which the rocks moved through its overburden and the rate of thinning of the remaining overburden at each step along the exhumation path.

Another possibility how the overburden can be removed is that one or more normal faults higher up in the section operated at the same time as the nappes in the Gran Paradiso massif formed. Reddy et al. (1999) showed that the southeastern portion of the Combin fault (Gressoney shear zone) was active as an extensional shear zone between 36-45 Ma. It seems that extension across the Combin fault unroofed the (ultra) high-pressure Zermatt Sass zone during thrusting of the latter onto the Gran Paradiso massif. This would explain the excision of 20-25 km of section between the Zermatt-Saas zone and the Gran Paradiso unit. The exact timing of high-pressure metamorphism in the Gran-Paradiso unit is needed to further discuss whether normal faulting aided exhumation of the Gran Paradiso unit during its emplacement onto the Erfaulet unit.

In addition, erosion could also explain the exhumation of the Gran Paradiso unit as it was thrust onto the Erfault unit. There are no Eocene erosion rates known from the Alps and therefore the contribution of erosion to exhumation remains unknown. Reddy et al. (1999) suggested that during extensional movement on the Combin fault no significant unroofing of the hanging wall occurred implying that erosion rates were small. Rates of thrusting and normal faulting in the Eocene and Early Oligocene in the Alps were fast (Reddy et al. 1999) and therefore one can assume that thrusting of the Gran Paradiso unit onto the Erfault unit occurred within a few million years. In this case, high erosion rates of 0.5-2 km Myr^{-1} would have to be envisioned to explain the metamorphic break between the Gran Paradiso and Erfault units. Such high rates appear to be unrealistic for the Eocene Alps because mountains relief was not accomplished before the Oligocene (Spiegel, et al., 2000 and Trümpy, 2001).

4.2 Review of Geochronological data, Residence time and average exhumation rates:

Many authors who discussed the timing of high-pressure metamorphism in the Gran Paradiso massif (e.g. Meffan et al., 2004) concluded that the high-pressure metamorphism thereabout started at ca. 43 Ma and continued up to at least 36 Ma. Internal units of the Western Alps were generally affected by a greenschist to lower amphibolite facies overprint. This is thought to have taken place during the Oligocene (Hunziker et al., 1992). Recent geochronological studies have aided in resolving problems pertaining to deciphering age relationships of specific greenschist facies deformation fabrics (e.g. Freeman et al., 1997; Reddy et al., 1999; Cartwright & Barnicoat, 2002). Localised deformation under greenschist conditions within and around the Gran Paradiso basement has been dated at 38-34 Ma (average about 36 Ma), using Rb-Sr on white mica (Inger & Ramsbotham, 1997). The post-Alpine cooling path of the Gran Paradiso massif was investigated by Hurford & Hunziker (1989) who determined fission track ages on zircon (closure 200-250°C) of 30±1Ma and on apatite (closure 60-120°C) between 24 and 20Ma. Zircon and apatite track ages for the Gran Paradiso indicate a monotonic cooling of ~10°C/Ma during the Miocene to recent. These data suggest that the Gran Paradiso massif was within a few km of the surface by *c.* 20Ma.

The timing information given above is used here to estimate wedge residence times and exhumation rates for our study areas in Gran Paradiso unit **(Table 4.1)**. The age of thrusting nappes onto each other is closely approximately by the age of peak metamorphism, which spans a period of time between 2 and 7 Ma (with an estimated average of 4 Ma). In addition, the depth of the underplating is about 42-49 km when maximum metamorphic pressure for Gran Paradiso unit in the range 12-14 kbar and 500-550°C (assuming an average density of 2800 kg m^{-3}), whereas high-pressure metamorphism of the Erfaulet unit occurred at 11-13 kbar and 450-500°C, corresponding to a depth of about 38.5- 45.5 km. In this case, the difference pressure between two units can considerable about 1-3 kbar (3.5-10.5 km depth). Based on metamorphic depths and residence times, the average exhumation rate would be about 0.5-5.0 km/m.y.

Table 4.1: Summarising all input parameters required by Exhume-program.

	Model Parameters and Initial Conditions		
Orogenic Parameters			
Depth of Initial acceration		46 Km	
Residence time in Wedge	2	4	6
Azimuth of Transport Direction		100°	
Directions and Magnitudes of the Principal Stretches (Sx, Sy, Sz)			
Extention(trend, plunge and Sx)		278, 09, 2.29	
Intermediate(trend, plunge and Sy)		08, 03, 1.05	
Shortening(trend, plunge and Sz)		114, 81, 0.42	
Stretches, Orogenic Coordinate frame			
Across-strike		1.75	
Parallel-strike		1.05	
vertical		0.43	

4.3 Results and implications:

The results of the exhumation calculation are presented in **Table 4.2** as well as in **Fig. 4.3**. The data indicate that the ductile strain contributed about 11 ± 0.6 km/m.y for a proportional strain rate. Feehan and Brandon (1999) show that a proportional strain rate approximates a situation where strain rates are governed by parameters that increase with depth, such as deviatoric stress and temperature. The percentage of total exhumation due to ductile flow is about 25 %. In addition, the calculated contribution of erosion and normal faulting represent 75% of the exhumation, a value which is equivalent to some 34.4 km of thickness for a proportional strain rate (**Table 4.2)**.

Ductile strain is highest at the base of the wedge and decreases to zero at the top, following the proportional strain rate law. This means that most of the finite strain is acquired in the deep part of the wedge. During their ascent rocks accumulate strain over the thickness of the orogenic wedge and finally reach the surface with a certain amount of finite ductile strain. Thus, the exhumation is a function of the integrated strain along the vertical deformation path and is not simply related to the total finite strain. As a consequence, the fraction of ductile thinning deduced from finite strains is necessarily less than, or equal to, the amount of shortening in the vertical direction.

If the strain measurements are considered with respect to orogenic coordinates (average present strike of the orogen is 100°), averages of across-strike, parallel to strike in the horizontal and vertical stretches of 1.75, 1.05, and 0.43 are obtained respectively **(Table4.1)**. This indicates an average of across-strike horizontal extension in the range of 75%. This value highlights a W/WNW direction (extension) during the deformation of the Gran Paradiso unit. The average parallel-to-strike horizontal strain is 5% extension. This indicates that the deformation was close to plane strain.

Results pertaining to the model calculation are shown in Fig. 4.3. They illustrate the exhumation and strain history for a proportional strain rate. For the proportional strain, the model favours a slightly faster rate (á = 13.1 km/m.y.) and a thinning rate due to erosion and normal faulting of about 5.7 km/m.y. In addition, the thinning rate for ductile flow is close to 7.4 km/m.y. The principal stretches display a non-linear disposition (indicated by the curvatures Sx and Sz – **Fig.4.3**).

In accord with the current study, it may be concluded, that deformation associated with thrusting in the Gran Paradiso unit involved significant vertical shortening with the horizontal extension. In essence, the exhumation data suggest that the vertical shortening would have played a vital role with reference to interpreting the missing crust between the Gran Paradiso and Erfaulet units as well as the juxtaposition of the high-pressure rocks against their lower-pressure counterparts. Final emplacement of the Gran Paradiso unit onto the Erfaulet unit was probably achieved during the underplating event.

Table 4.2: The result of the exhumation

Residence time inside orogen (m.y.)	2	4	6
	Proportional Strain Rate		
Thinning Rate due to erosion & normal faulting (km/m.y.)	17.2	8.6	5.7
Thinning Rate due to ductile flow (km/m.y.)	22.1	11	7.4
Rate of basal accretion (km/ m. y.)	39.3	19.6	13.1
Total exhumation due to erosion & normal faulting	34.4	34.4	34.4
Total exhumation due to ductile flow	11.6	11.6	11.6
Percentage of Total exhumation due to ductile flow (%)	25.1	25.1	25.1
Strain Rates: Across-Strike (%/myr)	45.7	23.9	15.2
Strain Rates: Parallel-Strike (%/myr)	2.8	1.4	0.9
Strain Rates: Vertical (%/myr)	-47.9	-23.9	-15.9

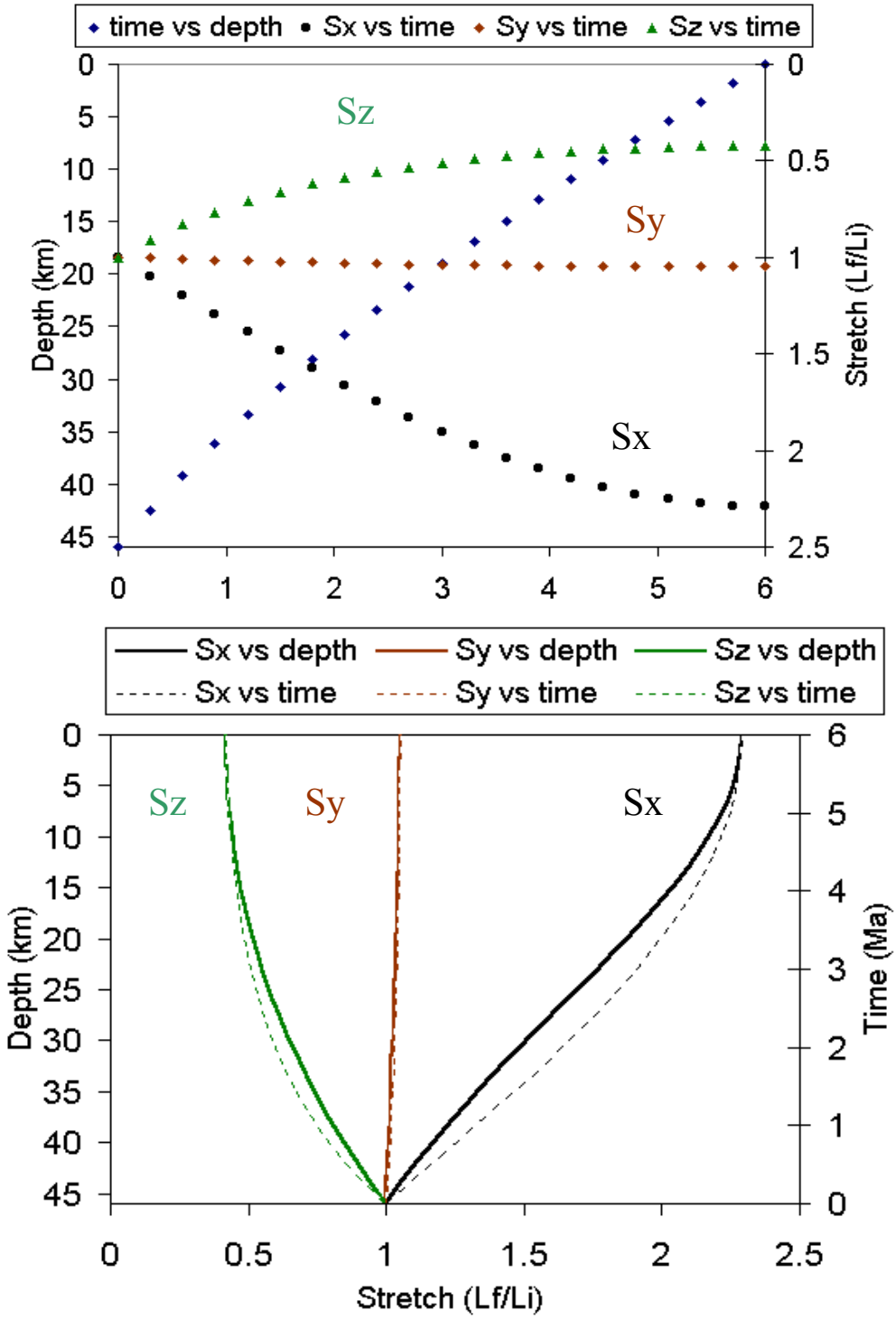

Fig.4.3: Plots of model results for tensor average strains, illustrating the exhumation and strain history for proportional strain rates, respectively; depth of initial accretion is 46 km; residence time within a steady-state wedge is 6myr.

5. Summary and Discussion

Subhorizontal foliation and shearing

The chemical data indicate no volume change with progressive deformation of the augengneiss. Minor or no volume changes are expected in high-grade rocks in which porosities during deformation are probably very small. Because of isochoric deformation the strain data reflect flattening strain type. This indicates that the accumulation of ductile deformation during underplating was not by simple shear and involved vertical shortening produced by a component of pure shear. Pure shear-related vertical shortening caused the subhorizontal foliation in the Gran Paradiso massif and adjacent units.

The development of a subhorizontal foliation by simple shear nappe stacking alone appears to be an unreasonable alternative. The latter scenario demands very high shear strains of the order of >10 and the rotation of material lines into a subhorizontal position would lead to strain ellipses with aspect ratios of ~100 throughout the entire thickness of nappes. To the best of the author's knowledge, high strains of ~100 have never been reported across a whole nappe. Therefore, Kassem and Ring (2004) envisage that nappe imbrication associated with a component of pure shear flattening is a general process causing flat-lying foliations in the internides of many orogens. The faster rotation of objects in pure shear than in simple shear also makes a pure shear component of deformation more likely for producing subhorizontal foliations across nappes.

On the main-phase foliation, a W/WNW-trending stretching lineation developed **(Fig.3.7)**. The structure of the area is dominated by a pervasive, subhorizontal main-phase foliation. The main-phase foliation is subparallel to the nappe contact of the Gran Paradiso massif with the overlying Zermatt-Saas zone and therefore defines a broad regional dome structure. Vissers & Compagnoni (1984) made the important observation that this foliation cuts the tectonic contact between the Gran Paradiso unit and the Erfaulet unit at a low angle. These authors argued that the Gran Paradiso massif is a gneiss-cored fold nappe with the Erfaulet unit occurring in the axial plane of the fold nappe. The data introduced in chapter 3 and corroboration (Kassem and Ring, 2004) reveal that stretching lineations during subduction-related underplating assume a general trend of W/WNW and that associated kineamatic indicators, in general, record a top-W tectonic transport. Vissers & Compagnoni (1984) and Vearncombe (1985) came to similar conclusions; Butler & Freeman (1996) also

reported top-W tectonic transport from the contact of the Gran Paradiso massif with the overlying Zermatt-Saas zone **(Fig.5.1)**. Further evidence for top-W tectonic transport during high-pressure metamorphism in the Western Alps comes from the studies by Philipot (1990), Froitzheim (2001), Reddy et al. (2003), Ring & Merle (1992) and Ring (1992, 1995). According to Schmid & Kissling (2000) early E-W shortening caused ~30 km of top-W thrusting of the Gran Paradiso massif onto its underlying units **(Figs. 2.4 & 5.1)**.

However, the problem with interpreting the stretching lineations as the tectonic transport direction is that such an interpretation is only valid for a simple-shear deformation, which is not supported by the strain data. The observation that deformation in large parts of the Gran Paradiso massif is, in general, distinctly non-coaxial with a dominant top-W sense of shear suggests that ductile deformation in the nappe is related to shear coupling on the thrusts which bound the Gran Paradiso massif. Therefore, it seems plausible to assume that this shear coupling produced the regional consistently oriented stretching lineation.

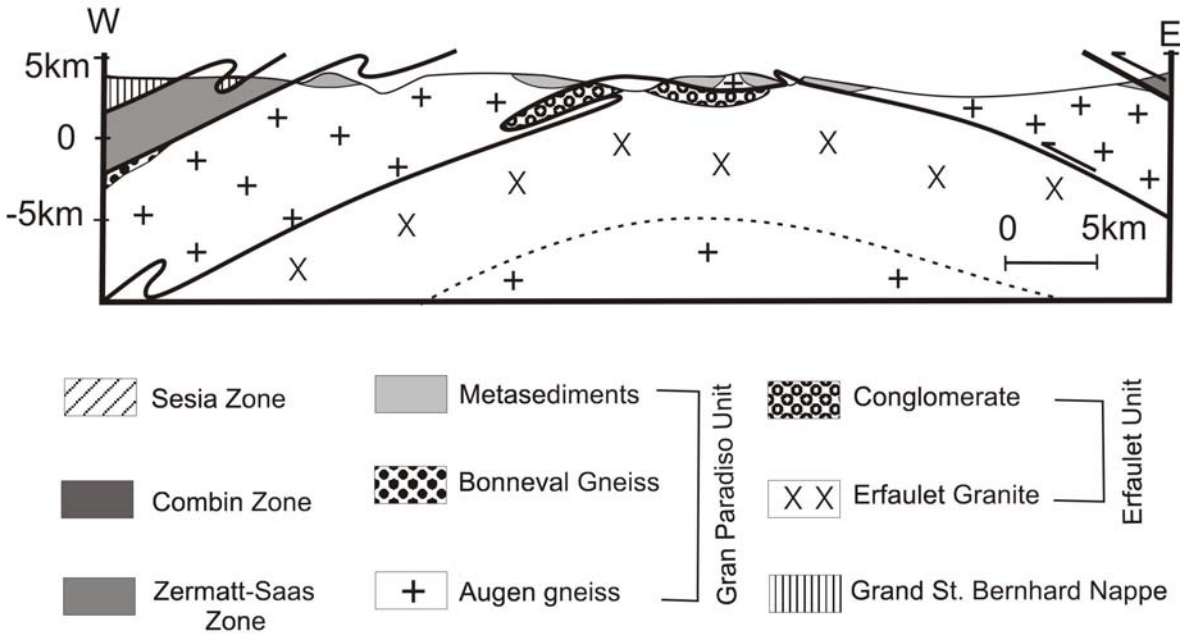

Fig. 5.1: Cross-section E-W showing broad domal structural; Erfaulet unit forms base of exposed section and crops out in major valleys.

Heterogeneous deformation and nappe emplacement

The deformation/metamorphism relationships in conjunction with the thermobarometric data of Borghi et al. (1994, 1996) indicate that feldspar ductility at temperatures >~450-500°C occurred only during deformation at peak metamorphic conditions. Therefore, the R_f/ϕ strains as derived from ductile-deformed feldspar porphyroclasts can be associated with deformation at maximum burial depths during underplating of the rocks beneath the overriding plate. This conclusion is corroborated by similar microstructures from the Monte Rosa nappe, which also formed during maximum burial when the nappes were underplated beneath the overriding Adriatic plate (Ring & Merle 1992).

In addition, electron microprobe work was undertaken to determine if the analysed fabrics formed during high-P metamorphism. On the basis of chemical data, it may be summarized that: a) there is only one generation of high-Si phengite that has been detected within the compositional range of the three analysed samples; b) there is no retrograde transformation at the expense of phengite is observed; c) no chemical zoning is present. This implies that the motion, deformation and final structural juxtaposition of the Gran Paradiso unit against the Erfaulet took place during underplating and high-pressure metamorphism.

The lack of any obvious relationship between the strain magnitude and tectonic contacts may have two reasons: (1) the nappe contacts formed early during subduction under brittle to semi-brittle deformation conditions before the peak of high-pressure metamorphism. In this case, ductile strain was superimposed heterogeneously on the already assembled nappe structure. (2) The nappe contacts formed late, after high-pressure metamorphism ceased, i.e. ductile strain accumulated before the nappes formed. The fact that finite strain accumulated during high-pressure metamorphism indicates that the nappe contacts formed before the accumulation of ductile strain and thus during underthrusting. The observation of Vissers & Compagnoni (1984) that the main-phase foliation cuts the tectonic contact between the Gran Paradiso unit and the Erfaulet unit at a low angle corroborates this conclusion.

Although the strain magnitude does not show any relationships to nappe contacts, the strain type as expressed by the K value shows a distinct pattern in the Gran Paradiso massif. Kassem and Ring (2004) suggested that underplating was accompanied by vertical shortening and this explains flattening strain type in large parts of the Gran Paradiso massif.

The constrictional strain in the Erfaulet unit could be explained by the gneiss-cored fold-nappe model of Vissers & Compagnoni (1984). Dürr (1992) and Ring et al. (1988, 1989) showed that in fold hinges where an earlier foliation is overprinted at a high angle by a fold-related axial-plane foliation, the superposition of the strains results in prolate strain, whereas on the limbs of the fold flattening strain results. The gneiss-cored fold-nappe model of Vissers & Compagnoni (1984) implies that the Erfaulet unit occurs in the axial plane of the gneiss fold, whereas most parts of the Gran Paradiso unit should make up the limbs of the envisioned large-scale fold **(Fig. 5.2)**.

In this case, vertical shortening thinned the overriding nappe package and therefore the final overburden above the Erfaulet unit was reduced. It seems that the final movement of the Gran Paradiso unit onto the Erfaulet unit occurred during underplating and the accumulation of finite strain, which is in accord with top-to-the-W shear during high-pressure underplating. In other words, the nappes formed already during subduction but final nappe transport in the Gran Paradiso massif took place during subsequent underplating. The high-strain zone south of Pont **(Figs. 3.11, 3.13**) probably accomplished a considerable part of final nappe transport.

Another interesting feature in the high-pressure rocks of the Gran Paradiso massif is that intrusive relationships close to the contact with the overlying Zermatt-Saas zone are well preserved despite the fact that the rocks were transported down to depths of ~45 km and were subsequently exhumed rapidly. Similar intrusive relationships occur in the ultrahigh-pressure unit of the Dora Maira massif, which was exhumed very rapidly (Compagnoni et al. 1995). These examples indicate that Alpine (ultra)high-pressure metamorphism and associated heterogeneous and rapid deformation in the Alpine subduction zone left parts of the nappes mineralogically and/or structurally completely unaffected. Ring & Reischmann (2002) proposed that fast underthrusting and exhumation at great rates occurs when the bounding faults are very weak and that this is the reason why some high-pressure rocks are almost undeformed. However, the consistently oriented stretching lineations and top-to-the-W shear suggest at least some shear coupling at the thrusts that bound the Gran Paradiso massif. Furthermore, ductile strain reaching axial ratios in XZ sections of ~70 was superimposed heterogeneously on the existing nappe structure indicating that high strain accumulated, at least in part, after considerable movement at the bounding faults. In this case, the good preservation of pre-high-pressure structures close to nappe contacts was aided because the nappes formed early during subduction by brittle

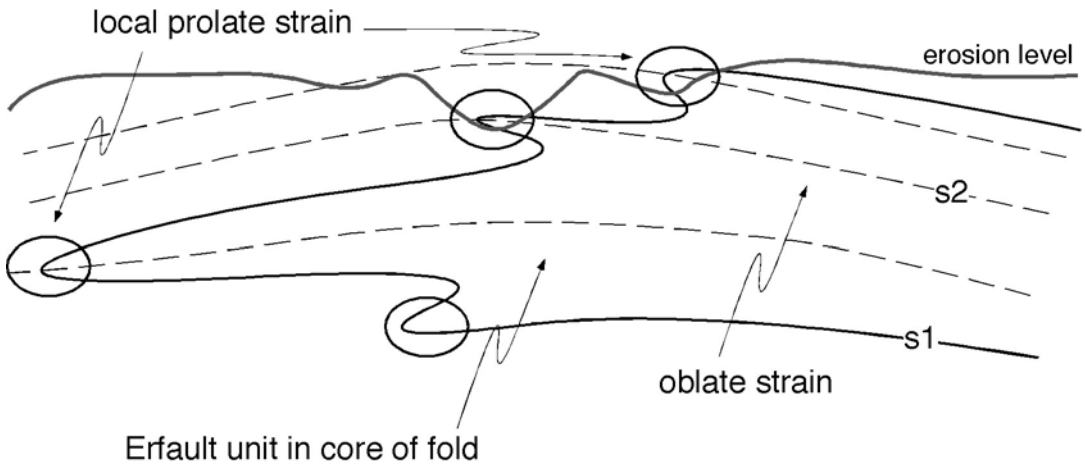

Fig. 5.2: Schematic structural model for occurrence of slightly constrictional strain in Erfaulet unit. Early S1 foliation parallel to tectonic contact between Gran Paradiso unit and Erfaulet unit is folded and forms gneiss-cored fold nappe of Vissers & Compagnoni (1984); S2 foliation is generally subparallel to S1, which explains flattening strain, but in hinge zones of F2 folds S2 is at high angle to S1 leading to local constrictional strain.

imbrication and were modified by extremely heterogeneous strain which allowed pre-existing structures to survive in low-strain areas between shear zones.

Implications of exhumation in the Gran Paradiso massif:

The high-pressure metamorphism in Gran Paradiso massif is due to deformation and final structural juxtaposition of the Gran Paradiso unit against the Erfaulet took place during underplating in Alpine subduction zone. The Gran Paradiso unit was thrust onto the Erfaulet unit; this event is characterized by a metamorphic break and was associated with subhorizontal foliation. The question is whatever vertical shortening during nappe emplacement caused the pressure break (about 1-3 kbar).

The results of the calculations (**Table 4.2**; **Fig.4.3**) indicate that vertical shortening is playing an important role during thrusting of the Gran Paradiso unit onto the Erfaulet unit. Furthermore, the exhumation data in chapter 4 indicate that the average exhumation rate would be about 0.5-5 km/m.y. The calculated exhumation rate in Gran Paradiso massif is not exceptional: in the Dora Maira massif Rubatto & Hermann (2001) estimated exhumation rates up to 34 km/m.y. These calculations illustrate that the contribution of ductile thinning to exhumation depends on interactions with the other exhumation processes (normal faulting and/or erosion), and it also depends on how ductile deformation is distributed with depth.

Normal faults, higher up in the section, have caused exhumation of the Gran Paradiso unit at the time when the higher was thrust onto the Erfaulet unit. Reddy et al. (1999) showed that the southeastern portion of the Combin fault (Gressoney shear zone) was active as an extensional shear zone between 36-45 Ma. It may be asserted that extensional processes, across the Combin fault, unroofed the (ultra)high-pressure Zermatt Sass zone during thrusting of the latter onto the Gran Paradiso massif; an inference that would explain the excision of 20-25 km of section between the two units. In essence, constraining of the exact timing of high-pressure metamorphism in the Gran-Paradiso unit is perceived to be a factor relevance. This would enable a further discussion on whether normal faulting aided exhumation of the Gran Paradiso unit during its emplacement onto the Erfaulet unit or otherwise.

Erosion as the third most probable exhumation mechanism (Ring et al. 1999) could also explain the exhumation of the Gran Paradiso unit and its emplacement through thrusting onto the Erfaulet unit. Nonetheless, there are no Eocene erosion rates known from the Alps and therefore the contribution of erosion to exhumation remains largely unknown.

Sedimentary evidence for the erosion of continental crust prior to the Oligocene is lacking in the Alpine flysch (Platt, 1986). Therefore, rather than removing the overlying rocks by erosion, a mechanism to transport the HP rocks through the overburden is necessary. However, It also appears that the Sesia-Lanzo zone and Gran Paradiso massif were near surface when part of the Dora Maira massif was metamorphosed within the range of over 100-km in depth. Indeed, the Sesia-Lanzo began its exhumation cycle approximately 35 Ma prior to HP metamorphism in the Dora Maira. Reddy et al. (1999) suggested that during extensional movement on the Combin fault no significant unroofing of the hanging wall has taken place. This implies that erosion rates were small. Rates of thrusting and normal faulting in the Eocene and Early Oligocene in the Alps were fast (Reddy et al. 1999) and therefore one would assume that thrusting of the Gran Paradiso unit onto the Erfaulet unit occurred within a few million years. Nevertheless, a sort of erosion (possibly in the range of 0.5-2 km Myr^{-1}) is to be envisioned: such a conjecture would help in explaining the metamorphic break between the Gran Paradiso and Erfaulet units.

.

6. Conclusions

Nappe stacking in the Gran Paradiso massif occurred early during subduction (*underthrusting event*) probably by brittle imbrication. Ductile strain was then superimposed on the nappe structure during high-pressure underplating of the nappe stack beneath the Adriatic plate in the Alpine subduction zone. Final emplacement of the Gran Paradiso unit onto the Erfaulet unit was probably achieved during the underplating event. Flattening strain indicates that the accumulation of ductile strain during underplating was not by simple shear. It is assumed to have involved a component of vertical shortening, which caused the subhorizontal foliation in the Gran Paradiso massif and, by inference, also in other Pennine gneiss nappes in the Alps.

The chemistry of phengite micas in samples from the Gran Paradiso massif supports that the analysed fabrics formed during high-P metamorphism. In essence, there is no change in the physical conditions to which the rocks were subjected during deformation. Thus, the motion, deformation and final structural juxtaposition of the Gran Paradiso unit against the Erfaulet unit took place during underplating and the high-pressure metamorphism as, equally, revealed by phengite barometry.

On the other hand, the exhumation during high-pressure metamorphism in the Gran Paradiso massif was indicated as a component of vertical shortening, which is responsible for the subhorizontal foliation within the nappes. On the basis of the exhumation data it is to be concluded that the vertical shortening would have played an important role to interpreting the missing crust between the Gran Paradiso and Erfaulet units as well as the juxtaposition of the high-pressure rocks against their low-pressure counterparts. It is asserted that the vertical shortening, which accompanied the accumulation of finite strain during high-pressure metamorphism, thinned the overriding nappe package and, therefore, the final overburden above the Erfaulet unit was reduced. Within this context and in order to, properly, estimate the impact of vertical ductile shortening that was exerted on the total exhumation of the overriding nappe package, it is necessary to consider both the vertical rate at which the rocks moved through the overburden, as well as the rate of thinning of the remaining overburden at each step along the exhumation path.

References

Avé Lallemant, H. G. and Guth, L. R. 1990: Role of extensional tectonics in exhumation of eclogites and blueschists in an oblique subduction setting: northeastern Venezuela. Geology, 18, 950-953.

Avigad, D. 1992: Exhumation of coesite-bearing rocks in the Dora Maira massif (western Alps, Italy). Geology, 20, 947-950.

Ayers, J.C. and Watson E. B. 1991: Solubility of apatite, monazite, zircon, and rutile in supercritical aqueous fluids with implications for subduction zone geochemistry. Philosophical Transactions Royal Society London Series A, 335, 335-375.

Ayers, J.C. and Watson, E. B. 1993: Rutile solubility and mobility in supercritical aqueous fluids. Contribution to Mineralogy and Petrology 114, 321-330

Bailey, C. M., Simpson, C. and De Paor, D. G. 1994: Volume loss and tectonic flattening strain in granitic mylonites from the Blue Ridge Province, Central Appalachians. Journal of Structural Geology 10, 1403-1416.

Ballèvre, M. 1988: Collision continentale et chemins P-T: I` unite pennique du Grand Paradis (Alpes occidentales). Thesis, Univ. Rennes, Mèm. et Doc. Du Centre Armoricain d'Etude structural des Socles, 19, 340p.

Ballèvre, M. and Merle, O. 1993: The Combin fault: compressional reactivation of a Late Cretaceous-Early Tertiary detachement fault in the Western Alps. Schweizerische Mineralogishche und Petrographishe Mitteilungen 3, 205-227.

Ballèvre, M., Kienast, J.R. and Vuichard, J.P. 1986: La "nappe de la Dent Blanche" Alpes occidentales, Deux unités austroalpines indépendantes. Eclogae Geologicae Helvetiae 79, 57-74.

Bearth, P. 1952: Geologie und Petrographie des Monte Rosa. Beiträge zur Geologischen Karte Schweiz NF 96, 94p.

Bearth, P. 1953: Gologischer Atlas der Schweiz 1:25000, Blatt Zermatt, mit Erläuterungen. Schweiz Geologishen Kommission.

Bearth, P. 1956: Geologische Beobachtungen im Grenzgebiet der lepontinischen und penninischen Alpen. Eclogae Geologicae Helvetiae 49, 279-290.

Bearth, P. 1962: Versuch einer Gliederung alpin-metamorpher Serien der Westalpen. Schweizerische Mineralogishche und Petrographishe Mitteilungen 42,127-137.

Bearth, P. 1967: Die Ophiolite der Zone von Zermatt-Sass. Beiträge zur Geologischen Karte Schweiz NF 130,130p.

Bearth, P. 1973: Gesteins-und Mineralparagenesen aus den Ophiolithen Zermatt. Schweizerische Mineralogishche und Petrographishe Mitteilungen 44, 299-334.

Bearth, P. 1976: Zur Gliederung der Bündnerschiefer in der Region von Zermatt. Eclogae Geologicae Helvetiae 69, 149-161.

Bearth, P. and Schwander, H. 1981: The post-Triassic sediments of the ophiolite zone Zermat-sass Fee and the associated manganese mineralizations. Eclogae Geologicae Helvetiae 74, 189-205.

Beccaluva, L., Dal Piaz, G.V. and Macciotta, G. 1984: Transitional to normal MORB affinities in ophiolitic metabasites from the Zermatt-sass, Combin and Antrona units, western Alps. Geologie en Mijnbouw. 63, 165-177.

Benciolini L., Martin S. and Tartarotti P. 1984: II metamorfismo eclogitico nel basamento del Gran Paradiso ed in Unitá Piemontesi della Valle di Campiglia. Memorie Societa Geologica Italiana 29, 121-157.

Bertrand, J., Pidgeon, R., Leterrier, J., Guillot, F., Gasquet, D. and Gattiglio, M. 2000: SHRIMP and IDTIMS U-Pb zircon ages of the pre-Alpine basement in the Internal Western Alps (Savoy and Piemont). Schweizerische Mineralogishche und Petrographishe Mitteilungen 80, 225-248.

Bertrand, J.M. 1968: Etude structurale du versant occidental Massif du Gran Paradiso (Alpes Graies). Geology of Alpine 44, 57-87.

Biino G. and Pognante U. 1989: Paleozoic continental- type gabbros in the Gran Paradiso nappe (Western Alps, Italy). Early-Alpine eclogitiztion and geochemistry. Lithos, 24, 3-19.

Bistacchi, A., Dal Piaz, G. V., Massironi, M., Zattin, M. and Balestrieri, M. L. 2001: The Aosta - Ranzola extensional fault system and Oligocene-present evolution of the Austroalpine-Penninic wedge in the northwestern. International Journal of Earth Science 90, 654-667.

Bois, J.P. and Fabre, J. 1956: Galerie Arc dans Tignes. Rapp. No. 2. B.R.G.M. A1040.

Borghi, A., Compagnoni, R. and Sandrone, R. 1992: Composite P-T path of the Gran Paradiso nappe: petrological constraints to the geodynamic evolution of the eclogitic continental crust of the Western Alps. Géology of Alpine, Série spéciale Résumés de colloquies 1**,** 8-9.

Borghi, A., Compagnoni, R. and Sandrone, R. 1994: Evoluzione Tettonica Alpina Del settore setten trionale Del Massiccio Del Gran Paradiso (Alpi Occidentali). Atti Ticinensi di Scienze Della Terra 1, 137-152.

Borghi, A., Compagnoni, R. and Sandrone, R. 1996: Composite P-T paths in the Internal Penninic Massifs of the Western Alps: Petrological constraints to their thermo-mechanical evolution. Eclogae Geologicae Helvetiae 89, 345-367.

Brandon, M. T., and Calderwood, A.R. 1990: High-pressure metamorphism and uplift of the Olympic subduction complex: Geology, v. 18, p. 1252-1255.

Brandon, M.T. 1995: Analysis of geologic strain data in strain-magnitude space. Journal of Structural Geology, 17, 1375-1385.

Brouwer, F.M. 2000: Thermal evolution of high-pressure metamorphic rocks in the Alps. Mededelingen van de Faculteit Aardwetenschapen, University Utrecht 199, 221p.

Buchs A., Chessex, R., Krummenacher, D., and Vuagnat M. 1962: Ages ´plomb total´ determines par fluorescence X sur les zircons de quelques roches des Alps. Schweizerische Mineralogishche und Petrographishe Mitteilungen, 42, 295-305.

Butler, R. W. H. and Freeman, S. 1996: Can crustal extension be distinguished from thrusting in the internal parts of mountain belts? A case history of the Entrelor shear zone, western Alps. Journal of Structural Geology 18, 909-923.

Callegari, E., Compagnoni, R. and Dal Piaz, G. V. 1969: Relitti di strutture intrusive erciniche e schisti a sillimanite nel massiccio Del Gran Paradiso. Bollettino Della Societa Geologica Italiana 88, 59-69.

Cartwright, I. and Barnicoat, A. C. 2002: Petrology, geochronology and tectonics of shear zone in the zermatt-Saas and Combin zones of the western Alps. Journal of Metamorphic Geology 20, 263-281.

Castelli, D and Compagnoni, R. 1994: High Pressure metamorphism in the western Alps, Editors Compagnoni, R., Messiga, B and Castelli, D., 16 th General meeting of the International Mineralogical Association, book to the field excursion, pp 3-22.

Chessex, R., Delanoye, M., Krummenacher, D., and Vuagnat M. 1964: Nouvelles determinations d´âges ´plomb total´ sur des zircons alpines. Schweizerische Mineralogishche und Petrographishe Mitteilungen, 44, 43-60.

Chopin, C. 1981: Talc-phengite: a widespread assemblage in high-grade pelitic blueschists of the Western Alps. Journal of Petrology, 22,628-650.

Chopin, C. 1984: Coesite and pure pyrope in high-grade blueschists of the Western Alps: a frist record andsome consequences. Contribution to Mineralogy and Petrology 86, 107-118.

Chopin, C., Henry, C. and Michard, A. 1991: Geology and Petrology of the coesite-bearing terrain, Dora Maira massif, Western Alps. European Journal of Mineralogy 3, 263-291.

Choukrone, P. and Gapais, D. 1983: Strain pattern in the Aar Granite (Central Alps): Orthogneiss developed by bulk inhomogeneous flattening. Journal of Structural Geology 5, 412-418.

Clowes, R. M., Brandon, M. T., Green, A. G., Yorath, C. J., Brown, A. S., Kanasewich, E. R. and Spencer, C. 1987: Lithoprobe-southern Vancouver Island: Cenozoic subduction complex imaged by deep seismic reflections. Canadian Journal of Earth Sciences, 24, 31-51.

Compagnoni R., Hirajima T. and Chopin C. 1994: Ultra-high-pressure metamorphic rocks in Western Alps. In R.G. Coleman and X. Wang (eds.), “Ultrahigh pressure metamorphism”. Cambridge Univ. Press, Chapter 8.

Compagnoni, R. and Prato, R. 1969: Paramorfosi di cianite su sillimanite in scisti pregranitci Del Massiccio del Gran Pardiso. Bollettino Della Societa Geologica Italiana 88, 537-549.

Compagnoni, R., 1977: The Sesia-Lanzo Zone; high pressure-low temperature metamorphism in the Austroalpine continental margin. Petrologia 33, 335-374.

Compagnoni, R., Dal Piaz, G. V., Hunziker, J.C., Gosso, G., Lombardo, B. and Williams, P. F. 1977: The Sesia-Lanzo zone: a slice of continental crust with Alpine HT-LT assemblages in the Western Italian Alps. Rendiconti Della Societa Italiana di Mineralogia Petrologia 33, 281-334.

Compagnoni, R., Elter, G., and Lombardo, B. 1974: Eteroger stratigrafica del complesso degli Gneiss Minuti nel massicritallino del Gran Pradiso. Memorie della Societa Geologica Italiana 227-239.

Compagnoni, R., Hirajima, T. and Chopin, C. 1995: Ultra-high – pressure metamorphic rocks in the Western Alps, in Coleman, R. G. and Wang, X, eds., Ultrahigh-pressure Metamorphism. Cambridge University Press p. 206-243.

Correns, C. W. 1978: Ti-behaviour during weathering and alteration of rocks. In Handbook of Geochemistry (edited by Wedepohl, K. H.), II/ 2, 22-G, 1-3.

Coward, M and Dietrich, D 1989: Alpine tectonics-an overview. In: Coward, M.P., Dietrich, D., Park, R. (eds.). Alpine Tectonics. Geological Society of London Special Publication 45, 1-29.

Coward, M. P. 1976: Strain within ductile shear zones. Tectonophysics 34, 184-197.

Crespi, J. M., Chan, Y.C. and Swaim, M. S. 1996: Synorogenic extension and exhumation of the Taiwan hinterland. Geology, 24, 247-250.

Dal Piaz, G. V. 1966: Gneiss ghiandoni, marmi ed anfiboliti antiche del ricoprimento Monte Rosa nell alta Valle d´Ayas. Bollettino Della Societa Geologica Italiana 85, 103-132.

Dal Piaz, G. V. 1974: Le metamor-phisme de haute pression et basse température dans l'evolution structurale du basin ophiolitique alpino-apenninique. Schweizerische Mineralogishche und Petrographishe Mitteilungen 54, 399-424.

Dal Piaz, G. V. and Ernst, W.G. 1978: Areal geology and petrology of eclogites and associated metabasites of the Piemonte ophiolite nappe, Breuil-St. Jacques area, Italian Western Alps. Tectonophysics 51, 99-126.

Dal Piaz, G. V. and Lombardo, B. 1986: Early Alpine eclogite metamorphism in the Penninic Monte Rosa-Gran Paradiso Basement nappes of the northwestern Alps. Geological Society of American Memoires 164, 249-265.

Dal Piaz, G. V., Hunziker, J. C., and Martinotti, G. 1972: La zona Sesia-Lanzo e l´evoluzione tettonico-metamorphica delle Alpi Nordoccidentali Interne. Memorie Societa Geologica Italiana, 11,433-460.

Dewey, J. F., Helman, M. L., Turco, E., Hutton, D. H. W. and Knott, S. D. 1989a: Kinematics of the western Mediterranean. In M. P. Coward, D. D. Dietrian and R. G. Parke (Eds), Alpine Tectonics (pp. 265-283). Bath: Geol. Lond. Spec. Publ. 45.

Dürr, S. 1992: Structural history of the Arosa Zone between the Platta and Err nappes east of Mamorera (Grisons): Multiphase deformation at the Penninic-Austroalpine plate boundary. Eclogae Geologicae Helvetiae 85, 361-374.

Ernst, W.G. and Dal Piaz, G. V. 1978: Mineral parageneses of eclogitic rocks and related mafic schists of the Piemonte ophiolite nappe, Breuil-St.Jacques area, Italian Western Alps. American Mineralogist, 63, 621-640.

Escher, A. and Beaumont, C. 1997: Formation, burial and exhumation of basement nappes at crustal scale: a geometric model based on the Western Swiss-Italian Alps. Journal of Structural Geology 19, 955-974.

Feehan, J.G. and Brandon, M. T. 1999: Contribution of ductile flow to exhumation of low T-high metamorphic rocks: San Juan-Cascade Nappes, NW Washington State. Journal of Geophysical Research, 104, 10883-10902.

Flinn, D. 1962: On folding during three-dimensional progressive deformation. Quarternary Journal of Geological Society of London 118, 385-433.

Freeman, S.R., Inger, S., Butler, R. W.H. and Cliff, R.A. 1997: dating deformation using Rb-Sr in white mica; Greenschist facies deformation ages from the Entrelor shear zone, Italian Alps. Tectonics, 16, 57-76.

Frey M., Hunziker J.C., Bocquet J., Dal Piaz G.V., Jager E. and Niggli E. (1974). Alpine metamorphism of the Alps. A review. Schweizerische Mineralogishche und Petrographishe Mitteilungen, 54, 247-290.

Froitzheim, N. 2001: Origin of the Monte Rosa nappe in the Pennine Alps-A new working hypothesis. Geological Society of America 113, 5, 604-614.

Froitzheim, N., Schmid, S.M. and Frey, M. 1996: Mesozoic paleogeography and the timing of eclogite-facies metamorphism in the Alps: A working hypothesis. Eclogae Geologicae Helvetiae 89, 81-110.

Fry, N. 1979: Random point distributions and strain measurement in rocks. Tectonophysics 60, 89-105.

Fuis, G. S. and Plafker, G.1991: Evolution of deep structure along the Trans-Alaska Crustal Transect, Chugach Mountains and Copper River Basin, southern Alaska. Jouranl of Geophysical research, 96, 4229-4253.

Garnt, J. A. 1986: The isocon diagram - A simple solution to Gresens equation for metasomatic alteration. Economic Geology 81, 1976-1982.

Gebauer, D., Schert, H. P., Brix, M. and Schreyer, W. 1997: 35 Ma old ultrahigh-pressure metamorphism and evidence for very rapid exhumation in the Dora Maira Massif, Western Alps. Lithos 41, 5-24.

Goffé, B. and C. Chopin 1986: "High-pressure metamorphism in the Western Alps: zoneography of metapelites, chronology and consequences." Schweizerische Mineralogische und Petrographische Mitteilungen 66: 41-52.

Gosso, G., Dal Piaz, G. V., Piovano, V. and Polino, R. 1979: High pressure emplacement of early-Alpine nappes, postnappe deformation and structural levels. Memorie Societa Geologica Padova 32,15p.

Harms, T. A., Jayko, A. S. and Blake, M. C., JR 1992: Kinematic evidence for extensional unroofing of the Franciscan Complex along the Coast Range fault, northern Diablo Range, California. Teconics, 11, 228-241.

Hem, J. D. 1978: Al-behaviour during weathering and alteration of rocks. In: Handbook of Geochemistry (edited by Wedepohl, K. H.), II /I, 13-G, 1.

Henk, A., Franz, L., Teufel, S. and Oncken, O. 1997: Magmatic under-plating, extension, and crustal reequilibration: insights from a cross-section through the Ivrea Zone and the Strona-Ceneri Zone, Northern Italy. Journal of Geology 105, 367-377.

Henry, C., Michard, A. and Chopin, C. 1993: Geometry and structural evolution of ultra-high-pressure and high-pressure rocks from the Dora-Maira massif, Western Alps, Italy. Journal of Structural Geology 15, 965-981.

Hossack, J. R. 1968: Pebble deformation and thrusting in the Bygdin area (Southern Norway). Tectonophysics 5, 315-339.

Hsü, K.J. 1989: Time and place in Alpine orogenesis- the Fermor Lecture. In: Coward, M.P., Dietrich, D., Park, R.G.(eds). Alpine Tectonics. Geological Society of London Special Publication 45, 421-443.

Hunziker, J. C., Desmons, J. And Hurford, A. J. 1992: Thirty-Two Years of Geochronological Work in the Central and Western Alps: a Review on Seven Maps, 13, Mémoires Géologiques, Lausanne.

Hurford, A. J. and Hunziker, J. C 1989: A revised thermal history for the Gran Paradiso Massif. Schweizerische Mineralogishche und Petrographishe Mitteilungen 69, 319-329.

Inger, S. and Ramsbotham, W., 1997: Syn-convergent exhumation implied by progressive deformation and metamorphism in the Valle dell'Orco transect, NW Italian Alps. Journal of Geological Society of London 154, 667-677.

Jayko, A. S., Blake, M. C., JR and Harms, T. 1987: Attenuation of the Coast Range Ophiolite by extensional faulting, and nature of the Coast range ´Thrust´, California. Tectonics, 6, 475-488.

Kassem, O. and Ring, U. 2004: Underplating-related finite-strain patterns in the Gran Paradiso massif, Western Alps, Italy: heterogeneous ductile strain superimposed on a nappe stack.Journal of the Geological Society, London, Vol. 161, 2004, pp. 875–884.

Klein, J.A. 1978: Post-nappe folding southeast of the Misschabelrückfalte (Pennine Alps) and some aspects of the associated metamorphism. Leidse Geologische Mededelingen, 51, 233-312.

Krabbendam, M., and Dewey, J. 1998: Exhumation of UHP rocks by transtension in the western Gneiss Region, Scandinavian Caledonides. In: Holdsworth, R.E., Strachan, R. A. and Dewey, J. F. (eds) Continental Transpressional and Transtensional Tectonics. Geological Society of London, Special Publication, 135, 159-181.

Lardeaux J. M, Gosso G., Kienast J.-R. and Lombardo B. 1982: Relations entre le mètamorphisme et la dèormation dans la zone Sèsia-Lanzo (Alpes Occidentales) et le problème de l'èclogitisation de la croŭte continentalle**.** Bulletin Society of Geological France, 24, 793-800.

Le Goff E. and Ballévre M. 1990: Geothermobarometry in albite-garnet orthogneisses: A case study from the Gran Paradiso nappe (Western Alps). Lithos, 25, 261-280.

Lister, G.S., Banga, G. and Feenstra, A. 1984: Metamorphic core complexes of Cordilleran type in the Cyclades, Aegean Sea, Greece. Geology, 12, 221-225.

Mancktelow, N. 1990: The Simplon fault zone. Beiträge zur Geologischen Karte Schweiz 63, 1- 74.

Marthaler, M. and Stampfli, G. M. 1989: Les schistes lustrés à ophiolites de la nappe du Tsaté, un ancien prisme d'accrétion issu de la marge active apulienne. Schweizerische Mineralogishche und Petrographishe Mitteilungen 69, 211-216.

Massonne, H. J. and Schreyer, W. 1987: Phengite geobarometery based on the limiting assemblage with K-feldspar, phlogopite, and quartz. Contributions to Mineralogy and Petrology 96,212-224.

Massonne, H.J. and Chopin, C. 1989: P-T history of the Gran Paradiso (western Alps) metagranites based on phengite geobarometry. In: Daly, J.s., Cliff, R. A. and Yardley, B.W.D.(eds). Evolution of metamorphic belts. Geological Society of London Special Publication 43, 545-549.

McNeill, L. C., Piper, K.A., Goldfinger, C., Kulm, L. D. and Yeats, R.S. 1997: Listric normal faulting on the Cascadia continental margin. Journal of Geophysical Research, 102, 12123-12138.

Meffan-Main, S. Cliff, R. A., Baricoat, A.C., Lombardo, B. and Compagnoni, R. 2004: A Tertiary age for Alpine high-pressure metamorphism in the Gran Paradiso massif, Western Alps: a Rb-Sr microsampling study. Journal of Metamorphic Geology 22, 267-281.

Mehnert, K.R. 1975: The Ivrea Zone- A model of the deep crust. Neues Jahrbuch für Geologie Paläontologie Abhandlungen 125, 156-199.

Michard, A., Chopin, C. and Henry, C. 1993: Compression versus extension in the exhumation of the Dora-Maira coesite-bearing unit, Western Alps, Italy. Tectonophysics, 221, 173-193.

Milnes, A. G., 1978: Structural zones and continental collision, Central Alps, Tectonophysics, 47, 369-392.

Milnes, A. G., Greller, M. and Mueller, R. 1981: Sequence and style of major post-nappe structures, Simplon-Pennine Alps. Journal of Structural Geology 3, 411-420.

Mortimer, N. 1993: Geology of the Otago schist and adjacent rocks, 1: 500000; Map 7. Institute of Geological and Nuclear Sciences, Lower Hutt, New Zealand.

O´Hara, K. 1990: State of strain in mylonites from the western Blue Ridge province, Southern Appalachians: The role of volume loss. Journal of Structural Geology 12, 419-430.

O´Hara, K. and Blockburn, W. H. 1989: Volume-loss model for trace element enrichments in mylonites. Geology 17, 524-527.

Owens, W. H. 1984: The calculation of a best-fit ellipsoid from elliptical sections on arbitrarily oriented planes. Journal of Structural Geology 6, 571-578.

Pangaud, G., Lameyre, J. and Michel, R. 1957: Age absolu des migmatites du massif du Grand Paradis (Alpes franco-italiennes). Acadmic Science Paris Séries D 245, 331-333.

Paquette, J. L., Montel, J. M. and Chopin, C 1999: U-Th-Pb dating of the Brossasco ultrahigh-pressure metagranite, Dora-Maira Massif, Western Alps. European Journal of Mineralogy 11(1): 69-77.

Park, R.G. 1983: Foundation of structural Geology, pp135.

Pawlig, S. 2001: Geological Evolution of the Monte Rosa: Constrains from Geochronology and Geochemistry of a Talc-Kyanite choloritoid shear Zone with the Monte Rosa Granite (Monte Rosa Nappe, Italian Western Alps), Ph.D theses, pp149.

Peach, C. J. and Lisle, R. J. 1979: A fortran IV program for the analysis of tectonic strain using deformed elliptical markers. Computer & Geoscience 5, 325-334.

Pfeifer, H. R., Colombi, A. and Ganguin, J. 1989: Zermatt-Saas and Antrona zones: A petrographic and geochemical comparison of polyphase metamorphic ophiolites of the West-Central Alps. Schweizerische Mineralogishche und Petrographishe Mitteilungen 71, 217-236.

Pfiffner, O. A., 1992: Alpine Orogeny, in Blundell, D., Freeman, R., and Mueller, S., editors, The European Geotraverse: Cambridge, Cambridge university press, p. 180-190.

Pfiffner, O.A., Lehner, P. Heitzmann, P., Mueller, S. and Steck, A. 1997: Deep Structure of the Alps: Results from NRP 20, 380, Birkhäuser, Basel, Switzerland.

Philippot, P. 1990: Fluid melt-rock interaction in mafic eclogites and coesite-bearing metasediments: constrains on volatile recycling during subduction. Chemical Geology 108, 93-112.

Pickles-C-S, Kelley-S-P, Reddy-S-M and Wheeler-J 1997: Determination of high spatial resolution argon isotope variations in metamorphic biotites. Geochimica et Cosmochimica Acta. 61; 18, Pages 3809-3833.

Platt, J. 1987: The uplift of high-pressure low-temperature rocks. Philosophical Transactions of the Royal Society of London, Series A, 321, 87-103.

Platt, J. 1993: Mechanics of oblique convergence. Journal of Geophysical Research, 98 (B9), 16239-16256.

Platt, J. P 1986: Dynamics of orogenic wedges and the uplift of high-Pressure metamorphic rocks. Geological Society of American Bulletin 97, 1037-1053.

Platt, J. P. 1997: The European Alps. In: Van der Pluijm, B.A, and Marshak, S. (editers.) Earth structure: an introduction to structural geology and tectonics. WCB/MC Grow-Hill, Dubuque, Iowa, 408-415.

Platt, J. P. and Lister, G. S. 1978: Déformation, metamorphism mécanismes d´écoulement dans le massif de la Vanoise, Apenniques françaises- Acadmic Science Paris Séries D: 895-899.

Platt, J. P. and Vissers 1980: Extensional structure anisotropic rocks- Journal of Structural Geology, 2,397-410.

Platt, J., Soto J. I., Whitehouse, M. J., Hurford, A. J. and Kelley, S. P. 1998: Thermal evolution, rate of exhumation, and tectonic significance of metamorphic rocks from the floor of the Alboran extensional basin, Western Mediterranean. Tectonics, 17, 671-689.

Pognante U. 1989: Early alpine eclogitization in talc/chloritoid bearing Mg-metagabbros in jadeite-Fe-omphacite bearing metatrondhjemites from the ophiolites of the western Alps. Rendiconti Della Societa Italiana di Mineralogia Petrologia, 43, 687-704.

Pognante U., Talarico, F., Rastelli, N. and Ferrati, N. 1987: High-pressure metamorphism in the nappes of the valle dell´Orco traverse (Western Alps collisional belt). Journal of Metamorphic Geology, 5, 397-414.

Polino, R. and G. V. Dal Piaz, 1990: “Tectonic erosopn at the Adria margin and accretionary processes for the Cretaceous orogeny of the Alps.” Mémoires de la Societé Géologique de France 156: 345-367.

Pryer, L. L. 1993: Microstructures in feldspars from a major crustal thrust zone: the Grenville Front, Ontario, Canada. Journal of Structural Geology 15, 21-36.

Ramsay, J. G. 1967: Folding and Fracturing of rocks. McGraw Hill, London.

Ramsay, J. G. and Huber, M. I. 1983: The Techniques of Modern Structural Geology, volume 1: Strain Analysis. Academic press, New York.

Ramsay, J. G. and Wood, D. S. 1973: The geometric effects of volume change during deformation processes. Tectonophysics 16, 263-277.

Reddy, S. M., Kelley, S. P. and Wheeler, J.1996: A $^{40}Ar/^{39}Ar$ laser probe study of micas from the Sesia Zone, Italian Alps: implications for metamorphic and deformation histories. Journal of Metamorphic Geology 14, 493-508.

Reddy, S. M., Wheeler, J. and Cliff, R.A. 1999: The Geometry and timing of Orogenic Extension: An Example from the Western Italian Alps. Journal of Metamorphic Geology 17, 573-589.

Reddy, S. M., Wheeler, J., Butler, R. W. H., Gliff, R. A., Freeman, s., Inger, S., Pickles, C. and Kelley, S. P. 2003: Kinematic reworking and exhumation of the convergent Alpine orogen, Tectonophysics 365, 77-102.

Reinecke, T. 1991: Very-high pressure metamorphism and uplift of coesite-bearing metasediments from the Zermatt-Saas zone, Western Alps. European Journal of Mineralogy 3, 7-17.

Ridley, J., 1989: Structural and metamorphic history of a segment of the Sesia-Lanzo zone, and its bearing on the kinematics of Alpine deformation in the western Alps. In: Coward, M.P., Dietrich, D., Park, R. G. (Eds), Alpine Tectonics. Geological Society Special Publication, vol. 45, pp.189-201.

Ring, U. 1992: An Alpine kinematical analysis of the Penninic nappes east of the Lepontine dome: Implications for the evolution of the Central Alps. Tectonics 11, 1139-1158.

Ring, U. 1994: Late Alpine kinematics of the Aosta fault (northwestern Italian Alps). Neues Jahrbuch für Geologie Paläontologie Abhandlungen 434 - 442.

Ring, U. 1995: Horizontal contraction or horizontal extension? Heterogeneous late Eocene and early Oligocene general shearing during blueschist and greenschist facies metamorphism at the Pennine-Austroalpine boundary zone in the Western Alps the Western Alps. Geologische Rundschau 84(4): 843-859.

Ring, U. 1998: Exhumation of blue schists from Samos Island. Geological Society of Greece Bulletin 32, 97-104.

Ring, U. 1999: Volume loss, fluid flow, and coaxial vs non-coaxial deformation in retrograde, amphibolite-facies shear zones, northern Malawi, east-central Africa. Geological Society of America Bulletin 111, 123-142.

Ring, U. and Brandon, M. T. 1994: Ductile strain, mass loss, and exhumation of Franciscan rocks. Geological Society of America Abstracts with Programs, 26, A73.

Ring, U. and Brandon, M. T. 1999: Deformation and mass loss in the Franciscan subduction complex: Implications for exhumation processes in accretionary wedges, in Exhumation processes: Normal Faulting, Ductile Flow, and Erosion, edited by U. Ring et al., Geological Society of London Special Publication 154**,** 55-86.

Ring, U. and Merle, O. 1992: Forethrusting, backfolding, and lateral gravitational escape in the northern part of the Western Alps Monte-Rosa region. Geological Society of America Bulletin 104, 901-914.

Ring, U. and Reischmann, T. 2002: The weak and superfast Cretan detachment, Greece: exhumation at subduction rates in extruding wedges. Journal of Geological Society of London 159, 225-228.

Ring, U., Brandon, M. T., Willet, S.D. and Lister, G.S., 1999: Exhumation processes. In: Ring, U., Brandon, M. T., Lister, G.S., Willet, S.D. (Eds.), Exhumation processes: Normal Faulting, Ductile Flow and Erosion. Geological Society Special Publication, pp.1-27.

Ring, U., Ratschbacher, L., Frisch, W., Biehler, D. and Kralik, M. 1989: Kinematics of the Alpine plate margin: structural styles, strain and motion along the Penninic-Austroalpine boundary in the Swiss-Austrian Alps. Journal of Geological Society of London 146, 835-849.

Ring, U., Willner, A. P. and Lackmann, W. 2001b: Stacking of Nappes with different Pressure-Temperature paths: An Example from the Menderes Nappes of Western Turkey. American Journal of Science 301, 912-944.

Rubatto, D. and Hermann, J., 2001: Exhumation as fast as subduction? Geology, 29, 3-6.

Sandrone, R., Cadoppi, P., Sacchi, R. and Vialon, P., 1993: The Dora-Maria Massif. In J.F. von Raumer and F. Neubauer (eds.), „Pre-Mesozoic geology in the Alps". Springer, Berlin, 315-323.

Sartori, M., 1990: L´unité du Barrhorn (Zone Pennique, Valais, Suisse), un lien entre les Préalpes médianes rigides et leur socle paléozoique: Mémoires de Géologie (Lausanne), 6, 1-140.

Schertl, H. P., Schreyer, W., and Chopin, C., 1991: The pyrope-coesite rocks and their country-rocks and their country-rocks at Parigi, Dora Massif, Western Alps: Detailed petrography, mineral chemistry and PT path. Contribution to Mineralogy and Petrology, 108, 1-21.

Schmid, S. M. and Kissling, E. 2000: The arc of the western Alps in the high of geophysical data on deep crustal structure. Tectonics 19, 62-85.

Schmid, S. M., Pfiffner, O.A., Froitzheim, N., Schönborn, G. and Kissling, E., 1996: Geophysical-geological transect and tectonic evolution of the Swiss-Italian Alps. Tectonics, 15, 1036-1064.

Selverstone, J. 1985: Petrologic constraints on imbrication, metamorphism, and uplift in the SW Tauern window, Eastern Alps. Tectonics, 4, 687-704.

Selverstone, J. 1988: Evidence for east-west crustal extension in the Eastern Alps: implications for the unroofing history of the Tauern Window. Tectonics, 7, 87-105.

Simpson, C. and De Poar, D. G. 1993: Strain and Kinematic analysis in general shear zones. Journal of Structural Geology 15, 1-20.

Spiegel, C., Kuhlemann, J., Dunkl, I., Frisch, W., Eynatten, H. and Balogh, K. 2000: The erosion history of the Central Alps: evidence from zircon fission track data of the foreland basin sediments. Terra Nova, 12, 163-170.

Stampfli, G. M. 1993: Le Briançonnais, terrain exotique dans les Alpes? Eclogae Geologicae Helvetiae 86, 1, 1-45.

Stampfli, G. M. 2000: Tectonics and magmatism in Turkey and the surrounding area. Geological Society Special Publications.173; Pages 1-23.

Stampfli, G. M. and R. H. Marchant 1997: Geodynamic evolution of the Tethyan margins of the Western Alps. Results of NRP 20; deep structure of the Swiss Alps. O. A. Pfiffner, P. Lehner, P. Heitzman, S. Mueller and A. Steck: 223-239.

Stern, W. B. 1972: Zur röntgenspektrometrischen Analyse von silikatischen Gesteinen und Mineralien. Schweizerische Mineralogishche und Petrographishe Mitteilungen 52, 1-25.

Thompson, A. B., Schulmann, K. and Jezek, J. 1997: Extrusion tectonics and elevation of the lower crustal metamorphic rocks in convergent orogens. Geology, 25, 491-494.

Tilton, G. R., Schreye, R. W. and Schertl, H. P. 1991: Pb-Sr-Hd isotopic behaviour of deeply subducted rocks from the Dora Maira massif, Western Alps, Italy: What is the age of the ultrahigh pressure metamorphism? Contribution to Mineralogy and Petrology 108, 22-33.

Trümpy, R. 2001: Why plate tectonics was not invented in the Alps. International Journal of Earth Sciences, V 90, 3, 477-483.

Trümpy, R., 1980: Geology of Switzerland: A Guide Book. Wepf, Basel.

Vearncombe J.R. 1983: High-Pressure-low-temperature metamorphism in the Gran Paradiso basement, Western Alps. Journal of Metamorphic Geology 1, 103-115.

Vearncombe, J. R. 1985: The structure of the Gran Paradiso basement massif and its envelope, western Alps. Eclogae Geologicae Helvetiae 78, 49-72.

Vialon P. 1966: Etude gèologique du Massif Cristallin Dora Maria, Alpes cottiennes internes, Italie. PhD Thesis, Univ. Grenoble, Travaux du laboratoire de Gèologie de la Facultè des sciences de Grenoble, Memoir 4, 293p.

Vissers, R. L. M. and Compagnoni, R. 1984: The structure of the Gran Paradiso basement (Pennine Zone, Italian western Alps). Geologie en Mijnbouw 63, 89-92.

Voll, G. 1980: Ein Querprofil durch die Schweizer Alpen vom vierwaldstätter see zur Wurzelzone-strukturen und ihre Entwicklung durch Defomationsmechanismen wichtiger Minerale. Neues Jahrbuch für Geologie Paläontologie Abhandlungen 160, 321-335.

Vuichard J.P. and Ballèvre M. 1988: Garnet- chloritoid equilibria in eclogitic pelitic rocks from the Sesia Zone (Western Alps): their bearing on phase relations in high-pressure metapelites. Journal of Metamorphic Geology 6, 135-157.

Wallis, S. R. 1995: Vorticity analysis and recognition of ductile extension in the Sanbagawa belt, SW Japan. Journal of Structural Geology, 17(8), 1077-1093.

Wallis, S. R. 1992: Vorticity analysis in a metachert from the San-bagawa Belt, SW Japan. Journal of Structural Geology 14, 271-280.

Wallis, S., Platt, J. and Knott, S. 1993: Recognition of syn-convergence extension in accretionary wedges with examples from the Calabrian Arc and the Eastern Alps. American Journal of Science, 293, 463-494.

Westbrook, G. K. and Smith, M. J. 1983: Long décollements and mud volcanoes: evidence from the Barbados Ridge complex for the role of high pore-fluid pressure in the development of an accretionary complex. Geology, 11, 279-283.

Wetzel R. 1972: Zür Petrographie und Mineralogie der Furgg-Zone (Monte Rosa-Decke). Schweizerische Mineralogishche und Petrographishe Mitteilungen, 52, 161-236.

Wheeler, J. and Butler, R. W. H. 1993: Evidence for extension in the western Alpine orogen: the contact between the oceanic Piemonte and overlying continental Sesia units. Earth Planetary Science Letters 114, 113-129.

Willett, S. D., Beaumont, C. and Fullsack, P. 1993: Mechanical model for the tectonics of doubly vergent compressional orogens. Geology, 21, 371-374.

Zingg, A., Handy, M.R. Hunziker, J. C. and Schmid, S.M. 1990: Tectonometamorphic history of the Ivrea Zone and its relationship to the evolution of the Southern Alps. Tectonophysics 182, 169-192.

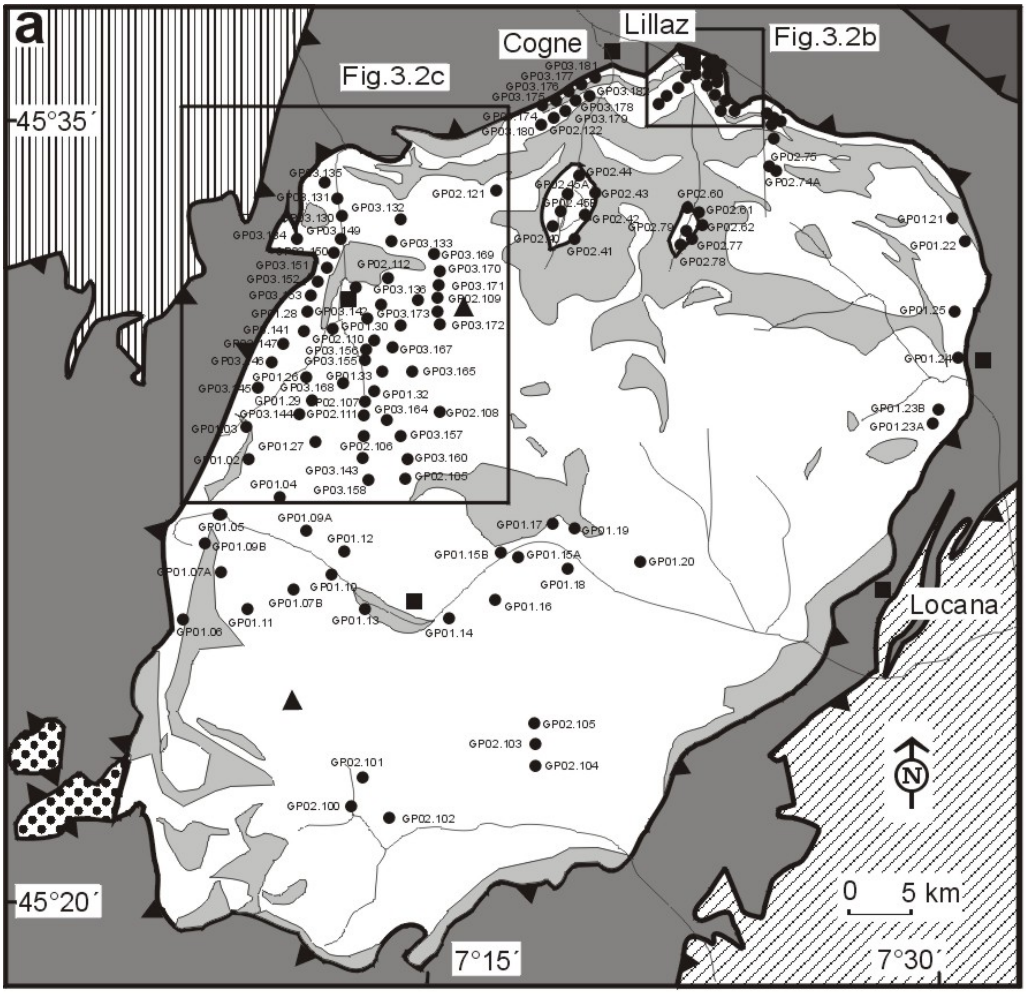
a
Cogne
Lillaz
Fig.3.2b
Fig.3.2c
45°35´
45°20´
7°15´
7°30´
Locana
0 5 km
b
Lillaz
0 5km

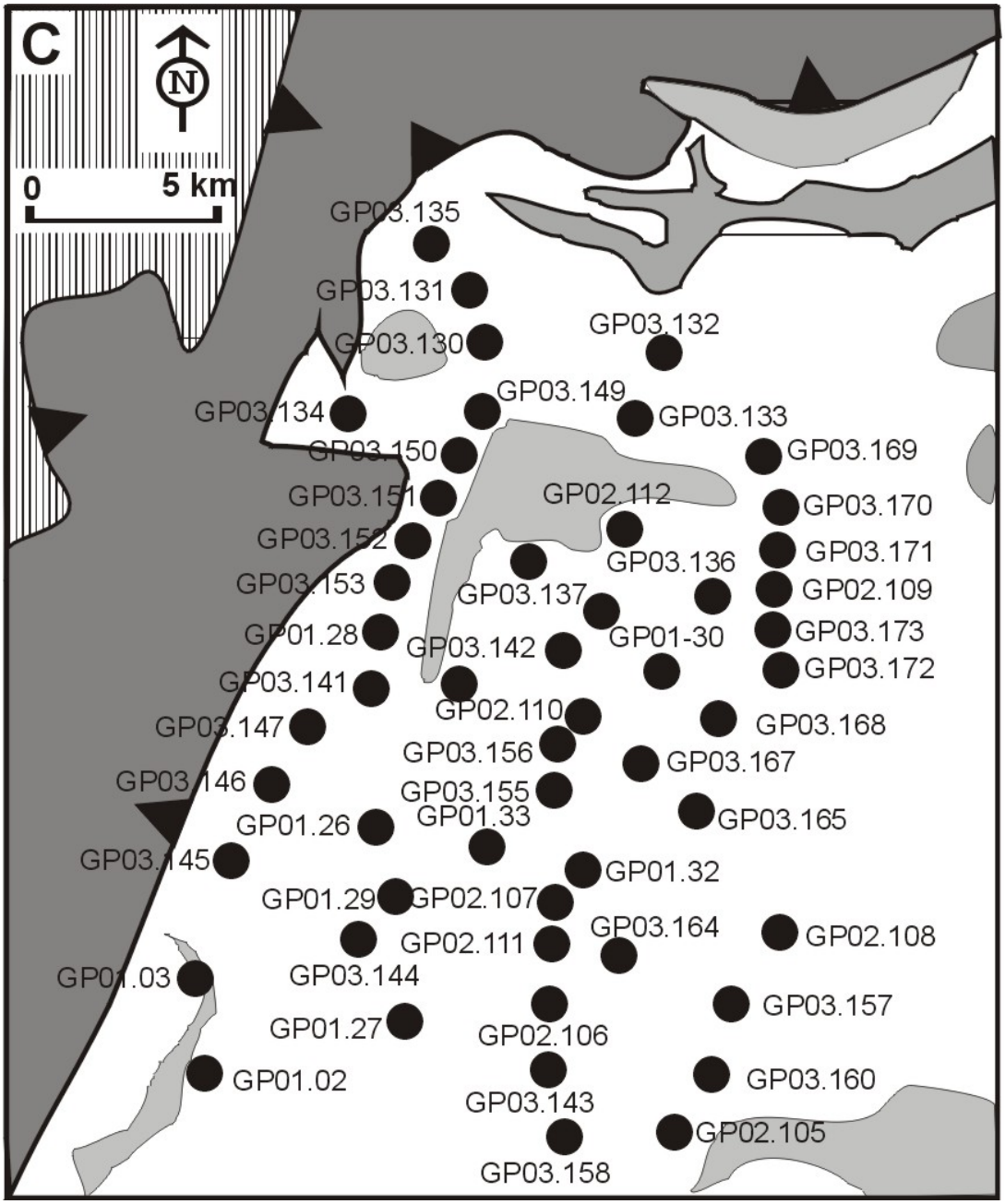

Fig.3.2: (a, b and c) Maps showing localities of finite-strain samples.

Table 3.1: Direction of finite strain axes and stretches for samples from Gran Paradiso massif.

Sample No.	Trend X	Plung X	Sx	Trend Y	Plung Y	Sy	Trend Z	Plung Z	S z
Gran Paradiso Unit									
Augen gneiss									
GP01-01	306	22	2.39	36	1	1.39	126	68	0.30
GP01-02	302	12	2.61	211	6	1.13	97	75	0.34
GP01-03	312	20	1.94	44	0	1.31	134	69	0.40
GP01-04	272	0	3.53	2	10	0.91	175	80	0.31
GP01-05	297	14	2.67	27	0	1.55	110	76	0.24
GP01-06	320	14	1.54	230	0	1.53	134	76	0.42
GP01-07A	282	7	3.50	13	4	1.03	135	82	0.28
GP01-07B	282	10	6.66	14	13	1.04	154	73	0.14
GP01-08	247	9	1.56	340	16	1.55	126	72	0.41
GP01-09A	57	2	3.79	328	24	1.53	150	65	0.17
GP01-09B	276	22	2.36	13	16	1.29	135	64	0.33
GP01-10	347	1	1.68	257	11	1.34	80	79	0.45
GP01-11	249	15	1.69	340	4	1.34	88	74	0.44
GP01-12	300	22	2.22	207	8	1.37	92	67	0.33
GP01-13	281	24	1.84	185	16	1.43	70	65	0.38
GP01-14	283	5	1.79	192	13	1.23	40	75	0.45
GP01-15A	76	15	2.20	170	12	0.99	292	70	0.46
GP01-15B	265	3	2.34	356	1	0.96	93	86	0.45
GP01-16	74	4	2.76	164	4	1.01	295	85	0.36
GP01-17	112	10	2.53	203	8	1.29	324	77	0.31
GP01-18	296	9	1.94	27	2	1.21	120	83	0.43
GP01-19	122	15	2.38	215	12	1.32	343	70	0.32
GP01-20	278	2	2.13	187	18	1.12	11	72	0.42
GP01-21	224	1	1.67	130	54	1.23	315	36	0.49
GP01-22	227	42	1.68	341	27	1.21	92	38	0.49
GP01-23A	311	47	1.44	118	42	1.27	214	6	0.54
GP01-23B	334	42	1.44	124	44	1.27	230	15	0.54
GP01-24	70	10	1.50	161	11	1.20	297	75	0.56
GP01-25	278	25	2.10	11	6	1.07	112	64	0.45
GP01-26	288	32	2.14	23	6	1.27	122	57	0.37
GP01-27	301	33	2.14	34	6	1.42	130	57	0.33
GP01-28	274	24	2.64	15	24	1.14	144	56	0.33
GP01-29	294	5	2.91	25	10	1.23	182	79	0.28
GP01-30	248	15	1.71	342	12	1.53	105	70	0.38
GP01-31	295	2	2.41	25	0	1.34	110	88	0.31
GP01-32	310	10	2.26	40	0	1.56	125	79	0.28
GP01-33	319	4	3.66	50	10	1.02	204	77	0.27
GP02-46	120	1	2.86	209	37	1.49	28	52	0.24
GP02-47	131	40	2.94	243	25	1.21	356	40	0.28
GP02-48	133	28	3.24	238	26	1.13	2	50	0.27

Table 3.1: continued

GP02-49A	128	15	4.21	227	25	1.12	10	60	0.21
GP02-49B	252	0	3.03	342	30	1.15	161	60	0.29
GP02-50	102	24	2.84	208	30	0.96	341	50	0.37
GP02-51	333	19	1.40	218	48	1.38	76	34	0.52
GP02-52	299	12	1.46	197	42	1.29	41	45	0.53
GP02-53	256	38	2.53	127	38	0.92	11	30	0.43
GP02-54	224	22	1.40	328	30	1.18	103	50	0.60
GP02-55	260	18	1.47	163	17	1.26	35	64	0.54
GP02-56	298	18	1.70	28	0	1.05	114	72	0.56
GP02-57	279	24	2.67	187	5	0.98	90	66	0.38
GP02-58	285	16	2.42	15	1	1.21	107	75	0.34
(Fry)			2.59			1.24			0.31
GP02-63	100	0	2.90	190	27	1.07	10	64	0.32
GP02-64	123	13	3.09	215	8	1.18	334	74	0.27
GP02-65A	260	10	2.33	166	21	1.31	12	68	0.33
GP02-65B	270	0	2.59	180	4	1.46	346	85	0.26
GP02-66	260	4	2.32	170	8	1.33	16	81	0.32
GP02-67	120	12	2.60	218	34	1.10	16	55	0.35
GP02-70A	125	11	2.96	217	10	1.42	350	75	0.24
GP02-70B	113	15	3.14	210	24	1.43	352	60	0.22
GP02-71	122	6	2.66	214	18	1.24	14	70	0.30
GP02-72	120	23	2.18	224	28	1.38	358	53	0.33
GP02-73	105	16	2.58	201	19	1.41	337	65	0.27
GP02-74A	249	12	1.40	158	9	1.24	26	77	0.58
GP02-74B	272	8	1.90	180	12	1.23	34	75	0.43
GP02-75	250	7	1.54	340	0	1.23	72	85	0.53
GP02-80A	120	30	2.01	228	29	1.29	353	47	0.39
GP02-80B	258	6	2.35	165	24	1.17	2	66	0.36
GP02-81	90	0	3.12	180	44	1.38	359	46	0.23
GP02-82	125	7	2.32	35	2	1.15	288	83	0.37
GP02-83	128	17	3.03	231	38	1.26	18	48	0.26
GP02-84A	95	0	2.36	185	3	1.26	359	87	0.34
(Fry)			2.02			1.26			0.39
GP02-84B	253	0	2.79	163	21	1.12	347	68	0.32
GP02-85	90	0	2.10	181	21	1.45	357	69	0.33
(Fry)			1.75			1.40			0.41
GP02-86A	275	2	2.08	185	10	1.30	15	81	0.37
GP02-86B	305	2	2.43	214	18	1.14	38	71	0.36
GP02-100	141	11	1.90	47	19	1.22	258	67	0.43
GP02-101	248	6	1.78	338	5	1.33	106	82	0.42
GP02-102	283	2	2.58	12	1	1.03	114	88	0.38
GP02-103	88	17	3.05	180	6	0.94	288	72	0.35
GP02-104	82	14	4.27	176	14	0.77	309	70	0.30

Table 3.1: continued

GP02-105	80	16	2.32	174	15	1.07	304	67	0.40
GP02-106	280	3	8.08	10	0	1.07	98	87	0.12
GP02-107	273	4	3.41	4	1	1.21	108	86	0.24
GP02-108	289	4	2.11	19	1	1.13	108	86	0.42
GP02-109	272	14	3.09	181	3	0.96	87	76	0.34
GP02-110	280	8	5.09	189	3	1.15	84	82	0.17
GP02-111	280	11	3.98	10	1	1.15	105	78	0.22
GP02-112	270	4	1.47	180	1	1.12	79	86	0.61
GP02-113	82	8	2.30	172	4	0.94	280	81	0.46
GP02-118	278	2	1.34	8	3	1.17	157	87	0.64
GP02-119	271	7	2.14	8	42	1.46	173	49	0.32
GP02-120	258	3	2.87	347	2	1.21	83	87	0.29
GP02-121	274	16	2.35	25	50	1.25	172	37	0.34
GP02-122	283	18	2.75	28	40	1.15	173	45	0.32
GP03-130	278	2	5.32	9	24	0.85	180	66	0.22
GP03-131	86	0	2.57	356	29	1.08	176	60	0.36
GP03-132	264	12	1.92	6	42	1.30	162	46	0.40
GP03-133	242	22	2.38	339	17	1.19	100	60	0.35
GP03-134	270	22	2.87	12	29	1.20	147	53	0.29
GP03-135	278	24	2.80	21	26	1.13	152	53	0.32
GP03-136	293	30	2.49	199	7	1.17	98	60	0.34
GP03-137	278	22	2.56	12	10	1.19	122	64	0.33
GP03-138	272	12	2.71	182	4	1.02	82	79	0.36
GP03-139	266	7	4.97	356	0	1.00	90	83	0.20
GP03-140	275	10	3.53	6	4	0.91	111	80	0.31
GP03-141	268	9	2.88	358	2	0.93	92	81	0.37
GP03-142	283	15	3.91	14	4	0.80	113	75	0.32
GP03-143	262	9	8.95	350	6	0.72	111	79	0.15
GP03-144	305	21	2.99	212	9	1.11	99	67	0.30
GP03-145	295	20	9.62	201	11	0.57	86	67	0.18
GP03-146	305	28	3.93	212	6	1.47	113	62	0.17
GP03-147	298	19	4.87	30	6	0.90	138	71	0.23
GP03-148	292	9	3.63	22	1	1.05	108	81	0.26
GP03-149	300	18	3.05	30	0	1.27	120	71	0.26
GP03-150	290	18	3.22	21	2	0.96	115	72	0.32
GP03-151	300	18	2.65	33	10	1.11	146	68	0.34
GP03-152	282	32	3.42	23	19	1.25	138	53	0.23
GP03-153	290	24	4.21	25	12	1.09	139	62	0.22
GP03-154	305	26	2.76	36	2	1.09	129	63	0.33
GP03-155	284	32	4.57	30	25	1.12	151	49	0.20
GP03-156	287	30	4.13	20	6	0.94	119	59	0.26
GP03-157	290	11	6.69	200	4	0.95	90	78	0.16
GP03-158	279	15	3.08	10	4	1.01	112	75	0.32

Table 3.1: continued

GP03-159	284	16	3.84	18	16	1.08	152	67	0.24
GP03-160	276	5	5.91	7	3	0.78	113	84	0.22
GP03-164	292	20	4.79	25	8	0.96	136	68	0.22
GP03-165	281	5	2.83	11	0	1.16	90	85	0.31
GP03-166	280	2	1.60	190	0	1.22	90	88	0.51
GP03-167	283	14	4.21	14	3	1.11	110	76	0.21
GP03-168	275	12	3.36	5	0	0.86	96	78	0.35
GP03-169	285	22	2.87	22	17	1.02	146	61	0.34
GP03-170	283	19	2.56	18	14	1.07	141	65	0.37
GP03-171	287	11	2.81	18	9	0.95	145	76	0.37
GP03-172	283	18	2.63	17	14	1.65	139	67	0.23
GP03-173	279	21	3.08	15	14	0.92	133	64	0.35
GP03-174	287	20	3.83	33	38	0.98	175	46	0.27
GP03-175	296	19	3.28	33	21	1.15	167	60	0.26
GP03-176	284	21	3.54	24	25	1.07	159	57	0.26
GP03-177	274	0	3.33	5	47	1.23	184	43	0.24
GP03-178	275	0	3.46	5	41	1.10	184	49	0.26
GP03-179	260	10	7.15	353	17	0.86	138	70	0.16
GP03-180	276	14	2.68	12	22	1.01	154	62	0.37
GP03-181	70	20	3.20	332	22	1.05	198	60	0.30
GP03-182	77	7	4.69	342	41	0.85	175	49	0.25
tensor average	**278**	**9**	**2.29**	**8**	**3**	**1.05**	**114**	**81**	**0.42**
Conglomerate									
GP02-114	97	6	2.30	6	8	1.31	225	79	0.33
(Fry)			2.08			1.46			0.33
GP02-115	100	1	2.60	10	8	1.33	207	81	0.29
(Fry)			2.71			1.17			0.32
GP02-116	83	2	2.84	353	7	1.03	190	83	0.34
(Fry)			2.69			1.15			0.32
GP02-117	97	8	1.98	7	2	1.61	267	83	0.31
(Fry)			1.69			1.54			0.38
GP03-183	77	20	3.34	339	21	0.99	208	60	0.30
GP03-184	74	11	2.88	343	7	1.47	221	77	0.24
GP03-185	80	11	2.78	348	10	1.14	216	75	0.32
GP03-186	72	11	3.07	340	10	1.38	210	75	0.24
GP03-187	79	14	2.66	346	15	1.37	211	70	0.28
GP03-188	81	4	2.60	351	6	1.50	198	83	0.26
GP03-189	72	5	2.42	342	8	1.24	191	80	0.33
tensor average	**81**	**9**	**2.61**	**349**	**10**	**1.29**	**212**	**77**	**0.30**

Table 3.1: continued

Efaulet Unit									
Conglomerate									
GP02-41	91	3	3.69	360	11	0.80	198	78	0.34
GP02-42	282	10	3.57	12	1	0.97	104	80	0.29
GP02-43	99	18	3.73	193	11	0.82	310	69	0.33
Erfaulet granite									
GP02-44	84	5	1.82	182	66	1.16	352	24	0.48
GP02-45A	99	0	2.94	8	16	0.85	190	74	0.40
GP02-45B	105	24	2.47	8	16	0.97	247	62	0.42
GP02-60	282	1	3.36	191	10	0.87	13	81	0.34
GP02-61	284	26	2.75	188	11	1.03	78	61	0.35
GP02-62	298	24	2.22	196	25	0.99	66	55	0.46
GP02-77	277	12	3.32	183	20	0.91	35	68	0.33
GP02-78	103	8	3.19	196	20	0.93	353	70	0.34
GP02-79	119	7	2.87	28	2	1.00	279	82	0.35
tensor average	**282**	**1**	**2.52**	**192**	**8**	**0.87**	**15**	**82**	**0.46**
Mica Schist									
GP02-40	281	9	3.82	12	4	0.96	49	80	0.27
(Fry)			3.03			0.96			0.34
total tensor	**278**	**8**	**2.28**	**8**	**3**	**1.06**	**118**	**82**	**0.42**

Table 3.2: Finite strain data for sample from Gran Paradiso massif.

Sample No.	Long.	Lat.	Method	Rxy	Ryz	Rxz	K	Et
Gran Paradiso Unit								
Augen gneiss								
GP01-01	7°08′52′′	45°27′45′′	Rf/ϕ	1.72	4.63	7.94	0.20	1.52
GP01-02	7°08′25′′	45°28′50′′	Rf/ϕ	2.30	3.36	7.71	0.55	1.45
GP01-03	7°08′38′′	45°28′36′′	Rf/ϕ	1.48	3.30	4.89	0.21	1.17
GP01-04	7°08′31′′	45°28′22′′	Rf/ϕ	3.86	2.96	11.43	1.46	1.73
GP01-05	7°08′33′′	45°28′15′′	Rf/ϕ	1.73	6.37	10.99	0.14	1.78
GP01-06	7°07′53′′	45°27′50′′	Rf/ϕ	1.01	3.61	3.63	0.00	1.05
GP01-07A	7°08′11′′	45°27′54′′	Rf/ϕ	3.41	3.70	12.59	0.89	1.79
GP01-07B	7°08′12′′	45°27′55′′	Rf/ϕ	6.38	7.27	46.34	0.86	2.71
GP01-08	7°08′39′′	45°27′51′′	Rf/ϕ	1.01	3.73	3.76	0.00	1.08
GP01-09A	7°08′56′′	45°27′42′′	Rf/ϕ	2.47	8.91	22.00	0.19	2.25
GP01-09B	7°08′54′′	45°27′40′′	Rf/ϕ	1.82	3.96	7.22	0.28	1.43
GP01-10	7°09′44′′	45°27′32′′	Rf/ϕ	1.26	3.00	3.77	0.13	1.00
GP01-11	7°10′56′′	45°27′08′′	Rf/ϕ	1.26	3.05	3.84	0.13	1.02
GP01-12	7°11′34′′	45°27′04′′	Rf/ϕ	1.62	4.17	6.73	0.19	1.40
GP01-13	7°12′20′′	45°26′36′′	Rf/ϕ	1.28	3.77	4.83	0.10	1.20
GP01-14	7°15′07′′	45°25′55′′	Rf/ϕ	1.45	2.71	3.94	0.27	1.00
GP01-15A	7°16′35′′	45°26′36′′	Rf/ϕ	2.22	2.15	4.77	1.06	1.10
GP01-15B	7°16′37′′	45°26′37′′	Rf/ϕ	2.45	2.13	5.23	1.28	1.17
GP01-16	7°16′29′′	45°26′32′′	Rf/ϕ	2.74	2.79	7.65	0.97	1.44
GP01-17	7°18′07′′	45°27′23′′	Rf/ϕ	1.96	4.22	8.26	0.30	1.53
GP01-18	7°17′51′′	45°27′18′′	Rf/ϕ	1.60	2.86	4.56	0.32	1.10
GP01-19	7°18′39′′	45°27′21′′	Rf/ϕ	1.80	4.17	7.50	0.25	1.47
GP01-20	7°19′28′′	45°27′00′′	Rf/ϕ	1.89	2.68	5.07	0.53	1.16
GP01-21	7°31′18′′	45°32′53′′	Rf/ϕ	1.36	2.51	3.41	0.24	0.90
GP01-22	7°31′30′′	45°32′43′′	Rf/ϕ	1.39	2.47	3.43	0.26	0.90
GP01-23A	7°30′22′′	45°28′48′′	Rf/ϕ	1.13	2.34	2.65	0.10	0.75
GP01-23B	7°30′23′′	45°28′49′′	Rf/ϕ	1.13	2.34	2.65	0.10	0.75
GP01-24	7°30′46′′	45°30′06′′	Rf/ϕ	1.25	2.15	2.69	0.22	0.73
GP01-25	7°30′48′′	45°30′08′′	Rf/ϕ	1.96	2.38	4.66	0.70	1.09
GP01-26	7°10′43′′	45°31′26′′	Rf/ϕ	1.68	3.48	5.83	0.27	1.28
GP01-27	7°10′47′′	45°31′22′′	Rf/ϕ	1.50	4.33	6.51	0.15	1.39
GP01-28	7°11′13′′	45°31′29′′	Rf/ϕ	2.31	3.46	7.99	0.53	1.48
GP01-29	7°11′17′′	45°31′32′′	Rf/ϕ	2.37	4.38	10.38	0.41	1.67
GP01-30	7°11′35′′	45°31′30′′	Rf/ϕ	1.12	4.02	4.50	0.04	1.18
GP01-31	7°13′25′′	45°30′55′′	Rf/ϕ	1.80	4.33	7.80	0.24	1.50
GP01-32	7°13′06′′	45°31′18′′	Rf/ϕ	1.45	5.52	8.00	0.10	1.57
GP01-33	7°13′05′′	45°31′10′′	Rf/ϕ	3.58	3.82	13.65	0.42	1.85

Table 3.2: Continued

GP02-46	7°23′41′′	45°35′41′′	Rf/ϕ	1.92	6.32	12.16	0.17	1.83
GP02-47	7°23′43′′	45°35′43′′	Rf/ϕ	2.43	4.32	10.49	0.43	1.68
GP02-48	7°23′42′′	45°35′42′′	Rf/ϕ	2.87	4.16	11.91	0.59	1.76
GP02-49A	7°23′44′′	45°35′44′′	Rf/ϕ	3.78	5.25	19.82	0.65	2.12
GP02-49B	7°23′46′′	45°35′45′′	Rf/ϕ	2.64	3.97	10.50	0.55	1.67
GP02-50	7°23′10′′	45°35′25′′	Rf/ϕ	2.95	2.62	7.73	1.21	1.45
GP02-51	7°23′20′′	45°35′23′′	Rf/ϕ	1.01	2.69	2.72	0.01	0.81
GP02-52	7°23′21′′	45°35′22′′	Rf/ϕ	1.13	2.43	2.74	0.09	0.78
GP02-53	7°23′19′′	45°35′25′′	Rf/ϕ	2.75	2.13	5.86	1.55	1.25
GP02-54	7°23′30′′	45°35′28′′	Rf/ϕ	1.19	1.96	2.33	0.19	0.63
GP02-55	7°23′31′′	45°35′29′′	Rf/ϕ	1.17	2.34	2.73	0.12	0.77
GP02-56	7°23′32′′	45°35′30′′	Rf/ϕ	1.62	1.88	3.05	0.71	0.79
GP02-57	7°23′33′′	45°35′31′′	Rf/ϕ	2.73	2.56	6.98	1.11	1.38
GP02-58	7°23′34′′	45°35′28′′	Rf/ϕ	2.01	3.52	7.07	0.40	1.40
			Fry	2.08	4.00	8.33	0.36	2.00
GP02-63	7°23′53′′	45°35′24′′	Rf/ϕ	2.71	3.30	8.96	0.75	1.55
GP02-64	7°24′00′′	45°35′13′′	Rf/ϕ	2.61	4.32	11.29	0.49	1.73
GP02-65A	7°24′06′′	45°35′09′′	Rf/ϕ	1.78	3.99	7.11	0.26	1.43
GP02-65B	7°23′55′′	45°35′38′′	Rf/ϕ	1.78	5.51	9.81	0.17	1.68
GP02-66	7°23′46′′	45°35′47′′	Rf/ϕ	1.75	4.12	7.20	0.24	1.44
GP02-67	7°23′43′′	45°35′43′′	Rf/ϕ	2.35	3.17	7.45	0.62	1.43
GP02-70A	7°25′31′′	45°34′53′′	Rf/ϕ	2.08	6.00	12.50	0.22	1.84
GP02-70B	7°25′33′′	45°34′55′′	Rf/ϕ	2.20	6.44	14.15	0.22	1.92
GP02-71	7°25′34′′	45°34′51′′	Rf/ϕ	2.14	4.12	8.82	0.36	1.56
GP02-72	7°25′36′′	45°34′52′′	Rf/ϕ	1.59	4.13	6.56	0.19	1.39
GP02-73	7°25′30′′	45°34′40′′	Rf/ϕ	1.82	5.15	9.38	0.20	1.64
GP02-74A	7°25′32′′	45°34′10′′	Rf/ϕ	1.13	2.15	2.42	0.11	0.68
GP02-74B	7°25′30′′	45°34′08′′	Rf/ϕ	1.54	2.89	4.45	0.29	1.09
GP02-75	7°25′32′′	45°34′10′′	Rf/ϕ	1.25	2.32	2.90	0.19	0.80
GP02-80A	7°22′58′′	45°35′40′′	Rf/ϕ	1.56	3.34	5.21	0.24	1.21
GP02-80B	7°22′56′′	45°35′41′′	Rf/ϕ	2.00	3.22	6.46	0.45	1.33
GP02-81	7°22′57′′	45°35′32′′	Rf/ϕ	2.27	5.90	13.37	0.26	1.88
GP02-82	7°22′57′′	45°35′12′′	Rf/ϕ	2.01	3.09	6.22	0.48	1.30
GP02-83	7°22′44′′	45°35′33′′	Rf/ϕ	2.39	4.84	11.58	0.36	1.76
GP02-84A	7°22′38′′	45°35′46′′	Rf/ϕ	1.88	3.73	7.00	0.32	1.40
			Fry	1.61	3.20	5.14	0.28	1.00
GP02-84B	7°22′40′′	45°35′48′′	Rf/ϕ	2.48	3.52	8.73	0.59	1.54
GP02-85	7°22′40′′	45°35′47′′	Rf/ϕ	1.45	4.44	6.43	0.13	1.39
			Fry	1.25	3.43	4.29	0.10	1.00
GP02-86A	7°23′38′′	45°35′42′′	Rf/ϕ	1.60	3.52	5.65	0.24	1.27

Table 3.2: Continued

GP02-86B	7°23′39′′	45°35′44′′	Rf/ϕ	2.14	3.16	6.74	0.53	1.36
GP02-100	7°12′14′′	45°22′16′′	Rf/ϕ	1.57	2.82	4.41	0.31	0.19
GP02-101	7°12′33′′	45°22′13′′	Rf/ϕ	1.34	3.18	4.25	0.15	1.08
GP02-102	7°12′40′′	45°22′08′′	Rf/ϕ	2.50	2.75	6.89	0.86	1.37
GP02-103	7°16′29′′	45°23′08′′	Rf/ϕ	3.25	2.67	8.68	1.35	1.53
GP02-104	7°16′30′′	45°23′10′′	Rf/ϕ	5.53	2.55	14.11	2.92	1.90
GP02-105	7°16′31′′	45°23′11′′	Rf/ϕ	2.18	2.63	5.73	0.72	1.24
GP02-106	7°12′21′′	45°30′23′′	Rf/ϕ	7.55	9.25	69.81	0.79	3.00
GP02-107	7°12′05′′	45°31′45′′	Rf/ϕ	2.81	5.40	14.14	0.45	1.89
GP02-108	7°14′20′′	45°30′05′′	Rf/ϕ	1.87	2.69	5.03	0.51	1.15
GP02-109	7°14′30′′	45°31′30′′	Rf/ϕ	3.23	2.83	9.14	1.22	1.57
GP02-110	7°13′02′′	45°31′07′′	Rf/ϕ	4.44	6.70	29.74	0.60	2.41
GP02-111	7°13′12′′	45°30′40′′	Rf/ϕ	3.46	5.26	18.18	0.58	2.06
GP02-112	7°12′45′′	45°31′50′′	Rf/ϕ	1.31	1.84	2.41	0.38	0.64
GP02-113	7°23′33′′	45°35′28′′	Rf/ϕ	2.45	2.03	4.99	1.41	1.14
GP02-118	7°23′28′′	45°35′29′′	Rf/ϕ	1.14	1.85	2.10	0.16	0.56
GP02-119	7°23′30′′	45°35′30′′	Rf/ϕ	1.46	4.58	6.71	0.13	1.43
GP02-120	7°23′20′′	45°35′25′′	Rf/ϕ	2.38	4.19	9.94	0.43	1.64
GP02-121	7°23′25′′	45°35′27′′	Rf/ϕ	1.89	3.66	6.91	0.33	1.39
GP02-122	7°23′20′′	45°35′25′′	Rf/ϕ	2.39	3.63	8.70	0.53	1.54
GP03-130	7°12′01′′	45°34′01′′	Rf/ϕ	6.29	3.80	23.90	1.89	2.25
GP03-131	7°11′53′′	45°33′52′′	Rf/ϕ	2.37	3.02	7.15	0.68	1.40
GP03-132	7°12′33′′	45°33′40′′	Rf/ϕ	1.47	3.25	4.78	0.21	1.15
GP03-133	7°12′40′′	45°33′32′′	Rf/ϕ	1.99	3.38	6.73	0.42	1.37
GP03-134	7°10′53′′	45°33′39′′	Rf/ϕ	2.38	4.15	9.89	0.44	1.64
GP03-135	7°12′25′′	45°34′00′′	Rf/ϕ	2.48	3.59	8.90	0.57	1.55
GP03-136	7°12′42′′	45°32′36′′	Rf/ϕ	2.12	3.42	7.26	0.46	1.42
GP03-137	7°13′13′′	45°32′42′′	Rf/ϕ	2.16	3.61	7.80	0.44	1.47
GP03-138	7°12′42′′	45°32′44′′	Rf/ϕ	2.65	2.82	7.48	0.91	1.42
GP03-139	7°11′49′′	45°32′33′′	Rf/ϕ	4.99	4.94	24.65	1.01	2.27
GP03-140	7°12′29′′	45°32′07′′	Rf/ϕ	3.87	2.94	11.38	1.48	1.72
GP03-141	7°11′28′′	45°31′57′′	Rf/ϕ	3.09	2.51	7.75	1.38	1.45
GP03-142	7°12′00′′	45°31′56′′	Rf/ϕ	4.85	2.53	12.28	2.52	1.79
GP03-143	7°12′01′′	45°28′55′′	Rf/ϕ	12.35	4.69	57.94	3.08	2.90
GP03-144	7°10′24′′	45°30′34′′	Rf/ϕ	2.70	3.65	9.86	0.64	1.62
GP03-145	7°10′23′′	45°30′56′′	Rf/ϕ	16.97	3.09	52.45	7.64	2.89
GP03-146	7°10′53′′	45°31′36′′	Rf/ϕ	2.67	8.49	22.66	0.22	2.26
GP03-147	7°11′31′′	45°31′55′′	Rf/ϕ	5.43	3.93	21.33	1.51	2.17
GP03-148	7°11′41′′	45°02′13′′	Rf/ϕ	3.45	4.03	13.91	0.81	1.86
GP03-149	7°11′57′′	45°32′43′′	Rf/ϕ	2.40	4.93	11.83	0.36	1.77

Table 3.2: Continued

GP03-150	7°12´17´´	45°32´42´´	Rf/ϕ	3.34	2.99	9.98	1.17	1.63
GP03-151	7°12´15´´	45°32´34´´	Rf/ϕ	2.38	3.29	7.82	0.60	1.46
GP03-152	7°12´20´´	45°32´19´´	Rf/ϕ	2.74	5.35	14.64	0.40	1.92
GP03-153	7°12´07´´	45°02´02´´	Rf/ϕ	3.86	5.03	19.40	0.71	2.10
GP03-154	7°12´00´´	45°02´00´´	Rf/ϕ	2.54	3.26	8.27	0.68	1.50
GP03-155	7°11´58´´	45°31´37´´	Rf/ϕ	4.09	5.71	23.33	0.66	2.23
GP03-156	7°12´06´´	45°31´44´´	Rf/ϕ	4.40	3.64	16.03	1.29	1.96
GP03-157	7°12´25´´	45°29´42´´	Rf/ϕ	7.02	6.06	42.50	1.19	2.65
GP03-158	7°12´19´´	45°29´18´´	Rf/ϕ	3.06	3.12	9.54	0.97	1.60
GP03-159	7°12´ 07´´	45°30´ 08´´	Rf/ϕ	3.54	4.51	15.95	0.72	1.96
GP03-160	7°13´05´´	45°29´07´´	Rf/ϕ	7.53	3.64	27.41	2.47	2.36
GP03-164	7°12´13´´	45°30´15´´	Rf/ϕ	5.00	4.40	21.98	1.18	2.19
GP03-165	7°12´34´´	45°30´13´´	Rf/ϕ	2.45	3.78	9.25	0.52	1.58
GP03-166	7°12´22´´	45°30´26´´	Rf/ϕ	1.32	2.37	3.13	0.23	0.84
GP03-167	7°12´04´´	45°31´36´´	Rf/ϕ	3.79	5.17	19.61	0.67	2.11
GP03-168	7°12´27´´	45°31´38´´	Rf/ϕ	3.92	2.47	9.68	1.99	1.62
GP03-169	7°15´03´´	45°32´46´´	Rf/ϕ	2.81	2.99	8.40	0.91	1.51
GP03-170	7°15´08´´	45°32´42´´	Rf/ϕ	2.39	2.92	6.98	0.72	1.38
GP03-171	7°15´02´´	45°32´41´´	Rf/ϕ	2.95	2.56	7.54	1.25	1.43
GP03-172	7°14´50´´	45°32´36´´	Rf/ϕ	1.59	7.18	11.41	0.10	1.83
GP03-173	7°14´06´´	45°32´33´´	Rf/ϕ	3.35	2.62	8.77	1.45	1.54
GP03-174	7°17´54´´	45°34´42´´	Rf/ϕ	3.93	3.64	14.29	1.11	1.88
GP03-175	7°17´52´´	45°34´41´´	Rf/ϕ	2.85	4.35	12.40	0.55	1.79
GP03-176	7°18´07´´	45°34´42´´	Rf/ϕ	3.31	4.05	13.42	0.76	1.84
GP03-177	7°18´26´´	45°34´23´´	Rf/ϕ	2.71	5.04	13.64	0.42	1.87
GP03-178	7°18´25´´	45°34´27´´	Rf/ϕ	3.15	4.17	13.13	0.68	1.82
GP03-179	7°18´35´´	45°34´23´´	Rf/ϕ	8.31	5.29	43.95	1.70	2.68
GP03-180	7°18´35´´	45°34´23´´	Rf/ϕ	2.66	2.71	7.21	0.97	1.40
GP03-181	7°19´07´´	45°34´53´´	Rf/ϕ	3.06	3.49	10.67	0.83	1.68
GP03-182	7°19´34´´	45°34´58´´	Rf/ϕ	5.50	3.41	18.75	1.87	2.08
tensor average				**2.74**	**3.79**	**10.98**	**0.68**	**1.53**
<u>Conglomerate</u>								
GP02-114	7°23´44´´	45°35´30´´	Rf/ϕ	1.76	3.95	6.95	0.26	1.41
			Fry	1.43	4.44	6.33	0.12	1.39
GP02-115	7°23´42´´	45°35´33´´	Rf/ϕ	1.96	4.61	9.01	0.26	1.59
			Fry	2.32	3.70	8.57	0.49	1.53
GP02-116	7°23´40´´	45°35´31´´	Rf/ϕ	2.75	3.03	8.34	0.86	1.50
			Fry	2.34	3.56	8.33	0.52	1.51
GP02-117	7°23´43´´	45°35´28´´	Rf/ϕ	1.23	5.16	6.34	0.05	1.00
			Fry	1.10	4.00	4.40	0.03	1.17

Table 3.2: Continued

GP03-183	7°23´47´´	45°35´40´´	Rf/ϕ	3.39	3.25	11.02	1.06	1.70
GP03-184	7°23´46´´	45°35´40´´	Rf/ϕ	1.96	6.18	12.12	0.19	1.83
GP03-185	7°23´49´´	45°35´43´´	Rf/ϕ	2.44	3.62	8.83	0.55	1.55
GP03-186	7°23´48´´	45°35´42´´	Rf/ϕ	2.22	5.89	13.06	0.25	1.86
GP03-187	7°23´46´´	45°35´40´´	Rf/ϕ	1.95	4.97	9.67	0.24	1.65
GP03-188	7°23´47´´	45°35´39´´	Rf/ϕ	1.73	5.86	10.12	0.15	1.71
GP03-189	7°24´01´´	45°35´36´´	Rf/ϕ	1.96	3.70	7.26	0.36	1.43
tensor average				**2.04**	**4.39**	**8.69**	**0.36**	**1.52**
Efaulet Unit								
Conglomerate								
GP02-41	7°19´40´´	45°32´57´´	Rf/ϕ	4.63	2.35	10.87	2.70	1.71
GP02-42	7°19´41´´	45°32´55´´	Rf/ϕ	3.69	3.34	12.32	1.15	1.78
GP02-43	7°19´38´´	45°32´59´´	Rf/ϕ	4.53	2.52	11.44	2.32	1.74
Erfaulet granite								
GP02-44	7°19´45´´	45°33´24´´	Rf/ϕ	1.57	2.43	3.83	0.40	0.97
GP02-45A	7°19´46´´	45°33´23´´	Rf/ϕ	3.44	2.14	7.36	2.14	1.43
GP02-45B	7°19´48´´	45°33´20´´	Rf/ϕ	2.55	2.32	5.92	1.18	1.26
GP02-60	7°22´52´´	45°33´07´´	Rf/ϕ	3.87	2.54	9.84	1.86	1.63
GP02-61	7°22´54´´	45°33´09´´	Rf/ϕ	2.68	2.89	7.77	0.89	1.45
GP02-62	7°23´02´´	45°32´49´´	Rf/ϕ	2.25	2.16	4.86	1.07	1.12
GP02-77	7°23´02´´	45°32´59´´	Rf/ϕ	3.64	2.75	10.02	1.50	1.63
GP02-78	7°23´09´´	45°32´47´´	Rf/ϕ	3.42	2.77	9.49	1.37	1.59
GP02-79	7°23´10´´	45°32´49´´	Rf/ϕ	2.86	2.88	8.23	0.99	1.49
tensor average				**3.26**	**2.59**	**8.50**	**1.46**	**1.48**
Mica Schist								
GP02-40	7°19´33´´	45°32´32´´	Rf/ϕ	3.99	3.51	13.99	1.19	1.87
			Fry	3.14	2.82	8.85	1.17	1.54
tensor average				**3.57**	**3.17**	**11.42**	**1.18**	**1.71**
Average all samples				**2.73**	**3.75**	**10.62**	**0.71**	**1.53**

Table 3.3: Representative microprobe analyses of white micas from the analyzed samples from Gran Paradiso unit.

Sample 65

Comment	pheng.	pheng.	pheng.	pheng.	pheng.	pheng.	pheng.	pheng.	pheng.	pheng.	pheng.	pheng.	pheng.
No.	**1**	**2**	**3**	**4**	**5**	**6**	**7**	**8**	**9**	**10**	**11**	**12**	**13**
SiO2	51.97	52.46	52.39	49.07	51.86	51.85	51.78	52.50	53.03	51.35	50.90	52.93	50.95
Al2O3	24.40	24.18	24.96	27.12	25.34	25.30	24.02	24.62	23.82	24.49	25.57	23.65	23.97
TiO2	0.25	0.13	0.15	0.20	0.21	0.26	0.63	0.17	0.14	0.42	0.34	0.12	0.13
Cr2O3	0.05	0.00	0.07	0.06	0.04	0.04	0.02	0.00	0.06	0.00	0.03	0.04	0.03
MgO	2.40	2.13	2.19	2.13	2.15	2.11	2.47	2.19	2.12	2.41	2.51	2.09	2.26
FeO	6.68	6.45	6.33	6.08	6.19	6.27	6.92	6.61	6.96	7.33	6.73	6.80	7.43
MnO	0.04	0.06	0.13	0.12	0.14	0.15	0.06	0.19	0.25	0.09	0.13	0.26	0.27
CaO	0.00	0.05	0.00	0.00	0.00	0.00	0.01	0.04	0.01	0.02	0.00	0.02	0.06
BaO	0.00	0.02	0.14	0.00	0.00	0.14	0.09	0.00	0.04	0.04	0.00	0.00	0.00
Na2O	0.02	0.04	0.06	0.10	0.05	0.03	0.02	0.03	0.01	0.01	0.07	0.01	0.01
K2O	10.15	10.00	9.94	10.46	10.08	10.31	10.23	10.12	10.32	10.40	10.44	10.21	10.17
Cl	0.00	0.01	0.01	0.00	0.00	0.00	0.01	0.01	0.02	0.01	0.01	0.02	0.03
F	0.42	0.00	0.43	0.12	0.33	0.26	0.17	0.33	0.47	0.32	0.23	0.27	0.24
	96.38	95.53	96.80	95.47	96.40	96.70	96.43	96.81	97.24	96.89	96.96	96.41	95.56
-O equ.	0.17	0.00	0.17	0.05	0.13	0.10	0.07	0.14	0.19	0.13	0.10	0.11	0.10
	---	---	---	---	---	---	---	---	---	---	---	---	---
	96.21	95.53	96.63	95.42	96.27	96.60	96.36	96.67	97.05	96.76	96.86	96.30	95.45
nbr. of													
Si 4+	3.49	3.54	3.49	3.34	3.47	3.47	3.49	3.50	3.54	3.45	3.41	3.55	3.47
Al	0.51	0.46	0.51	0.66	0.53	0.53	0.51	0.50	0.46	0.55	0.59	0.45	0.53
	4.00	4.00	4.00	4.00	4.00	4.00	4.00	4.00	4.00	4.00	4.00	4.00	4.00
Al	1.42	1.46	1.45	1.51	1.47	1.46	1.39	1.44	1.41	1.39	1.43	1.42	1.40
Ti 4+	0.01	0.01	0.01	0.01	0.01	0.01	0.03	0.01	0.01	0.02	0.02	0.01	0.01
Cr 3+	0.00	0.00	0.00	0.00	0.00	0.00	0.00	0.00	0.00	0.00	0.00	0.00	0.00
Mg2+	0.24	0.21	0.22	0.22	0.21	0.21	0.25	0.22	0.21	0.24	0.25	0.21	0.23
Fe 2+	0.37	0.36	0.35	0.35	0.35	0.35	0.39	0.37	0.39	0.41	0.38	0.38	0.42
Mn 2+	0.00	0.00	0.01	0.01	0.01	0.01	0.00	0.01	0.01	0.01	0.01	0.02	0.02
	2.05	2.05	2.04	2.09	2.05	2.05	2.07	2.05	2.03	2.07	2.09	2.04	2.08
Ca 2+	0.00	0.00	0.00	0.00	0.00	0.00	0.00	0.00	0.00	0.00	0.00	0.00	0.00
Ba 2+	0.00	0.00	0.00	0.00	0.00	0.00	0.00	0.00	0.00	0.00	0.00	0.00	0.00
Na +	0.00	0.00	0.01	0.01	0.01	0.00	0.00	0.00	0.00	0.00	0.01	0.00	0.00
K +	0.87	0.86	0.85	0.91	0.86	0.88	0.88	0.86	0.88	0.89	0.89	0.87	0.88
	0.87	0.87	0.86	0.92	0.87	0.89	0.88	0.87	0.88	0.90	0.90	0.88	0.89
Cl	0.00	0.00	0.00	0.00	0.00	0.00	0.00	0.00	0.00	0.00	0.00	0.00	0.00
F	0.09	0.00	0.09	0.03	0.07	0.05	0.04	0.07	0.10	0.07	0.05	0.06	0.05
	---	---	---	---	---	---	---	---	---	---	---	---	---
total	7.01	6.92	6.99	7.04	6.99	6.99	6.99	6.99	7.01	7.04	7.04	6.97	7.02
Mg/Mg+F	0.39	0.37	0.38	0.38	0.38	0.37	0.39	0.37	0.35	0.37	0.40	0.35	0.35
Na/K+Na	0.00	0.01	0.01	0.01	0.01	0.00	0.00	0.00	0.00	0.00	0.01	0.00	0.00

Table 3.3: continued

	Sample 65						Sample 102						
Comment	**phengite**	**phengite**	**phengite**	**phengite**	**phengite**	**phengite**	**phengite**	**phengite**	**phengite**	**phengite**	**phengite**	**phengite**	**phengite**
No.	**14**	**15**	**16**	**17**	**18**	**19**	**1**	**2**	**3**	**4**	**5**	**6**	**7**
SiO2	51.57	52.29	52.38	52.29	52.92	51.77	53.10	52.85	52.49	53.05	53.21	52.21	52.05
Al2O3	25.16	25.29	24.15	24.35	24.20	25.53	23.46	24.31	24.85	24.85	23.83	25.44	25.33
TiO2	0.19	0.17	0.16	0.15	0.15	0.21	0.15	0.24	0.28	0.25	0.24	0.25	0.28
Cr2O3	0.04	0.01	0.00	0.00	0.03	0.01	0.05	0.04	0.07	0.00	0.08	0.04	0.07
MgO	2.45	2.12	1.96	2.18	2.10	2.23	2.66	2.60	2.72	2.67	3.07	2.41	2.60
FeO	5.75	5.97	6.77	6.35	6.90	6.37	6.45	6.12	5.68	5.77	5.73	5.39	5.39
MnO	0.02	0.25	0.18	0.15	0.16	0.14	0.12	0.14	0.16	0.16	0.15	0.13	0.04
CaO	0.00	0.00	0.06	0.00	0.02	0.00	0.00	0.03	0.00	0.00	0.01	0.04	0.00
BaO	0.02	0.10	0.00	0.10	0.00	0.06	0.03	0.12	0.00	0.00	0.07	0.00	0.06
Na2O	0.06	0.02	0.00	0.00	0.02	0.03	0.00	0.00	0.00	0.00	0.00	0.02	0.03
K2O	10.32	10.38	9.48	10.49	10.28	10.27	10.34	10.43	10.57	10.30	10.29	9.86	10.21
Cl	0.01	0.01	0.01	0.00	0.01	0.00	0.07	0.02	0.01	0.02	0.04	0.01	0.01
F	0.03	0.53	0.23	0.37	0.28	0.32	0.63	0.46	0.36	0.56	0.38	0.27	0.51
	95.61	97.14	95.37	96.42	97.07	96.93	97.05	97.36	97.20	97.63	97.14	96.06	96.57
-O equ.	0.01	0.21	0.09	0.15	0.11	0.13	0.27	0.19	0.15	0.23	0.16	0.11	0.20
	---	---	---	---	---	---	---	---	---	---	---	---	---
	95.60	96.92	95.28	96.28	96.95	96.80	96.78	97.17	97.05	97.40	96.98	95.95	96.36
nbr. of													
Si 4+	3.48	3.48	3.54	3.51	3.53	3.45	3.54	3.51	3.49	3.50	3.53	3.48	3.47
Al	0.52	0.52	0.46	0.49	0.47	0.55	0.46	0.49	0.51	0.50	0.47	0.52	0.53
	4.00	4.00	4.00	4.00	4.00	4.00	4.00	4.00	4.00	4.00	4.00	4.00	4.00
Al	1.48	1.46	1.46	1.44	1.43	1.46	1.38	1.41	1.43	0.43	1.40	0.49	1.45
Ti 4+	0.01	0.01	0.01	0.01	0.01	0.01	0.01	0.01	0.01	0.01	0.01	0.01	0.01
Cr 3+	0.00	0.00	0.00	0.00	0.00	0.00	0.00	0.00	0.00	0.00	0.00	0.00	0.00
Mg2+	0.25	0.21	0.20	0.22	0.21	0.22	0.20	0.26	0.27	0.26	0.30	0.24	0.26
Fe 2+	0.32	0.33	0.38	0.36	0.38	0.36	0.36	0.34	0.32	0.32	0.32	0.30	0.30
Mn 2+	0.00	0.01	0.01	0.01	0.01	0.01	0.01	0.01	0.01	0.01	0.01	0.01	0.00
	2.06	2.02	2.06	2.03	2.04	2.06	2.02	2.03	2.04	2.03	2.04	2.05	2.03
Ca 2+	0.00	0.00	0.00	0.00	0.00	0.00	0.00	0.00	0.00	0.00	0.00	0.00	0.00
Ba 2+	0.00	0.00	0.00	0.00	0.00	0.00	0.00	0.00	0.00	0.00	0.00	0.00	0.00
Na +	0.01	0.00	0.00	0.00	0.00	0.00	0.00	0.00	0.00	0.00	0.00	0.00	0.00
K +	0.89	0.88	0.82	0.90	0.87	0.87	0.88	0.88	0.90	0.00	0.87	0.84	0.87
	0.90	0.89	0.82	0.90	0.88	0.88	0.88	0.89	0.90	0.87	0.87	0.84	0.87
Cl	0.00	0.00	0.00	0.00	0.00	0.00	0.10	0.00	0.00	0.87	0.00	0.00	0.00
F	0.01	0.11	0.05	0.08	0.06	0.07	0.13	0.10	0.08	0.00	0.08	0.06	0.11
	---	---	---	---	---	---	---	---	---	0.12	---	---	---
total	6.96	7.02	6.93	7.01	6.98	7.00	7.04	7.02	7.01	7.02	7.00	6.95	7.01
Mg/Mg+F	0.43	0.39	0.34	0.38	0.35	0.38	0.42	0.43	0.46	0.45	0.49	0.44	0.46
Na/K+Na	0.01	0.00	0.00	0.00	0.00	0.00	0.00	0.00	0.00	0.00	0.00	0.00	0.00

Table 3.3: continued

	Sample 102					Sample 80A					
Comment	**pheng.**	**pheng.**	**pheng.**	**pheng.**	**pheng.**	**pheng.**	**pheng.**	**pheng.**	**pheng.**	**pheng.**	**pheng.**
No.	**8**	**9**	**10**	**11**	**12**	**19**	**22**	**23**	**26**	**27**	**28**
SiO2	53.13	53.17	51.75	52.18	52.90	52.20	52.15	52.93	52.77	52.93	50.45
Al2O3	25.00	24.08	23.73	25.44	24.56	25.53	24.95	24.54	24.40	23.23	27.23
TiO2	0.18	0.24	0.45	0.30	0.26	0.26	0.19	0.16	0.29	0.18	0.32
Cr2O3	0.04	0.03	0.04	0.02	0.05	0.05	0.06	0.01	0.05	0.01	0.04
MgO	2.71	2.75	3.02	2.48	2.68	2.17	2.34	2.09	2.23	2.28	2.44
FeO	5.85	5.92	6.83	5.58	5.86	5.79	5.83	6.40	6.11	7.02	5.35
MnO	0.09	0.13	0.01	0.14	0.01	0.23	0.17	0.13	0.22	0.17	0.12
CaO	0.00	0.00	0.00	0.02	0.01	0.02	0.02	0.02	0.03	0.05	0.00
BaO	0.22	0.04	0.00	0.14	0.00	0.00	0.00	0.03	0.06	0.04	0.00
Na2O	0.00	0.01	0.02	0.01	0.01	0.10	0.00	0.03	0.04	0.02	0.09
K2O	10.40	10.57	10.43	10.10	10.17	9.88	10.21	10.21	10.04	9.66	10.16
Cl	0.02	0.02	0.01	0.00	0.02	0.01	0.00	0.00	0.00	0.00	0.00
F	0.40	0.02	0.32	0.31	0.36	0.10	0.27	0.08	0.00	0.07	0.34
	98.05	96.97	96.61	96.71	96.89	96.34	96.19	96.62	96.24	96.37	96.54
-O equ.	0.17	0.01	0.13	0.12	0.15	0.04	0.11	0.03	0.00	0.03	0.14
	---	---	---	---	---	---	---	---	---	---	---
	97.88	96.96	96.48	96.58	96.74	96.30	96.08	96.58	96.24	96.34	96.34
nbr. of ions											
Si 4+	3.50	3.54	3.48	3.47	3.51	3.48	3.49	3.53	3.53	3.55	3.37
Al	0.50	0.46	0.52	0.53	0.49	0.52	0.51	0.47	0.47	0.45	0.63
	4.00	4.00	4.00	4.00	4.00	4.00	4.00	4.00	4.00	4.00	4.00
Al	1.44	1.43	1.36	1.47	1.43	1.49	1.46	1.46	1.46	1.43	1.51
Ti 4+	0.10	0.01	0.02	0.02	0.01	0.01	0.01	0.01	0.01	0.01	0.02
Cr 3+	0.00	0.00	0.00	0.00	0.00	0.00	0.00	0.00	0.00	0.00	0.00
Mg2+	0.27	0.27	0.30	0.25	0.27	0.22	0.23	0.21	0.22	0.23	0.24
Fe 2+	0.32	0.33	0.38	0.31	0.33	0.32	0.33	0.36	0.34	0.39	0.30
Mn 2+	0.01	0.01	0.00	0.01	0.00	0.01	0.01	0.01	0.01	0.01	0.01
	2.04	2.05	2.07	2.05	2.04	2.06	2.04	2.05	2.05	2.08	2.07
Ca 2+	0.00	0.00	0.00	0.00	0.00	0.00	0.00	0.00	0.00	0.00	0.00
Ba 2+	0.01	0.00	0.00	0.00	0.00	0.00	0.00	0.00	0.00	0.00	0.00
Na +	0.00	0.00	0.00	0.00	0.00	0.01	0.00	0.00	0.00	0.00	0.01
K +	0.87	0.90	0.89	0.86	0.86	0.84	0.87	0.87	0.87	0.83	0.86
	0.88	0.90	0.90	0.86	0.86	0.85	0.87	0.87	0.87	0.83	0.88
Cl	0.00	0.00	0.00	0.00	0.00	0.00	0.00	0.00	0.00	0.00	0.00
F	0.08	0.00	0.07	0.06	0.07	0.02	0.06	0.20	0.00	0.01	0.07
	---	---	---	---	---	---	---	---	---	---	---
total	7.00	6.96	7.04	6.98	6.98	6.94	6.98	6.94	6.92	6.92	7.02
Mg/Mg+Fe	0.45	0.45	0.44	0.44	0.45	0.40	0.42	0.37	0.39	0.37	0.45
Na/K+Na	0.00	0.00	0.00	0.00	0.00	0.00	0.00	0.00	0.00	0.00	0.01

Table 3.4: Representative microprobe analyses of plagioclase from the analyzed samples from Gran Paradiso unit.

	Sample 65		Sample 102				Sample 80A					
Comment	**plag.**	**plag.**	**plag.**	**plag.**	**plag.**	**plag.**	**plag.**	**plag.**	**plag.**	**plag.**	**plag.**	**plag.**
No.	**20**	**21**	**13**	**14**	**15**	**16**	**17**	**18**	**20**	**21**	**24**	**25**
SiO2	65.50	64.91	68.68	67.79	66.45	66.59	68.20	67.59	68.70	67.68	69.05	68.73
Al2O3	18.96	19.08	20.67	20.90	20.82	21.02	20.25	20.39	19.97	21.03	21.21	20.96
TiO2	0.00	0.00	0.00	0.02	0.00	0.06	0.01	0.00	0.01	0.01	0.00	0.00
Cr2O3	0.06	0.06	0.00	0.07	0.00	0.02	0.05	0.06	0.00	0.01	0.03	0.05
MgO	0.00	0.01	0.00	0.00	0.00	0.00	0.00	0.00	0.00	0.00	0.01	0.00
FeO	0.00	0.00	0.03	0.00	0.04	0.02	0.03	0.09	0.00	0.00	0.00	0.00
MnO	0.00	0.01	0.02	0.00	0.02	0.00	0.00	0.02	0.00	0.02	0.01	0.03
CaO	0.00	0.00	0.01	0.22	0.38	0.21	0.03	0.02	0.04	0.20	0.05	0.13
BaO	0.34	0.35	0.00	0.00	0.05	0.01	0.03	0.09	0.00	0.00	0.02	0.02
Na2O	0.85	0.62	10.73	11.21	10.78	10.81	11.47	11.73	11.82	11.01	11.45	11.27
K2O	15.08	15.52	0.11	0.14	0.14	0.12	0.15	0.15	0.08	0.09	0.16	0.16
	---	---	---	---	---	---	---	---	---	---	---	---
total	100.78	100.57	100.25	100.34	98.69	98.86	100.22	100.15	100.63	100.05	101.99	101.35
Normalization to												
Si4+	2.99	2.98	2.98	2.95	2.94	2.94	2.97	2.96	2.98	2.95	2.96	2.96
Al	1.02	1.03	1.06	1.07	1.09	1.09	1.04	1.05	1.02	1.08	1.07	1.06
Fe3+	0.00	0.00	0.00	0.00	0.00	0.00	0.00	0.00	0.00	0.00	0.00	0.00
Ti	0.00	0.00	0.00	0.00	0.00	0.00	0.00	0.00	0.00	0.00	0.00	0.00
Cr	0.00	0.00	0.00	0.00	0.00	0.00	0.00	0.00	0.00	0.00	0.00	0.00
Mg	0.00	0.00	0.00	0.00	0.00	0.00	0.00	0.00	0.00	0.00	0.00	0.00
Mn	0.00	0.00	0.00	0.00	0.00	0.00	0.00	0.00	0.00	0.00	0.00	0.00
Ca	0.00	0.00	0.00	0.01	0.02	0.01	0.00	0.00	0.00	0.01	0.00	0.01
Ba	0.01	0.01	0.00	0.00	0.00	0.00	0.00	0.00	0.00	0.00	0.00	0.00
Na	0.07	0.06	0.90	0.95	0.93	0.93	0.97	1.00	1.00	0.93	0.95	0.94
K	0.88	0.91	0.01	0.01	0.01	0.01	0.01	0.01	0.00	0.00	0.01	0.01
	---	---	---	---	---	---	---	---	---	---	---	---
total	4.97	4.99	4.95	4.99	4.98	4.98	5.00	5.02	5.01	4.98	4.99	4.98
Plagioclase												
An	0.00	0.00	0.05	1.05	1.91	1.08	0.13	0.10	0.19	0.99	0.23	0.64
Ab	100.00	100.00	99.95	98.95	98.09	98.92	99.87	99.90	99.81	99.01	99.77	99.36
Alkali feldspar												
Ab	7.85	5.74	99.36	99.17	99.13	99.25	99.15	99.15	99.53	99.48	99.08	99.07
Or	92.15	94.26	0.64	0.83	0.87	0.75	0.85	0.85	0.47	0.52	0.92	0.93
Ternary feldspar												
An	0.00	0.00	0.05	1.04	1.90	1.07	0.13	0.10	0.19	0.98	0.22	0.64
Ab	7.85	5.74	99.31	98.14	97.25	98.19	99.02	99.05	99.35	98.50	98.86	98.44
Or	92.15	94.26	0.64	0.82	0.85	0.74	0.85	0.85	0.46	0.52	0.91	0.92

Table 3.5: Average major (in wt%) and trace element (in ppm) of Gran Paradiso samples.

	GP01-01	GP01-05	GP99-6	GP01-9A	GP01-03	GP01-17	GP01-07B	GP01-15B	GP01-24	GP01-23A
SiO2	74.59	72.05	73.05	73.88	73.67	71.16	71.92	74.50	73.36	74.97
Al2O3	13.29	13.45	13.84	13.16	13.09	13.72	13.61	12.69	12.72	12.38
FeO*	1.87	2.69	1.80	2.06	2.11	3.08	2.90	2.04	2.59	1.89
MnO	0.06	0.03	0.04	0.05	0.04	0.06	0.04	0.04	0.04	0.03
MgO	0.34	0.84	0.38	0.33	0.57	0.63	0.67	0.34	0.49	0.32
CaO	0.63	0.52	0.40	0.84	0.77	1.98	0.50	0.91	1.43	0.79
Na2O	3.36	3.34	3.45	3.20	3.28	3.16	3.17	2.80	2.96	2.86
K2O	4.78	4.41	5.02	4.57	4.45	3.92	4.69	4.79	3.77	4.55
TiO2	0.19	0.34	0.20	0.23	0.27	0.40	0.35	0.22	0.34	0.22
P2O5	0.10	0.10	0.12	0.14	0.13	0.15	0.16	0.12	0.12	0.11
LO1	0.70	1.34	1.18	0.87	0.78	0.71	1.33	0.84	0.58	0.68
Total	99.91	99.18	99.47	99.33	99.16	98.97	99.35	99.28	98.40	98.81
Sc	3.00	6.00	4.00	4.00	4.00	6.00	7.00	4.00	5.00	3.00
V	12.00	22.00	13.00	14.00	18.00	31.00	24.00	16.00	21.00	14.00
Cr	7.00	12.00	7.00	12.00	10.00	11.00	12.00	11.00	18.00	12.00
Co	84.00	75.00	97.00	83.00	66.00	113.00	88.00	111.00	108.00	129.00
Ni	2.00	6.00	4.00	4.00	4.00	5.00	6.00	3.00	7.00	5.00
Cu	7.00	3.00	4.00	5.00	3.00	3.00	7.00	4.00	7.00	3.00
Zn	41.00	28.00	30.00	42.00	41.00	48.00	40.00	36.00	40.00	39.00
Ga	17.00	17.00	16.00	17.00	16.00	18.00	19.00	14.00	16.00	14.00
Rb	280.00	179.00	246.00	234.00	234.00	118.00	214.00	169.00	143.00	140.00
Sr	41.00	60.00	33.00	53.00	72.00	242.00	96.00	64.00	90.00	75.00
Y	30.00	36.00	23.00	28.00	32.00	34.00	35.00	31.00	38.00	30.00
Zr	92.00	188.00	111.00	130.00	122.00	197.00	183.00	116.00	178.00	126.00
Nb	10.00	14.00	10.00	12.00	11.00	11.00	14.00	8.00	10.00	8.00
Ba	187.00	454.00	291.00	292.00	353.00	830.00	421.00	421.00	509.00	471.00

Curriculum Vitae

Name	: Osama Mohamed Kaoud Kassem
Family name	: Kassem
Nationality	: Egyptian
Date and Place of Birth	: 10\12\1969, Tahta, Sohag, Egypt.
Marital status	: Married, three children
Languages	: Arabic (mother tongue), English (good), German (fair)
Profession	: Assistant Researcher
Address in Egypt	: Geophysics Lab., Geology & Geophysics Department, National Research Center, EL-Tahrir St., Dokki, Cairo, Egypt.
Address in Germany	: Institut für Geowissenschaften, Abteilung Geologie, Becherweg 21, Universität Mainz, 55099 Mainz

……

* Educational Career:-

1. 1976-1981: EL Komea Prep- School, Tahta, Souhag, Egypt
2. 1981-1984: EL Islamia Primary School, Tahta, Souhag
3. 1984-1987: Rephaa EL Tahtawy Secondary School, Tahta, Souhag
4. 1987-1991: Department of Geology, Faculty of Science, University of Assuit (Souhag branch), Souhag
5. 1991: B.Sc. in Geology with grade "Very Good", Assiut University (Souhag branch), Souhag
6. 1995: Pre Master studies (Diploma), Assiut University, Egypt.
7. 1998: M.Sc. in Geophysics, Assiut University.
8. 1998-2001: Assistant Researcher, Geophysics Lab, Geology & Geophysics Sciences Department, National Research Center.
9. 2001-2005: Doktorand, Institute of Geosciences, Faculty of Natural Sciences, University of Mainz, Mainz, Germany

بِسْمِ ٱللَّـهِ ٱلرَّحْـمَٰنِ ٱلرَّحِـيمِ ﴿١﴾ ٱلْحَـمْدُ لِلَّـهِ رَبِّ ٱلْعَٰلَمِيـنَ ﴿٢﴾
ٱلرَّحْـمَٰنِ ٱلرَّحِـيمِ ﴿٣﴾ مَٰلِـكِ يَـوْمِ ٱلـدِّينِ ﴿٤﴾ إِيَّـاكَ نَعْبُدُ وَإِيَّـاكَ
نَسْـتَعِينُ ﴿٥﴾ ٱهْدِنَـا ٱلصِّرَٰطَ ٱلْمُسْـتَقِيمَ ﴿٦﴾ صِرَٰطَ ٱلَّذِينَ أَنْعَمْتَ
عَلَيْهِمْ غَيْرِ ٱلْمَغْضُوبِ عَلَيْهِمْ وَلَا ٱلضَّآلِّينَ ﴿٧﴾


وجعل لكم من الجبال أكناناً